

X-ray crystallographic characterization of heavy metal-nucleosome association and nucleosome core particle composed of novel DNA sequences

Mohideen Abdul Kareem

2010

Mohideen, A. K. (2010). X-ray crystallographic characterization of heavy metal-nucleosome association and nucleosome core particle composed of novel DNA sequences. Doctoral thesis, Nanyang Technological University, Singapore.

<https://hdl.handle.net/10356/47441>

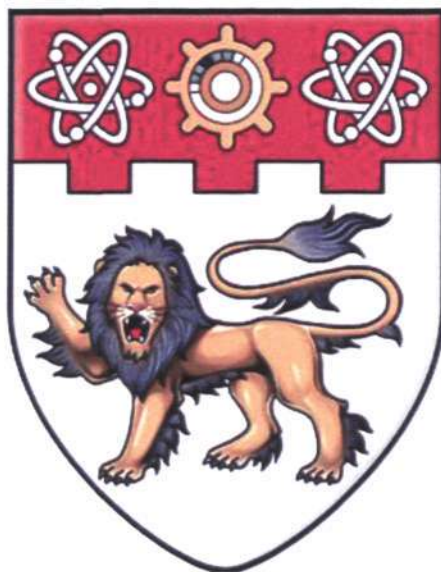
<https://doi.org/10.32657/10356/47441>

Nanyang Technological University

Downloaded on 20 Mar 2024 17:32:28 SGT

**X-Ray Crystallographic Characterization of Heavy Metal-
Nucleosome Association and Nucleosome Core Particle
Composed of Novel DNA Sequences**

Mohideen Abdul Kareem



Ph.D. Thesis

**School of Biological Sciences
Nanyang Technological University
Singapore**

2010

Acknowledgements

This research work is the most important scientific accomplishment in my life, and I would like to thank those who have supported me during this period.

I would like to express my sincere gratitude to my Ph.D. supervisor Dr. Curt Alexander Davey. He provided me with many helpful suggestions, important advice and constant encouragement during the course of this work.

I am especially grateful to my labmates Dileep, Wu Bin, Michelle, Reyhan, Gabriela, Zenita and Hong Tian, as well as my friends Asha, Venthan, Malathy, Jana, Rajakannan, Smeeta, Saravanan, Rathi, Insaf, Mano, Anil and Bagu.

I would like to thank the beam line staff at the Swiss Light Source, Switzerland for their help during my data collection.

I would like to thank NTU for the research scholarship which supported my research and stay in Singapore.

Finally, I wish to dedicate this thesis to my mother, my family and all my teachers.

TABLE OF CONTENTS

ACKNOWLEDGEMENTS	i
TABLE OF CONTENTS	ii
LIST OF ABBREVIATIONS	x
PUBLICATIONS	xi
ABSTRACT	1
1. NUCLEOSOMES AND NUCLEOSOME CORE PARTICLES	5
1.1. Structure of histone octamer	6
1.2. Histone post-translational modifications	9
1.3. Histone variants	10
1.4. Structure of nucleosome core particle	10
1.4.1. <i>Structural aspects of DNA in NCP</i>	13
1.4.2. <i>Interactions of DNA and histone octamer within NCP</i>	15
1.5. Significance of nucleosome organization	16
2. HEAVY METALS AND CANCER	19
2.1. Role of oxygen in metal-mediated DNA damage	20
2.2. Metal-mediated mechanisms in carcinogenesis	21
2.3. Metal-induced carcinogenesis and epigenetics	22
2.4. OBJECTIVES	24
3. MATERIALS AND METHODS	27
3.1. 147 bp DNA Preparation	29
3.1.1. <i>Transformation</i>	30
3.1.2. <i>Plasmid amplification</i>	31
3.1.3. <i>Plasmid extraction</i>	31
3.1.4. <i>EcoRV digestion</i>	33

3.1.5.	<i>PEG fractionation</i>	34
3.1.6.	<i>Dephosphorylation</i>	35
3.1.7.	<i>HinI digestion</i>	36
3.1.8.	<i>Purification of 72+3 bp DNA</i>	37
3.1.9.	<i>Ligation</i>	39
3.1.10.	<i>Purification of 147 bp DNA</i>	40
3.2.	Preparation of histones	42
3.2.1.	<i>Transformation</i>	43
3.2.2.	<i>Protein expression</i>	43
3.2.3.	<i>Inclusion body preparation</i>	43
3.2.4.	<i>Purification of crude histones</i>	44
3.2.5.	<i>Histone octamer refolding</i>	46
3.2.6.	<i>Purification of histone octamer</i>	46
3.3.	NCP Reconstitution	48
3.4.	Preparation of designer DNA	51
3.4.1.	<i>Transformation, amplification, isolation and purification of designer DNA</i>	52
3.4.2.	<i>EcoRV digestion</i>	53
3.4.3.	<i>PEG fractionation</i>	53
3.4.4.	<i>Dephosphorylation</i>	54
3.5.	Crystallization of NCP	55
3.6.	Data collection and processing	56
3.7.	Atomic absorption spectroscopy	57
3.8.	Buffer compositions	59
4.	CRYSTALLOGRAPHIC RESULTS	62
4.1.	Crystallization of NCP using several divalent metals	62
4.1.1.	Magnesium form of NCP	62

4.1.2. Calcium form of NCP	63
4.1.3. Mercury soaked crystal data in Mg^{2+} background	64
4.1.4. Cadmium soaked crystals	65
4.2. Crystallographic characterization of Ni^{2+} binding to NCP	65
4.2.1. <i>General features of Ni^{2+} in NCP structure</i>	68
4.2.2. <i>Register shift of DNA in NCP upon nickel ions binding</i>	69
4.2.3. <i>Stretching of DNA from -2 to -1.5 SHL</i>	70
4.2.4. <i>Position of nickel ions</i>	71
4.2.5. <i>Electron density of the DNA bases</i>	73
4.2.6. <i>Missing base pair in the compaction region</i>	73
4.2.7. <i>Different NCP models and omit maps to locate the missing base pair in the compaction region</i>	74
4.2.8. <i>Occupancy and B-values for nickel atoms in the Ni^{2+}-NCP structure</i>	76
4.2.9. <i>Sites of Ni^{2+} binding</i>	76
4.2.10. <i>Modes of Ni^{2+} binding in the major groove</i>	80
4.2.11. <i>New metal binding sites in the Ni^{2+}-NCP structure</i>	81
4.2.12. <i>Ni^{2+} mediated crystal contact site in NCP-DNA</i>	85
4.2.13. <i>Tetra-nucleotide binding features of Ni^{2+}</i>	86
4.2.14. <i>Di-nucleotide binding features of nickel ions</i>	87
4.2.15. <i>Four-bond mode Ni^{2+} binding in Ni^{2+}-NCP DNA</i>	87
4.2.16. <i>Three-bond mode Ni^{2+} binding with Ni^{2+}-NCP DNA</i>	88
4.2.17. <i>Ni^{2+} binding in the minor groove of NCP</i>	89
4.2.18. <i>Ni^{2+} binding to histone proteins</i>	91
4.2.19. <i>Geometric parameters of DNA in Ni^{2+}-NCP structure</i>	92
4.3. Crystallographic characterization of Co^{2+} binding to NCP	93
4.3.1. <i>Similarities between Co^{2+} and Ni^{2+} binding to NCP</i>	97

4.3.2.	<i>Differences between Co^{2+} and Ni^{2+} binding to NCP</i>	97
4.3.3.	<i>Geometric parameters of DNA in Co^{2+}-NCP structure</i>	99
4.4.	Crystallographic characterization of monovalent heavy metals binding to NCP	101
4.4.1.	<i>Monovalent metals in the minor groove DNA of NCP</i>	104
5.	NEW DNA SEQUENCES (147*) AND THEIR SEQUENCE	
	CONFORMATION-RELATIONSHIPS IN NCP	106
5.1.	Designer 2 NCP crystallization	107
5.2.	Designer 2 NCP crystal harvesting and data collection	110
5.3.	Structure of des 2 NCP	111
5.3.1.	<i>Orientation of DNA in des 2 NCP</i>	112
5.3.2.	<i>DNA end stacking in des 2 NCP</i>	112
5.3.3.	<i>Minor groove narrowing at TA region of des 2 NCP</i>	113
5.3.4.	<i>High thermal factors for des 2 NCP</i>	114
5.3.5.	<i>Cation binding to the DNA of des 2 NCP</i>	115
6.	DISCUSSION	120
6.1.	Importance of manganese in NCP crystallization	120
6.2.	Heavy metal ions and DNA binding	121
6.3.	Biological significance of Ni^{2+} in carcinogenesis	122
6.4.	Metallodrugs in cancer	124
6.5.	Monovalent ions in the DNA of NCP	125
6.6.	Designer DNA and its NCP	125
6.7.	Outlook	128
7.	REFERENCES	132-141

List of Diagrams

Diagram 1.	Flow chart showing the preparation of NCP	28
Diagram 2.	Flow chart showing the preparation of 147 bp DNA	30

List of Figures

Figure 1. Image showing the 1.9 Å structure of histone octamer	7
Figure 2. Image showing BS, MC and H42B interaction regions	8
Figure 3. Crystal structure of the NCP	11
Figure 4. 1.9 Å structure of NCP147 showing its solvation state	12
Figure 5. One half of NCP147	14
Figure 6. Agarose gel of extracted plasmid	33
Figure 7. DNA PAGE of <i>EcoRV</i> digestion	34
Figure 8. DNA PAGE of PEG fractionation	35
Figure 9. DNA PAGE of dephosphorylation test	36
Figure 10. DNA PAGE of <i>HinfI</i> digestion	37
Figure 11. FPLC profile of 72+3 bp DNA purification	38
Figure 12. DNA PAGE of FPLC purified 72+3 bp DNA	39
Figure 13. DNA PAGE of T4 ligation reaction	40
Figure 14. FPLC profile of 147 bp purification	41
Figure 15. DNA PAGE of 147 bp purification	41
Figure 16. SDS PAGE of crude histone (H3) after expression	44
Figure 17. FPLC profile of H2A purification	45
Figure 18. SDS PAGE of H2A purification	45
Figure 19. SDS PAGE of pure histones	46
Figure 20. FPLC profile of histone octamer purification	47
Figure 21. SDS PAGE of purified histone octamer	47
Figure 22. EMSA of reconstituted NCP	49
Figure 23. FPLC profile of NCP purification	50
Figure 24. EMSA of ion-exchange purified NCP	50
Figure 25. Comparison of 147α8s and the designer sequences	51

Figure 26. Plasmid vector pUC57 and details of the multiple cloning sites (MCS)	52
Figure 27. DNA PAGE of <i>EcoRV</i> digestion	53
Figure 28. DNA PAGE of PEG fractionation and dephosphorylation	54
Figure 29. Crystal of NCP grown under standard MnCl_2 condition	55
Figure 30. Generation of a standard concentration profile for Mn^{2+} by atomic absorption spectroscopy	58
Figure 31. Crystal of NCP grown in Mg^{2+} containing buffer	63
Figure 32. Crystal of NCP grown in Ca^{2+} containing buffer	63
Figure 33. Anomalous map contoured at 9σ shows the signal of Hg^{2+} binding to cysteine residues C110 of H3	64
Figure 34. Crystal structure of NCP in the presence of 37mM Ni^{2+}	67
Figure 35. Comparison of DNA sequences from the crystal structures of NCP147 and NCP145	71
Figure 36. Position of nickel ions near the NCP dyad from the initial molecular replacement model	71
Figure 37. Orientation of the DNA with respect to metal ions	72
Figure 38. Electron density map for the initial NCP147 model	73
Figure 39. A view of the electron density map in the compaction region calculated using the NCP145 model	74
Figure 40. Omit map in the compaction region	75
Figure 41. Binding mode of manganese ions to the DNA major groove of NCP	80
Figure 42. Structural comparison of 5'-AGAT-3' (multi-color) with 5'-AGGT-3' (gray) using least squares superposition (LSS)	82
Figure 43. Structural comparison of 5'-AGTA-3' (multi-color) with 5'-AGCA-3' (gray) using LSS	83
Figure 44. Ni^{2+} binding to adenine base	84

Figure 45. Inter-particle DNA contact site	85
Figure 46. Structural comparison between the two tetra-nucleotide (5'-AGGC-3' and 5'-AGGT-3') and (5'-TGGT-3' and 5'-AGGT-3')	86
Figure 47. Tetra-nucleotide, with two different Ni^{2+} binding directly to the GG nucleotide	88
Figure 48. Four-bond mode interactions	89
Figure 49. Metal binding in the minor groove of NCP	90
Figure 50. Binding of Ni^{2+} to histidine residues at the inter-particles site	91
Figure 51. DNA geometrical parameters for Ni^{2+} -NCP	92
Figure 52. Four-bond mode site in Co^{2+} -NCP DNA	98
Figure 53. DNA geometrical parameters for Co^{2+} -NCP	99
Figure 54. Manganese absorption edge	103
Figure 55. Cs^+ in the minor groove of NCP	105
Figure 56. EMSA of reconstituted designer NCP	106
Figure 57. Crystals of NCP grown in MnCl_2 condition	107
Figure 58. Diffraction pattern of des 2 NCP grown in MnCl_2 condition	108
Figure 59. Crystal of des 2 NCP grown in MnCl_2 , MPD and HgCl_2	109
Figure 60. Final des 2 NCP crystals	109
Figure 61. Diffraction pattern of des 2 NCP crystal	110
Figure 62. NCP DNA termini	113
Figure 63. Minor groove width data	114
Figure 64. DNA inter-particle site	115
Figure 65. DNA stretching in -1.5 SHL of Ni^{2+} -NCP structure	123

List of Tables

Table 1. Atomic absorption spectroscopic readings of manganese in nickel and cobalt-containing buffers and NCP crystals	58
Table 2. Crystallographic statistics for Ni ²⁺ - NCP	68
Table 3. Occupancy and <i>B</i> -factors for Ni ²⁺ calculated using the MLPhare program	78
Table 4. Ni ²⁺ sites in the DNA of NCP	79
Table 5. Protein binding sites of Ni ²⁺ in the NCP	91
Table 6. Crystallographic statistics for Co ²⁺ - NCP	94
Table 7. Occupancy and <i>B</i> -factors for Co ²⁺ calculated using the MLPhare program	95
Table 8. Co ²⁺ sites in the DNA of NCP	96
Table 9. Protein binding sites of Co ²⁺ in the NCP	97
Table 10. Crystallographic statistics for Rb ⁺ -NCP	102
Table 11. Crystallographic statistics for Cs ⁺ -NCP	103
Table 12. Monovalent ion sites in the DNA minor groove of NCP	104
Table 13. Crystallographic statistics for des 2 NCP	111
Table 14. Metal binding sites in des 2 NCP	116

List of Abbreviations

Abbreviated Form	Long Form
NCP	Nucleosome Core Particle
HO	Histone Octamer
BME	Beta-Mercapto Ethanol
CIAP	Calf Intestine Alkaline Phosphatase
DMSO	Dimethyl Sulfoxide
DTT	Dithiothreitol
FPLC	Fast Performance Liquid Chromatography
IPTG	Isopropyl β -D-1-thiogalactopyranoside
MW	Molecular Weight
OD	Optical Density
PEG	Polyethylene glycol
SDS-PAGE	Sodium Dodecyl Sulfate-Polyacrylamide Gel Electrophoresis
AAS	Atomic Adsorption Spectroscopy
CIA	Chloroform-isoamyl alcohol
EMSA	Electrophoretic mobility shift assay
MPD	2-methyl-2,4-pentanediol
NCP145	Nucleosome core particle composed of 145 bp DNA
NCP147	Nucleosome core particle composed of 147 bp DNA
TAE	Tris-Acetate-EDTA
TBE	Tris-borate-EDTA
SHL	Super Helical Location

PUBLICATIONS

1. **Kareem Mohideen**, Reyhan Mohammed and Curt A Davey. *Perturbations in Nucleosome Structure from Heavy Metal Association*. (**Nucleic Acid Research** 2010 May 21. [Epub ahead of print])

2. Bin Wu*, **Kareem Mohideen***, Dileep Vasudevan and Curt A Davey. *Structural Insight into the Sequence-Dependence of Nucleosome Positioning*. **Structure** 2010 March 14. 18(4), 528–536.

* These authors have contributed equally

ABSTRACT

Metal ions with strong carcinogenic potential, including Cd^{2+} , Ni^{2+} , Co^{2+} and Cr^{6+} , are known to play a significant role in disrupting a broad range of cellular processes. However, the precise mechanisms by which heavy metals exert their carcinogenic effects are not clear and require further studies. Recent developments suggest that epigenetic mechanisms may play an important role in activating or silencing the expression of genes, which are critical for driving the metal-induced pathogenesis. In our study, using X-ray crystallography, we characterized the binding of Ni^{2+} and Co^{2+} to the nucleosome core particle (NCP) – the fundamental entity of chromatin – in order to comprehend their site-selectivity and influence on the structure of nucleosomal DNA.

We observed remarkable changes upon the binding of Ni^{2+} and Co^{2+} to NCP. Compared to Mn^{2+} , which is harder on the hard and soft acids and bases (*HSAB*) scale, Ni^{2+} and Co^{2+} have higher binding affinity for DNA. In spite of having coordination geometry nearly identical to that of Mn^{2+} , the softer metals have pronounced ability to alter the histone-DNA register in the nucleosome. These softer metals involve not only coordinate to guanine but also to adenine bases, resulting in additional metal-binding sites (GA and AG base steps), as compared to the highest affinity GG and GC steps. Furthermore, the soft Ni^{2+} and Co^{2+} ions have high affinity for association with histone proteins groups, in particular histidine. Association of soft Ni^{2+} and Co^{2+} ions with histones results in additional inter-particle contact sites, which might be relevant to epigenetic mechanisms for gene activation and silencing *in vivo*. The binding of Ni^{2+} and Co^{2+} is also dependent on DNA sequence and conformation, and this site selectivity, together with the high affinity of association, may result in metal toxicity and explain the occurrence of mutational hotspots. In addition, structural and chemical insight gained from our heavy metal binding studies may also contribute to the understanding of principles governing molecular recognition in the nucleosome.

As an extension to the divalent cation studies, we characterized the binding of heavy monovalent cations (Rb^+ and Cs^+) to the NCP. The sequence and conformation of the DNA determine the binding preference of these ions to nucleosomes. Binding to the DNA was only observed at several minor groove elements, with a preference for direct

coordination to narrow AT dinucleotide sites. The binding of monovalent cations to the minor groove could play an important role in A|T-tract structure and groove narrowing, thereby modulating DNA function *in vivo*.

NCP composed of modified DNA molecules can provide new data on sequence dependent DNA structure as well as details regarding distinctions in DNA conformation or histone interactions at different sites on the octamer. Such studies are important for understanding the basis of sequence dependence in nucleosome positioning. Several NCP constructs were assembled with non-palindromic DNA sequences containing strong positioning elements and subjected to crystallization trials. One construct yielded crystals that diffracted to a resolution of 3.05 Å. In spite of the favorable diffraction properties of the crystals, the atomic B-factor average is very high (142 Å²) and the electron density is overall not well defined. Poor electron density map does not permit discrimination between the two possible orientations of the asymmetric core particle in the crystal, which apparently prevail at roughly equal proportion.

INTRODUCTION

1. NUCLEOSOMES AND NUCLEOSOME CORE PARTICLES

The genetic material in eukaryotic nucleus is present in a highly condensed form called chromatin. The state of compaction of DNA is essential for and central to all biological processes. The first level of organization occurs by wrapping the naked DNA on to the histone octamer (HO), and this entity is referred to as a nucleosome. It constitutes the fundamental component of chromatin (Ramakrishnan 1997; Davey *et al.* 2002). The nucleosomes are folded through a series of consecutive higher order structures (HOS), ultimately to form a chromosome. Nucleosomes condense the DNA and create an added level of regulatory control, which underlies accurate gene expression. Nucleosomes are thought to carry epigenetically inherited information in the form of covalent modifications of histones.

As a result of rigid packaging of eukaryotic DNA into nucleosomes and chromatin fibers, the accessibility of DNA is strictly controlled (Kornberg 1981; Davey and Richmond 2002). Thus, a deeper understanding of how the DNA is arranged in the nucleosomes and in HOS can reveal the molecular mechanisms of biological processes such as transcription, replication, recombination, DNA repair, and cell division, as well as pathological processes like cancer and viral infections (Luger *et al.* 1997a; Richmond and Davey 2003). In fact, these fundamental biological events can be fully understood only in the context of nucleosomal DNA structure, which is remarkably different from that of naked DNA. These differences are attributable to the interactions of the basic histone proteins with the DNA. Nucleosomes play both active and passive roles, in both positive and negative gene regulation. They provide a platform for replication, transcription and repair machinery. Specialized nucleosomes facilitate the function of chromosomes in centromeres and telomeres (Widom 1998; Wolffe 1998; Elgin *et al.* 2000; Becker 2002).

Nucleosomes can be visualized as a tandem array of beads under an electron microscope. They are dynamic structures, which can undergo folding and unfolding transitions both *in vitro* and *in vivo* (Thoma *et al.* 1979). The nucleosome consists of the DNA double helix wrapped around HO, with alternating major and minor grooves, which may vary in size according to the helix conformation. If the major groove is wider, then

Introduction

the minor groove on the opposing side of the helix will be narrower and *vice versa*. In addition, the nucleosome contains five different basic histones – H1, H2A, H2B, H3 and H4 (Thoma 1992). The nucleosome core particle (NCP) is the part of the nucleosome without linker DNA and histone (H1). It comprises ~147bp DNA, wrapped in ~1½ turns around a HO, which is assembled from two copies of each H2A, H2B, H3 and H4 histone proteins (Widom 2001).

1.1. Structure of histone octamer

The atomic resolution structure of the HO without DNA has been solved to a resolution of 1.9 Å (Wood *et al.* 2005). This structure gave a very clear picture of the respective histone proteins and their interactions with each other. The high resolution structure of both NCP as well as HO (Fig. 1) showed a basic tripartite assembly for the HO, divulging its organization in functional subunits containing two (H2A-H2B) heterodimers and one tetramer, which are made up of two copies of (H3-H4) (Davey *et al.* 2002; Wood *et al.* 2005).

In the HO, all the eight histone proteins are arranged in the following order – a core region containing a tetramer (H4-H3)-(H3'-H4') with its both sides having one (H2A-H2B) dimer each, to give an overall structure: (H2A-H2B)-(H4-H3)-(H3'-H4')-(H2B'-H2A'). The structure of core histones is well studied (Arents *et al.* 1991; Ramakrishnan 1997). Histone proteins are composed of two main parts; the globular domain, often referred to as the histone fold domain, consisting of three α -helices (α 1, α 2 and α 3), as well as loops L1 and L2 connecting the helices and the tail regions. These intra-histone protein structural entities associating with each other is referred to as a histone fold dimer (Luger 2006). In (H2A-H2B) and (H3-H4) dimers, the two histone folds come together to make a histone-fold pair that creates a rigidly bound stable entity of hydrophobic interactions and hydrogen bonds (Lavelle and Benecke 2006).

Introduction

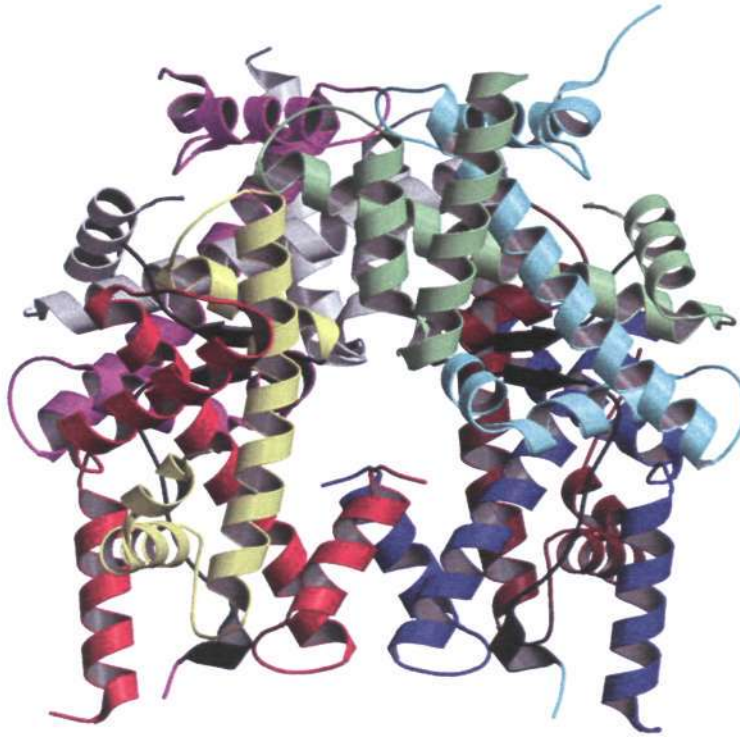


Figure 1. Image showing the 1.9 Å structure of histone octamer (PDB id: 1tzy). H2A, cyan; H2B, light green; H3, red; H4, yellow; H2A', magenta; H2B', grey; H3', blue; H4', brown. The H2A–H4' and H2A'–H4 docking regions are shown in black (The figure is adapted from Wood *et al.* 2005).

Approximately thirty percent of the histone mass is contributed by histone tail extensions, which are highly flexible. The N-terminal tails of H3 and H2B histones pass through a channel formed by the minor grooves of the two DNA strands, protruding from the DNA every 20 bp. On the other hand, the N-terminal tail of histone H4 has a region of highly basic amino acids, which interacts with the highly acidic surface region of a H2A-H2B dimer of another nucleosome, being potentially significant in the HOS of nucleosomes. This interaction is also thought to occur under physiological conditions and suggests that acetylation of the H4 tail influences the HOS formation of chromatin. The histone tails help to hold hetero-dimer and inter-dimer interactions together (Zheng and Hayes 2003).

Introduction

The complete HO is created from the connections of 3 four-helix bundles between the two (H3–H4) dimers and the two (H2A–H2B) dimers and also with the (H4–H3)–(H3'–H4') tetramer (Chantalat *et al.* 2003). The four-helix bundles are not the only part of HO that serve to maintain the structural integrity. There is also (Fig. 2) a H2A–H3'–H4' molecular cluster (MC) (and equivalently for H2A'–H3–H4), H2A–H4' β -sheet docking (BS) (and correspondingly for H2A'–H4) and H4'–H2B docking (H42B) (and equivalently for H4–H2B'). There is an important interaction of MC with the β -sheet (black regions in Fig. 1). If there is a mutation Y98G of H4, it will bring about not only perturbation of the β -sheet but also of the MC and H42B, leading to the disruption of the nucleosome (Santisteban *et al.* 1997).

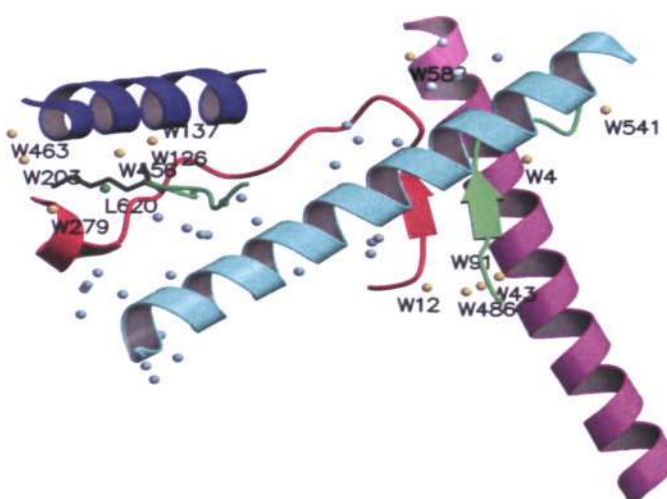


Figure 2. Image showing BS, MC and H42B interaction regions. H2A, red docking sequence; H4', green docking sequence; H3', blue α N helix; H2B, magenta α 2 helix; H3', cyan α 2 helix; the waters associated with the docking sequences are shown in gold; the waters involved in stabilizing the α 2 H3' helix within the molecular cluster are shown in sky blue; chloride L620 is shown in lime green; Lys44 of H4' is shown in dark green (The figure is adapted from Wood *et al.* 2005).

The tetramer complex is very stable and consists of two (H3–H4) hetero-dimers, which have a 'handshake' interlocking protein fold related in structure to that of (H2A–H2B) hetero-dimers. Histone fold domains arrange the central 121 base pair of DNA, and the rest of additional DNA *i.e.* 13 base pair at each end, which are positioned at the

Introduction

N-terminal extension of the H3 histone fold. Three unique main DNA-binding modes are contributed by each of the histone hetero-dimers in the form of two motifs, which are referred to as L1L2 and $\alpha 1\alpha 1$. These binding types are arranged in the following order - L1L2, $\alpha 1\alpha 1$, L1L2, which are spaced ~ 10 base pairs apart. The HO has an overall pseudo two-fold symmetry. Besides, each histone hetero-dimer has an *intra*-dimer pseudo two-fold symmetry axis (running through the $\alpha 1\alpha 1$ DNA-binding motif), and the two hetero-dimers on each side of the overall two-fold are related by an additional *inter*-dimer pseudo two-fold symmetry axis (Luger *et al.* 1997a; Davey *et al.* 2002).

1.2. Histone post-translational modifications

Modifications in histone proteins were discovered in the mid 1960's and it was predicted to affect transcription (Allfrey and Mirsky 1964). In general, it was found that the early post-translational modifications were highly concentrated within the tail extension regions, which protrude from the nucleosome core, leading to two main theories pertaining to the mechanisms of histone modifications. The first one suggested that the histone tail modifications may affect electrostatic interactions between the histone tail and DNA to loosen the chromatin structure. Later on, it was proposed that the various combinations of these modifications may generate the binding epitopes which recruit other proteins (Strahl and Allis 2000). It has been shown that more modifications occur in the globular regions of histones as opposed to tails. Hence, it has been put forward that these modifications may affect DNA-histone (Cosgrove *et al.* 2004) and histone-histone interactions within the nucleosome core region (Ye *et al.* 2005). Some of the common histone modifications are acetylation, methylation or ubiquitination of lysine; methylation of arginine and phosphorylation of serine. A few of the modifications have been shown to be correlated with gene silencing; others seem to be correlated with gene activation. The information stored in this way is considered epigenetic since histone modification is not encoded in the DNA, but it is still inherited by progenitor cells. The conservation of the repressed or activated status of the gene is often necessary for cellular differentiation (Felsenfeld and Groudine 2003; Cosgrove and Wolberger 2005).

Introduction

1.3. Histone variants

Histone proteins are conserved in higher organisms, whereby only a handful of variants have been identified. This diversification of histones is observed for H2A and H3, while H2B and H4 are typically invariant. Histone protein H2A substituted by H2A.Z gives increased nucleosome stability (Kumar and Wigge, 2010). Moreover, H2A.X protein is associated with T cell differentiation and DNA repair, whereas inactive X chromosomes are enriched with macroH2A, especially in mammals. H3 can be replaced by H3.3, which correlates with activation of genes, and in centromeres H3 is replaced by centromere protein A (CENPA) (Felsenfeld and Groudine 2003).

1.4. Structure of nucleosome core particle

As the basic repeating unit of chromatin, study of NCP enables us to understand how chromatin permits site-specific access to regulatory factors. Accurate depiction of NCP at atomic level illuminates the properties of chromatin that result from nucleosome positioning and mobility as well as provides an understanding of nucleosomal dynamics (Richmond and Davey 2003). Nucleosomal studies provide information on the local and global scales (Lavelle and Benecke 2006). Locally, we are able to unveil the genetic control (Segal *et al.* 2006), such as gene insulation function, the structure of chromatin fiber and site-selectivity of DNA binding drugs, divalent metals or other regulatory factors. On a global level, we can derive the overall chromosome structure, dynamics and mechanism of nucleosome exclusion that play a role in processes such as meiotic recombination or fragile site formation (Hsu and Wang 2002).

In the last decade, many new discoveries on nucleosomes and chromatin function were made. Among those was the X-ray structure of NCP solved at 1.9 Å resolution, which provided thorough information about the DNA structure on NCP and the binding of histones to DNA, which dictates the conformation of the DNA in the NCP (Davey *et al.* 2002; Richmond and Davey 2003; Figure 3). Furthermore, it furnished diminutive details on the positions of metal ions binding to the NCP. In total, 18 ions could be identified. Fourteen of them were Mn^{2+} and 4 of them were Cl^- . Chloride ions were observed in the HO. Out of the 14 Mn^{2+} ions, thirteen were bound to DNA and only one to the protein. The high resolution structure also helped to visualize the histone tails

Introduction

(Davey *et al.* 2002), which were difficult to see in the previous 2.8 Å resolution structure of NCP (Luger *et al.* 1997a). In addition, the high resolution aided in modeling water molecules into the structure. A total of 3130 water molecules were identified (Fig 4).

In general, Mn^{2+} ions found in the NCP structure were observed in the major groove of nucleosomal DNA, especially bonding with GG and GC steps via 3 or 4 bond modes (direct coordination and through hydrogen bonds with water molecules) (Davey and Richmond 2002). As an exception to this, manganese ion was found at only one location of the minor groove of nucleosomal DNA. In this minor groove binding, Mn is comprehensively hydrated and maintains its entire octahedral hydration shell, similarly to Mg *in vivo*, which has same coordination geometry and similar ionic radius. Therefore, it has been used successfully as a substitution for Mg in many experiments (Wu and Davey 2010.) Mn binds in the minor groove of one NCP and interacts with the α C-helix of histone H2B of a neighboring NCP through three of its water ligands. The other three water ligands, which are deep inside the minor groove, form contacts with adenine, guanine and thymine base acceptor groups.

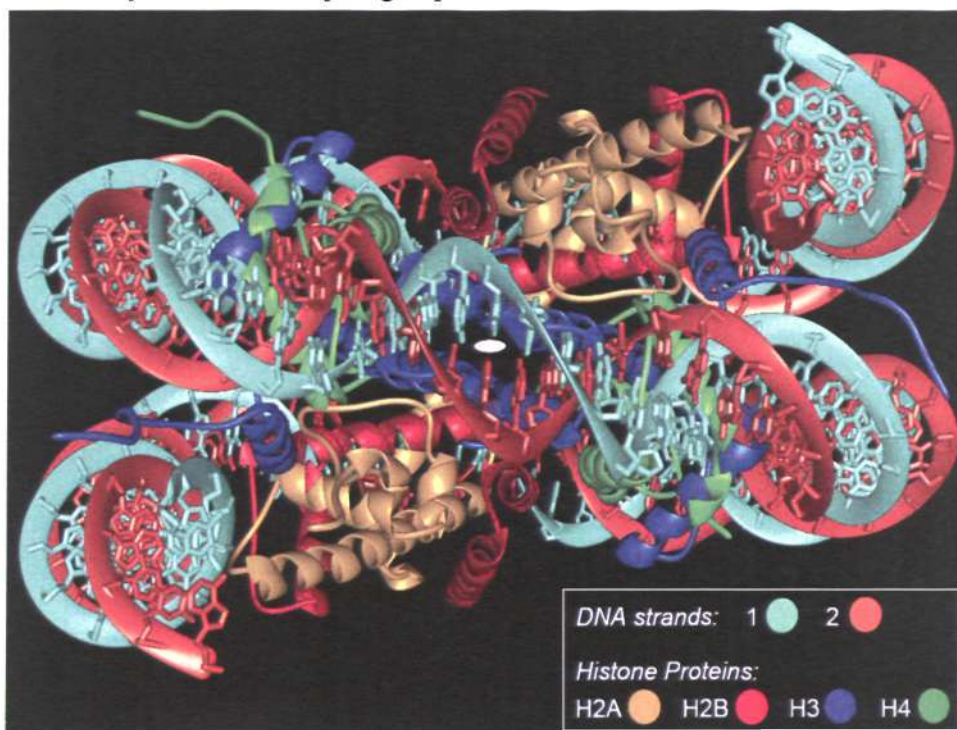


Figure 3. Crystal structure of the NCP. View of the NCP147 down the pseudo dyad axis (white oval) with the DNA superhelix axis running vertically (The figure is adapted from Davey *et al.* 2002).

Introduction

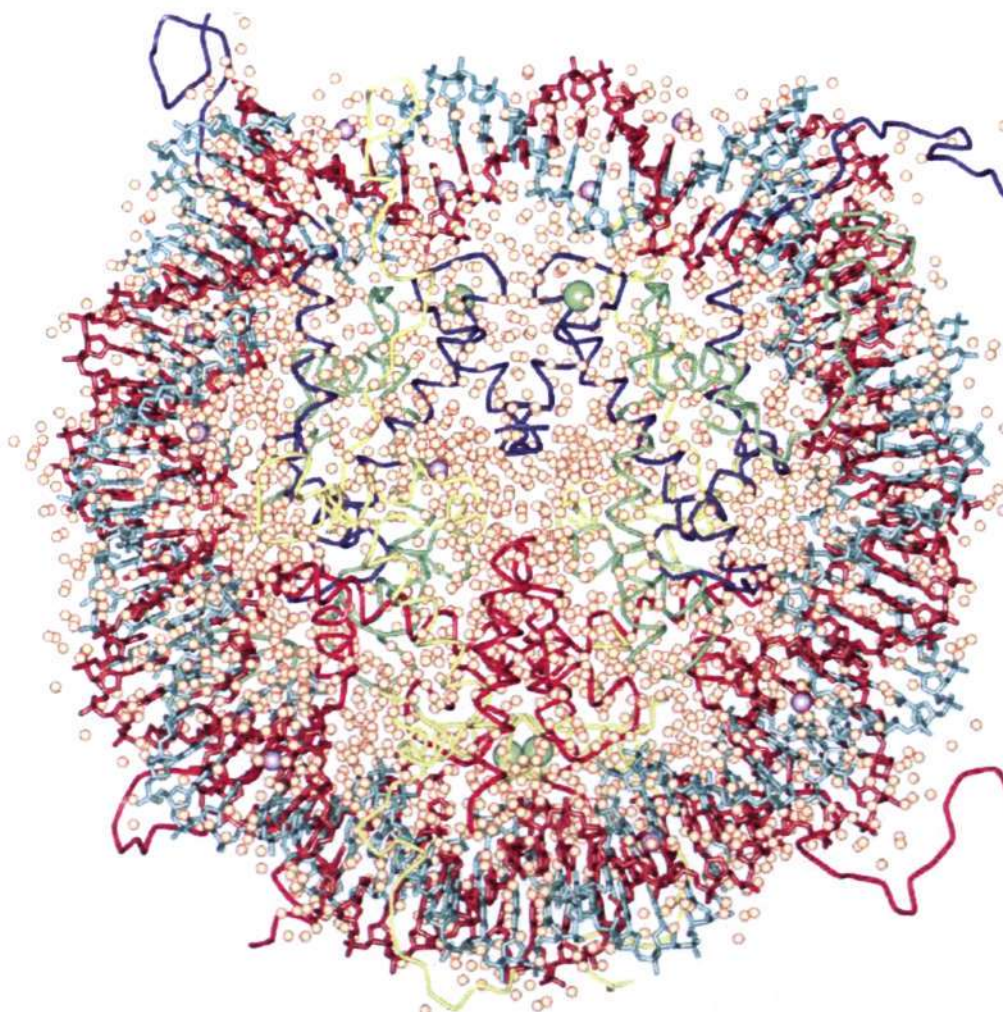


Figure 4. 1.9 Å structure of NCP147 showing its solvation state. Manganese ions (violet), water molecules (gold), and chloride ions (green). DNA strands are shown in cyan and brown. Histones are shown as: H2A yellow, H2B red, H3 blue and H4 green. The N-terminal histone tails are not shown in their entirety (The figure is adapted from Davey *et al.* 2002).

Moreover, a single manganese ion was found to bind to histone in the nucleosome core inter-particle region protein-protein contact site. The octahedral coordination of manganese ion is particularly well-ordered, where Mn^{2+} forms a bond with the carboxylic oxygen atom of H3-ASP77 from one particle and with the peptide carbonyl oxygen atom of H2B-VAL45 of the other. The metal also has four other water ligands. These ordered

Introduction

water molecules form contacts with seven protein acceptor groups coming from an aspartate, a glutamate and a glutamine side-chain, and three main-chain carbonyl groups distributed between both of the particles. This manganese binding site involves the C terminus of the H2B- α 1 helix that adds electrostatic stabilization from the helix dipole. Hence, it indicates that metal mediated interaction is likely necessary for the inter-particle stabilization. In contrast, the other symmetric site of the inter-particle, protein-protein contact site does not have the metal ion.

1.4.1. Structural aspects of DNA in NCP

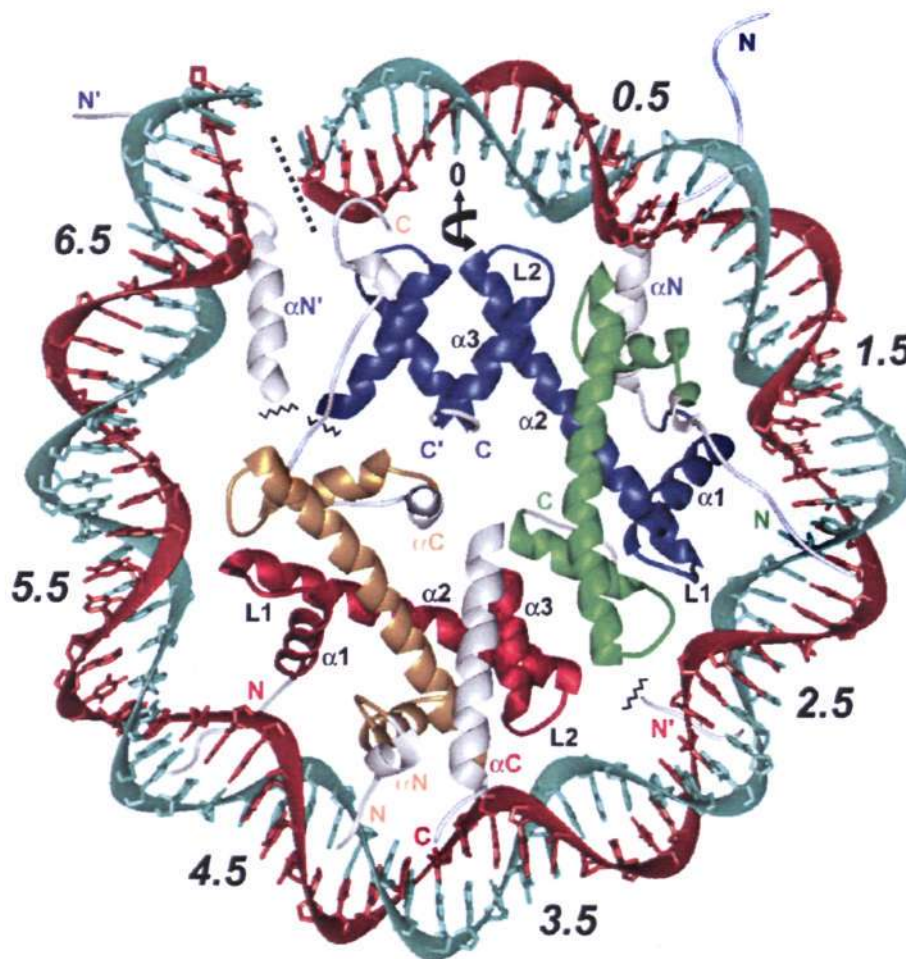
The exterior of the HO is highly positively charged, which plays a significant role in the organization of DNA. The negatively charged DNA backbone encircles the positively charged HO in ~ 1.65 turns of an irregular super-helix. The DNA helix axis has a variable pitch of ~ 26.5 Å and a variable radius of ~ 42.5 Å (Finch *et al.* 1981; Bentley *et al.* 1984). Histone octamer creates a high degree of structural distortion to DNA in the nucleosome (Richmond *et al.* 1984). It is also able to release the DNA in a coordinated manner when required. The DNA bases do not come into direct contact with protein and thus exhibit a high degree of mobility. Along the length of DNA, bending is distributed and it is also seen to occur into both the major and minor grooves. The midpoint of the bound DNA to HO is termed the dyad or central base pair (0), from which each copy of H2A, H2B, H3 and H4 can be related to its partner by an axis of two-fold symmetry (Prunell and Kornberg 1982).

In the NCP, the major and minor grooves of DNA alternately facing the HO create a total of 14 super-helix locations (SHL) (Luger 2003). The point “0” indicates the dyad axis of NCP (Fig. 5). The interaction between HO and DNA is mainly formed by about 120 direct or water-mediated hydrogen bonding interactions between the DNA phosphate backbone and protein elements. Although nucleosomes have a propensity for certain specific DNA sequences, they are capable of binding practically to any sequence, in part due to the flexibility in the formation of water-mediated interactions. Additional interactions are accomplished through insertion of arginine side-chains into the minor groove, which forms van der Waals contacts with sugar groups to help the compression

Introduction

of DNA towards the minor groove. The distribution and strength of DNA binding sites on the octamer surface distorts the DNA within the nucleosome core.

There are eight sites of super-helix locations - $\pm 1, 2, 4$ and 5 , related roughly to base pairs - $\pm 10, 20, 40$ and 50 from the nucleosome center base pair (0), which involve bending into the DNA major grooves where the DNA appears particularly deformed. When DNA bends, all of the grooves on the inside of the circle (both major and minor) must narrow somewhat due to the compression associated with bending, while those on the outside of the curve become correspondingly wider. In addition, the non-uniform bending of the DNA within NCP results in twist defects. The twist of free B-form DNA in solution is 10.5 bp per turn, varying based on the position in the NCP. On the other hand, the overall twist of nucleosomal DNA is only on average ~ 10.2 bp per turn, varying from a value of 9.4 to 10.9 bp per turn (Widom 2001).



Introduction

Figure 5. One half of NCP147. The DNA binding motifs of the histone pairs (L1L2 and $\alpha 1\alpha 1$) are indicated. SHL is denoted by numbers corresponding to double helix turns from the dyad axis ("0"). Histones are shown as: H2A yellow, H2B red, H3 blue and H4 green (The figure is adapted from Davey et al., 2002).

1.4.2. Interactions of DNA and Histone Octamer within NCP

Histone octamer binds primarily to the sugar phosphate backbone of the DNA, which is not continuous, but occurs over the short stretches of each DNA helical turn where the minor groove faces inward toward the HO surface (backbones of both DNA chains). Bond formation between DNA and histones is not specific, but it takes place via extensive salt bridges and hydrogen bonds to the phosphate groups, which are contributed by both main and side-chain groups. These include the 'non polar' contacts with the DNA sugar groups and the electrostatic interactions of the positively charged amino acids N-termini of α -helices with DNA phosphates (Luger and Richmond 1998). Conversely, there are several minor base contacts, which include the hydrophobic contact of the 5-methyl group of thymidine in the major groove (Luger et al., 1997).

Furthermore, there are two additional modes of histone-DNA contacts, which are particularly significant. First, with one exception, whenever the minor groove faces inward towards the HO, an arginine side-chain is inserted into the minor groove. The side-chains of arginine also form many salt bridges to the phosphodiester backbones on both sides of the minor groove. In order to avoid the side chain penetrating deeply into the minor groove and forming the base-specific contacts, almost all arginine residues are held by additional hydrogen bonds to protein functional groups (Luger and Richmond 1998).

Moreover, all the core histones have N-terminal domains, which are highly positively charged consisting of about 10 to 40 amino acids. They are known as 'tail domains' because they are greatly extended and mobile. The N-terminal tails of both H2A subunits stretch over the DNA along the minor groove, whereas the tails of the H2B and H3 pass between the gyres of DNA, threading through adjacent minor grooves and extending out from the nucleosome core particle. Therefore, the H2A, H2B and H3 N-terminal tail domains jointly bracket turns of DNA, going over and between the DNA gyres (Widom 2001).

Introduction

Histone tail and DNA interactions may have an influence on the energetics and dynamics of DNA wrapping. These interactions have been studied by measuring free energy of different DNA sequences using enzyme digestion and EMSA (Thastrom *et al.* 2004). Furthermore, these tail domains are of principal interest due to their role and interactions with numerous gene regulatory proteins and also because they are the sites of numerous post-translational modifications that are associated with nucleosome function. In this context, H4 tail domains are implicated in stabilization of higher order chromatin folding (Widom 1986; Fletcher and Hansen 1995; Widom 1998).

1.5. Significance of nucleosome organization

The nucleosome is the basic packaging component of DNA within the nucleus, and it is the primary determinant of DNA accessibility (Li and Widom 2004). On longer DNA molecules, such as that *in vivo*, nucleosomes can be located at many possible sites on the DNA. This phenomenon is known as nucleosomal positioning. Most nucleosomes in a nucleus are built with the same set of histone proteins, but are associated with different DNA sequences (Satchwell *et al.* 1986). Sequence-dependent structural and mechanical properties of DNA, and therefore the ability of a DNA molecule to bend around the HO are thought to be a major determinant of nucleosomal positioning.

Furthermore, it is helpful to make a distinction between two positioning parameters: a 'translational signal' that marks where the HO is placed on the DNA and the 'rotational setting' that defines the curvature and the side of the DNA that faces the histones (Travers and Klug 1987). These parameters are very much dependent on each other, since changing of one will affect the other. A translational shift by ten base pairs maintains the rotational setting, whereas a shift of five base pairs can make the DNA inner surface move outside of the HO (Hokestra *et al.* 1998).

Nucleosomal positioning is affected by various parameters, such as:

- (a) intrinsic DNA bending that favors wrapping of DNA around the HO resulting in rotationally positioned nucleosomes (Travers and Klug 1987). Many studies have demonstrated that the DNA in the nucleosome core shows a preference for alternating (A/T)₃ and (G/C)₃ elements with a total

Introduction

period of about 10.2 bp. This suggests that sequences such as (A/T)₃ are favored at sites of minor groove compression and sequences like (G/C)₃ are favored at major groove compression respectively. On the other hand, long sequences of poly(dA:dT) tracts illustrate an unusual rigid structure in solution, which are not found in the center of nucleosomes (Satchell *et al.* 1986; Shrader and Crothers 1989).

(b) proteins other than histones, including ACF (ATP – utilizing chromatin assembly and remodeling factor) and RSF (remodeling and spacing factor) protein (Becker 2002).

(c) proximally positioned nucleosomes or DNA that does not assemble into nucleosomes influencing the neighboring regions called a “boundary” effect (Kornberg 1981). It was shown that the exchanging nuclease-sensitive region in yeast chromatin could alter position of nucleosomes in flanking regions.

(d) chromatin folding inducing rearrangement.

In vitro, HOs do not exchange freely between different DNA molecules in a given chromosome under physiological conditions, yet they have the surprising ability to glide along DNA, yielding new nucleosomal positions. This process is referred to as nucleosomal mobility or sliding (Becker 2002). Nucleosomes reconstituted onto the 5S DNA positioning sequence were able to reposition themselves translationally onto adjacent sequences upon heating (Pennings *et al.* 1991). This thermally induced repositioning did not disrupt the HO but was consistent with nucleosomes being able to “slide” along the DNA *in cis*.

In vivo, nucleosomes are intrinsically mobile; eukaryotes have evolved a large family of ATP-dependent chromatin remodeling enzymes to alter chromatin structure, many of which do so by means of nucleosome sliding. The physical properties of nucleosomes depend on conditions such as ionic strength and histone modification state. Divalent ion concentration may play an essential role in controlling the properties of nucleosomes, like positioning and mobility, as well as by modulating interactions with nuclear factors (Davey and Richmond 2002).

Introduction

Many biochemical experiments and crystallization studies (Luger *et al.* 1997a; Luger *et al.* 1997b; Davey and Richmond 2002; Davey *et al.* 2002; Richmond and Davey 2003) have deciphered several aspects of NCP organization and structure. These studies have shown that different DNA sequences have different binding affinity towards histone octamer (Luger 2003; Kelbauskas *et al.* 2007). Most NCP structural studies however have made use of 147 bp palindromic sequence derived from human α -satellite DNA and related palindromic DNA molecules due to superior crystal packing, which in turn results in better diffraction quality. However, it is essential to study the structure of the nucleosome core particle with a variety of DNA sequences to gain more insight into the structure of the numerous sequence-unique nucleosomes found in the genome. Designing DNA sequences that can bind to the HO with high affinity is one possible avenue for structural characterization.

2. HEAVY METALS AND CANCER

The most challenging disease of our times, cancer, is caused by various factors, one of which is exposure to heavy metals. Metals that are carcinogenic to humans, such as As, Be, Cd, Cr and Ni as well as metalloid compounds have been appraised by the International Agency for research and cancer (IARC), and classified as group I carcinogens. There are more elements emerging from current research, including Co, Cu and Fe (Bal and Kasprzak 2002). These elements are spread all over the periodic table and accordingly, their chemical properties are quite diverse.

Most cancers induced by heavy metal exposure occur in workers from the mining and refining industries. Various epidemiological studies have shown clearly that the exposure to metals has both toxic and carcinogenic affects on animals as well as on humans (Valko *et al.* 2005). Entry of heavy metals into the human body occurs through food, water, air or absorption through the skin. Industry is the major source of heavy metal exposure in adults during manufacturing in the pharmaceutical, industrial or residential settings, while ingestion of the polluted items is the most common route of exposure in children (Robert 1999). There are other pathways in which heavy metals cause poisoning less frequently, such as a radiological procedure, from inappropriate dosing or monitoring during intravenous nutrition or from a broken thermometer (Smith *et al.* 1997).

Basic metabolic functions are hampered by heavy metals in two ways. First, they accumulate in soft tissues due to improper metabolization and become toxic by disrupting the function of vital organs and glands such as the heart, brain, kidneys, etc. Second, they dislodge vital nutritional minerals from the body and inhibit proper biological function. For instance, enzymes are catalysts for nearly every biochemical reaction in all life-sustaining processes of metabolism. Most enzymes require Mg^{2+} , Ca^{2+} or Zn^{2+} for their enzymatic reactions, but heavy metals such as nickel or cadmium may displace them. These toxic metals cannot play the same role as the nutritional minerals and thus their presence becomes detrimental to enzyme activity.

Symptoms due to acute heavy metal toxicity are usually severe, rapid in onset, and associated with a known exposure or ingestion, which leads to cramping, nausea and

Introduction

vomiting, pain, sweating, headaches, difficulty in breathing, impaired cognitive, motor and language skills, mania, and convulsions (Ferner 2001). The symptoms of toxicity resulting from chronic exposure include impaired cognitive, motor, and language skills, learning difficulties, nervousness and emotional instability, and insomnia, nausea, lethargy, and feeling ill. However, these symptoms are more difficult to associate with their cause. Symptoms of chronic exposure are very similar to symptoms of other health conditions and often develop slowly over months or even years. Sometimes, the symptoms of chronic exposure actually abate from time to time, leading the person to postpone seeking of treatment, thinking that they are related to something else. Allergies are frequent and repeated long-term contact with some of the metals or their derivatives may cause cancer (IOSHIC 1999).

2.1. Role of oxygen in metal-mediated DNA damage

Molecular oxygen is essential for aerobic life forms, and it is also the worst abetting carcinogenic molecule that we must endure during our whole lifetime. This means that we must be cautious to manage a proper reserve of intracellular reducing potential. Trace metals exceeding the physiological levels are highly toxic, since a number of metals are capable of generating free radicals. In general, there is a fine balance within each cell between antioxidants and free radicals. Free radicals have one or more unpaired electrons in their outer orbitals, in contrast to non-radical species that have pairs of electrons with antiparallel spin. Thiol group (-SH)-containing molecules are the most important factors in the maintenance of cellular redox homeostasis. Under certain conditions a thiol group may lead to formation of thiyl radicals (-S \cdot). These radicals can interact with molecular oxygen and generate reactive oxygen species (ROS) (Karoui *et al.* 1996).

ROS are oxygen-containing free radicals. The mitochondrial respiratory chain, the cytochrome P450 metabolic pathway and the inflammatory responses are the major sources for the endogenous generation of ROS (Inou *et al.* 2003). Exogenously, ROS can be produced by various xenobiotics, such as chlorinated compounds, metal ions and radiation. The superoxide anion radical ($\text{O}_2^{\cdot-}$) is a simple derivative of ambient oxygen. It is produced from complexes I and III of the electron transport chain in mitochondria,

Introduction

with the addition of one electron to molecular oxygen. Superoxide anion can, in turn, react with other molecules and form secondary ROS, such as the hydroxyl radical (OH•), hydrogen peroxide (H₂O₂) and peroxy radical (ROO•) (Valko *et al.* 2006).

Different oxygen species such as singlet oxygen, superoxide anion, hydrogen peroxide and hydroxyl radicals are generated as by-products during aerobic metabolism in somatic cells (Kobayashi *et al.* 1990). Increasing evidence indicates that transition metals act as catalysts in these oxidative processes, and therefore, the toxicities associated with these metals may be due at least in part to oxidative tissue damage (Halliwell and Aruoma 1991). Studies have shown that metals such as iron, copper, cadmium, chromium, lead, mercury, nickel, cobalt and vanadium exhibit the ability to produce reactive oxygen species, resulting in DNA damage, lipid peroxidation, depletion of sulfhydryls and altered calcium homeostasis (Stohs and Bagchi 1995). DNA-oxidative damage induces mutations, which may lead to neoplastic transformation. Such products include modified bases (primarily 8-oxoguanine), abasic sites (primarily depurinated), base adducts of carbon-centered radicals (including DNA-crosslinked proteins), and single and double breaks in the phospho-sugar backbone of DNA (Aust and Eveleigh 1999). Damage in DNA can induce mutations, which may result in accelerated ageing, tumorigenesis and heart diseases (Liang and Dedon 2001). When ROS overcome the cell reduction capacities, they are able to induce lipid peroxidation, depletion of the sulfhydryl groups, altered signal transduction pathways, calcium homeostasis and DNA damage, particularly contributory towards ageing and cancer (Marnett 2000; Cooke *et al.* 2003).

2.2 Metal-mediated mechanisms in carcinogenesis

The key mechanisms involved in metal-induced carcinogenesis are genetic and epigenetic changes, deregulation of cell proliferation and aberrant activation of signal transduction pathways. The most common genetic effects are nucleotide base modifications, single and double strand breaks and DNA-protein cross-linking. The epigenetic effects revealed so far are mainly associated with changes in DNA and histone methylation leading to inappropriate gene-silencing (tumor suppressor protein p53), an event that alters the gene expression profile, promoting tumor development (Salnikow and Zhitkovich 2008). Differentiation and deregulation of cell growth is a typical feature

Introduction

of the cancer phenotype. Metals promote deregulation of cell proliferation by activating various transcription factors that control key cellular responses, such as cell cycle progression and apoptosis. Among them, the nuclear factors NF- κ B, AP-1 and NFAT are included (Leonard *et al.* 2004). Metals modulate gene expression by interfering with signal transduction pathways that plays an essential part in cell growth and development. The classical MAP kinase pathways and the PI3K/Akt/ mTOR cascade are targets of several metals. But most metals are capable of damaging the DNA through oxidative stress.

The majority of DNA damage is carried out by metal-induced free radicals; moreover, metals can also inhibit DNA repair, such as direct damage by free radicals, substitution of zinc in Zn-finger domains, or indirectly by lowering the level of reduced glutathione. Several metals such as Cr, Cd, Ni, Co and As are able to inhibit DNA repair. Therefore, the elucidation of the molecular pathways of metal-induced carcinogenesis is critical for the improvement of risk assessment and for the design of safe metal-based anticancer drugs.

2.3. Metal-induced carcinogenesis and epigenetics

Carcinogenic metals such as Ni, Co, Cd are known to disrupt a wide range of cellular processes, but the specific mechanism by which they exert their carcinogenic activity is not clear. However, current work in the field of metallo-carcinogenesis suggests that the epigenetic mechanisms may play a role in metal-induced carcinogenesis (Arita and Costa 2009). In order to comprehend the role of genetic and epigenetic factors in gene expression, it is essential to include mechanisms underlying the toxicity and cell transforming ability of heavy metals, as well as aberrant changes in gene expression that occur during disease states such as cancer. Two main categories of epigenetic mechanisms known to affect mammalian gene expression at the chromatin level are DNA methylation and histone post-translational modifications.

It is known that the exposure to carcinogenic metals can perturb DNA methylation levels globally, and metals also play a role in gene-specific histone tail post-translational modifications. Expression of genes, however, is not solely determined by DNA sequence, but also depends upon dynamic states of chromatin, for which the

Introduction

fundamental unit is the nucleosome. Most of the previous heavy metal binding studies have been performed using small oligonucleotide DNA, but the geometry of oligonucleotides is quite different from that of the DNA in the NCP (Richmond and Davey 2003). Therefore, the first step to understand the influence of carcinogenic metals on chromatin is to elucidate structurally the binding behavior of these metals to the nucleosome, which could aid in understanding their global impact on genome dynamics and epigenetic mechanisms.

2.4. OBJECTIVES

In order to understand the influence of heavy metals on the nucleosome, we wanted to characterize crystallographically the binding of potentially carcinogenic heavy metals - Ni^{2+} , Co^{2+} , Cd^{2+} , Cu^{2+} , Hg^{2+} and Pb^{2+} to NCP. This study may unveil the site selectivity of heavy metals. Moreover, it may tell us whether the binding of heavy metals is dictated by the structural and sequence context of DNA. Also, the binding of heavy metals to the histone proteins may reveal their role in the modulation of histone post-translational modifications. Furthermore, we wanted to examine the association of the heavy monovalent cations, Rb^+ and Cs^+ , to the NCP.

NCP composed of novel DNA molecules can provide new data on sequence dependent DNA structure as well as details regarding distinctions in DNA conformation or histone interactions at different sites on the octamer. This is important for understanding the basis of the sequence dependence in nucleosome positioning. We wanted to design new DNA sequences that yield well diffracting crystals, which would not only generate new sequence-conformation relationships in the nucleosome, but also provide novel NCP substrates for drug development and factor binding studies. Several NCP constructs were decided to be assembled with non-palindromic DNA sequences containing strong positioning elements and subjected to crystallographic analysis.

MATERIALS AND METHODS

3. MATERIALS AND METHODS

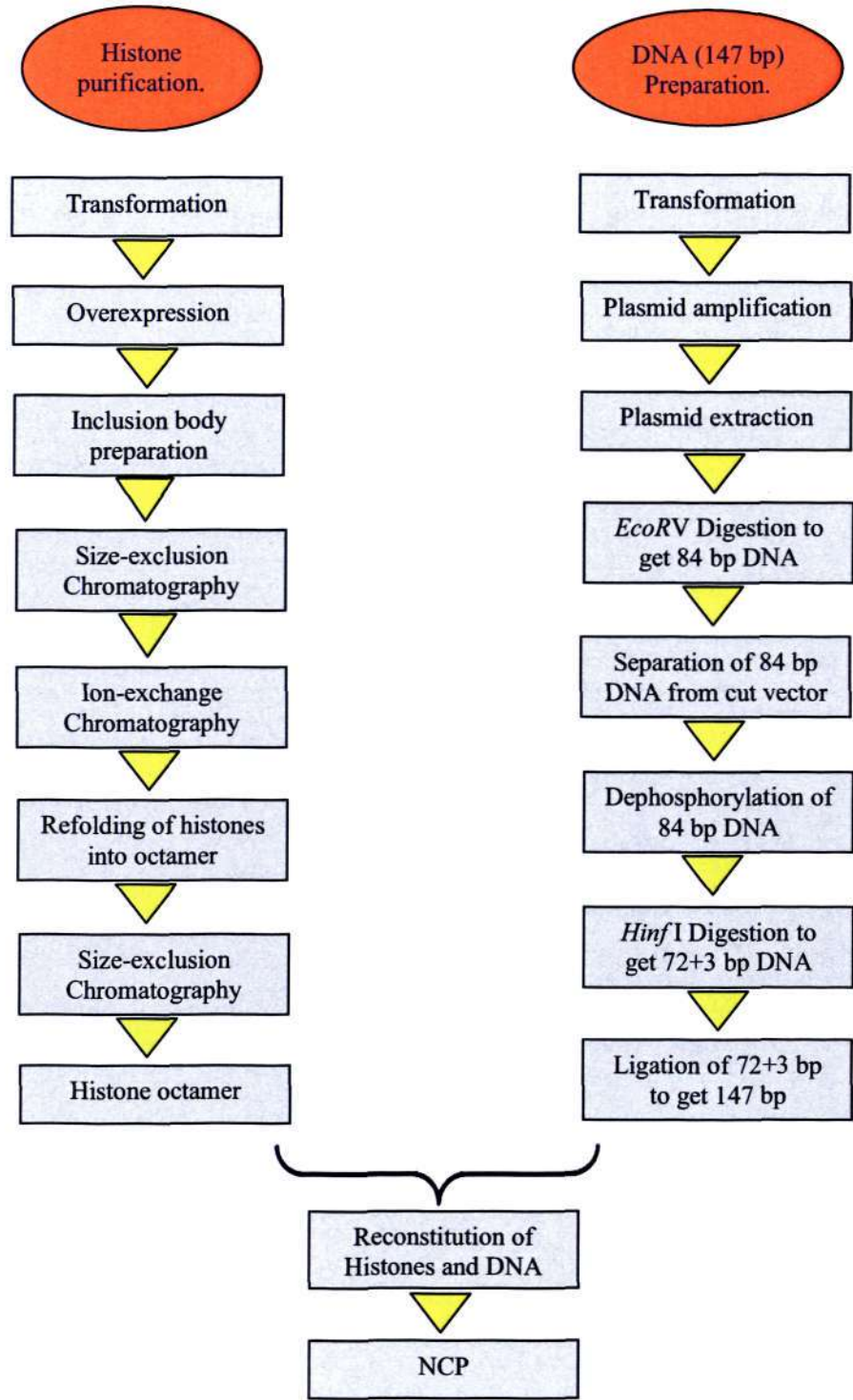
Described in this section are the comprehensive protocols for expression and purification of histones, refolding of HO, reconstitution of NCP and purification of crystallization quality NCP. The cloning strategies for the construction of plasmids containing multiple repeats of defined DNA sequences, and the subsequent large-scale isolation of defined sequence DNA for nucleosome reconstitution, are also described in detail. A flow chart with all the steps involved in the preparation of NCP is given in Diagram 1.

Preparation of NCP from recombinant histone proteins and defined-sequence DNA followed existing protocols (Luger *et al.* 1997b; Dyer *et al.* 2004) with slight modifications for better yield and quality of the materials. Making NCP by recombinant means offers many advantages, such as the ability to combine histone variants and binding of other proteins to NCP, and the opportunity to study the effect of individual metals and drugs on nucleosome structure and function.

All chemical reagents without specific annotation were purchased from Sigma (St.Louis, MO, US). All enzymes and Markers without specific annotation were purchased from New England Biolabs (NEB, Ipswich, MA, USA).

Materials and Methods

Diagram 1. Flow chart showing the preparation of NCP



Materials and Methods

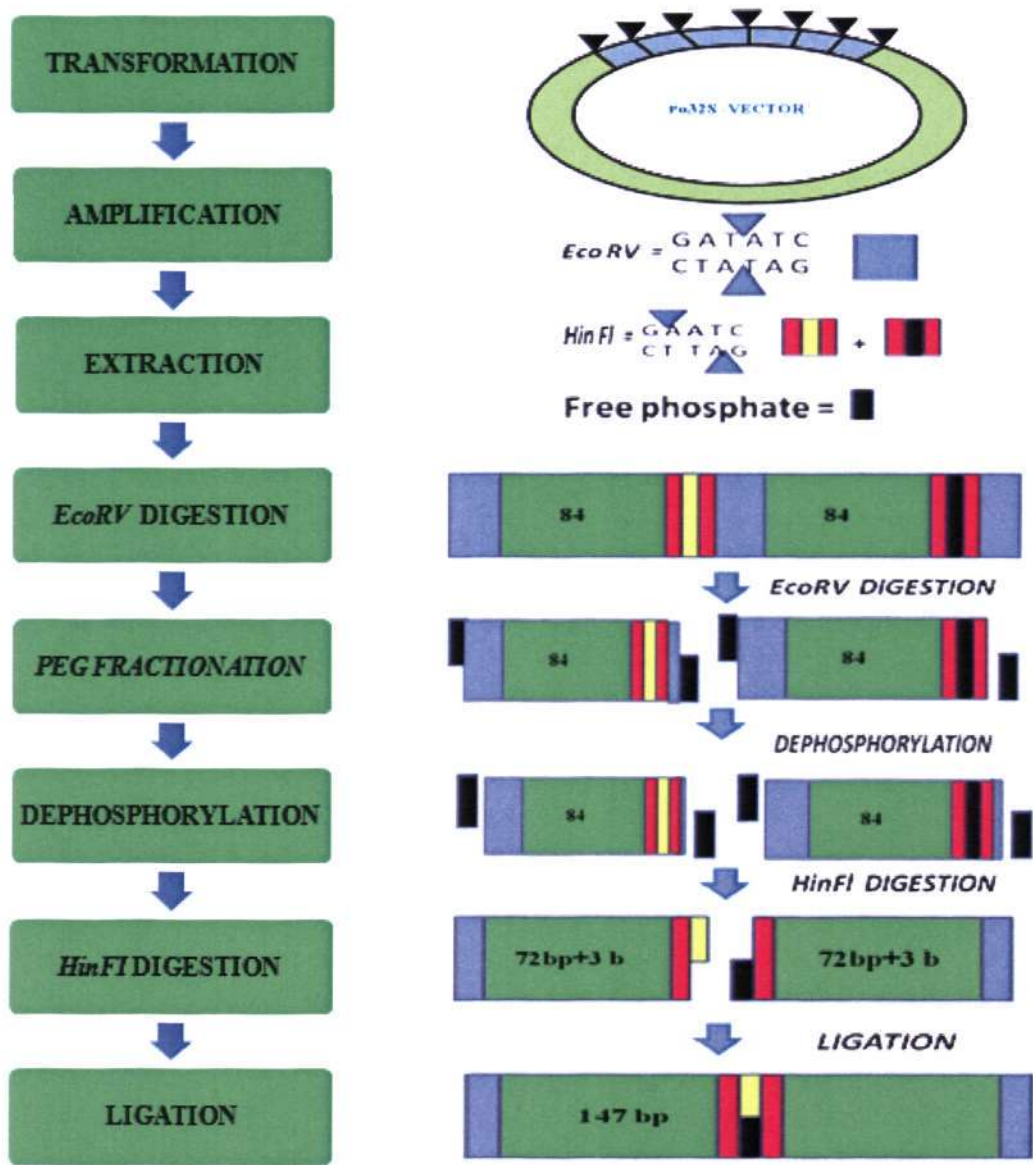
3.1. 147 bp DNA preparation

Thirty two repeats of 84 bp DNA from human α -satellite sequences inserted into a pUC 19 (2.6 K bp size) plasmid vector (hence called pUC- α 32S - 5.3 K bp size) was used. Competent *E. coli* HB101 cells (Promega, Madison, WI, USA) were transformed with this plasmid and amplified to produce ~ 60 milligram of DNA (Richmond *et al.* 1988; Luger *et al.* 1999). Plasmid extraction was carried out using an existing protocol (Sambrook *et al.* 2001), which was slightly modified to get higher yields. Later, the plasmid was digested using *EcoRV* restriction enzyme to get blunt end DNA of 84 bp. Then, these inserts were subjected to dephosphorylation with calf intestine alkaline phosphatase (CIAP) to remove the terminal phosphate group in order to avoid self ligation in the subsequent step. This CIAP treated DNA was digested with *HinfI* to get 72 bp with an overhang of 3 bases. This product was purified using ion-exchange chromatography, followed by ligation using T4 ligase to obtain the required palindromic 147 bp DNA. The sequence of a single strand of the 147 base long DNA is given below, followed by a flow chart showing the steps involved in the preparation of 147 bp DNA (Diagram 2).

5'ATCAATATCCACCTGCAGATACTACCAAAAGTGTATTTGGAAACTGCTC
CATCAAAAGGCATGTTTCAGCTGGAATCCAGCTGAACATGCCTTTTGATGG
AGCAGTTTCCAAATACACTTTTGGTAGTATCTGCAGGTGGATATTGAT3'

Materials and Methods

Diagram 2. Flow chart showing the preparation of 147 bp DNA



3.1.1. Transformation

One hundred ng of pUC- α 32S plasmid was mixed with 50 μ l of competent *E. coli* HB101 cells and incubated on ice for 10 minutes. Later these cells were heat-shocked for 45 seconds at 42°C. The tube was immediately transferred to ice and cooled for 5 minutes. Then, 450 μ l of cold 2X TYE medium was added and mixed gently, followed by

Materials and Methods

incubating the tubes in a shaker incubator at a speed of 220 revolutions per minute (rpm) for 1 hour at 37 °C. The transformed bacterial cells were diluted sequentially in the following order (1X, 10X, 100X and 1000 X) and spread on four 2X tryptone yeast extract (TYE) agar plates containing the antibiotic ampicillin at a concentration of 100 µg/ml. The various dilutions were intended to yield well separated colonies. The plates were incubated for 12 -16 hours at 37 °C.

3.1.2. Plasmid amplification

In general, an agar plate with the least crowded and well separated colonies was selected, from which five single, large colonies were picked for DNA amplification. These colonies were used to inoculate individual culture tubes containing 4 ml each of Terrific Broth (TB) medium with ampicillin (100µg/ml). In order to get the exponential phase of *E. coli* cells, these tubes were incubated at 220 rpm for about 4-5 hrs at 37 °C in a shaker incubator. Then, the content from all the 5 tubes were transferred to a 500-ml flask containing 100 ml TB medium with ampicillin (100 µg/ml). This 100 ml culture was incubated at 37 °C in a shaker incubator at 220 rpm until the medium appeared turbid. The culture medium was then evenly distributed into fifteen 2-liter flasks containing 500 ml each of TB medium with ampicillin (100 µg/ml) and incubated in a shaker incubator at 220 rpm for about ~18 hrs at 37 °C.

3.1.3. Plasmid extraction

Fully grown culture was centrifuged at 8000 g for 7 min in 500 ml. The harvested cells at this stage could be stored at -20 °C. The thawed cell pellets in each centrifuge bottle were mixed using a sterile glass rod until they became homogenous. To each centrifuge bottle, 60 ml of Alkaline Lysis Buffer I was added gradually in order to homogenize the bacterial pellets. After properly suspending the bacterial cells, 120 ml of Alkaline Lysis Buffer II was added into each of these bottles, and this mixture was shaken vigorously. Once these were thoroughly mixed, they were let to cool down on ice for 20 minutes with intermittent shaking every five minutes. Finally, 210 ml of cold Alkaline Lysis Buffer III was added into the bottles and mixed immediately but gently.

Materials and Methods

These bottles were incubated on ice for 20 minutes, and during incubation the bottles were shaken every 5 minutes.

Cell lysate was pelleted down at 10,000 g for 20 min at 4 °C and the supernatant was filtered through a stack of sterile gauze. To this filtered lysate, 0.52 volume of isopropanol was added and allowed to stand for 30 minutes to aid in the precipitation of plasmid DNA. The precipitated mixture was then transferred to a set of clean 500 ml fresh centrifuge bottles and centrifuged at 15,000 g for 20 minutes at 20 °C. The pellet was air dried for 1 hr, transferred to two 50-ml polycarbonate tubes and dissolved in 10 mM Tris - 50 mM EDTA (TE 10/50) buffer followed by vigorous vortexing in order to maximize the suspension of the pellet. 120 µl each of 10 mg/ml RNase A was added to each tube and incubated overnight at 37 °C to remove all the RNA contaminants.

After the completion of RNase treatment, the insoluble matter was removed by centrifugation at 10,000 g for 10 minutes at room temperature and the supernatant transferred to a Teflon tube. To this tube, an equal volume of phenol was added and vortexed vigorously, followed by centrifugation at 27,000 g for 20 minutes at 20 °C to remove the protein contaminants. Whenever needed, this phenol extraction step was repeated to remove proteins completely. A Chloroform/Isoamyl alcohol (CIA) extraction step was performed twice and the sample centrifuged at 12,000 g for 10 minutes at 20 °C both times to extract out traces of phenol that get into the aqueous phase containing the plasmid DNA.

Poly Ethylene Glycol (PEG) precipitation was carried out with 10% PEG 6000 and 0.5 M NaCl (final concentration) to remove traces of small molecular weight RNA. The mixture was incubated on ice for 30 minutes followed by centrifugation at 27,000 g for 20 minutes at 4 °C. RNA remains in solution and the DNA gets precipitated. The supernatant was discarded and the plasmid DNA pellet dissolved in 10 ml TE (10/0.1). For complete dissolution of plasmid DNA, the mixture was incubated at 37 °C for a few minutes in a shaker incubator. Subsequently, two rounds of CIA extraction were carried out to remove trace amounts of PEG in the supernatant. Finally, pure DNA plasmid was ethanol precipitated (2.5 volumes of ethanol and 1/10th volume of 4 M NaCl incubated on ice for 1 hr) and resuspended in TE (10/0.1). DNA sample was later analyzed on a 0.7%

Materials and Methods

agarose gel containing 1X Tris acetate EDTA (TAE) buffer to check the quality of purified plasmid DNA (Fig. 6).

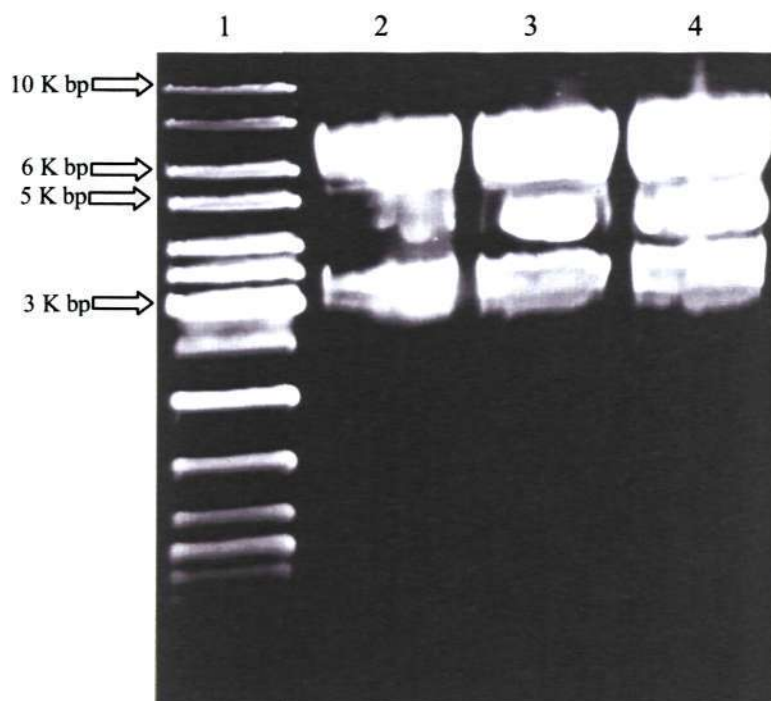


Figure 6. Agarose gel of extracted plasmid. The quality of the purified plasmid vector was verified on a 0.7% Agarose gel in 1X TAE. Lane 1 – 1 K bp Marker (Fermentas, Ontario, Canada); Lane 2 – Control vector (3 µg); Lane 3 – Extracted Vector (4 µg); Lane 4 – Extracted vector (6 µg).

3.1.4. *EcoRV* digestion

The purified pUC- α 32S vector was digested with the restriction enzyme, *EcoRV*. The precursors (84 bp with 5' free phosphate) of the 147 bp DNA were released from the vector. The digested sample was checked on a 10% DNA PAGE in 1X TBE buffer (Fig. 7). The digestion condition used had 2 mg/ml plasmid DNA in a buffer containing 50 mM Tris (pH 7.6), 100 mM NaCl, 10 mM MgCl₂ and 1 mM DTT. *EcoRV* enzyme was added at a proportion of 300 units/mg of DNA. The reaction mixture was incubated with continuous shaking for 24 hours at 37 °C.

Materials and Methods

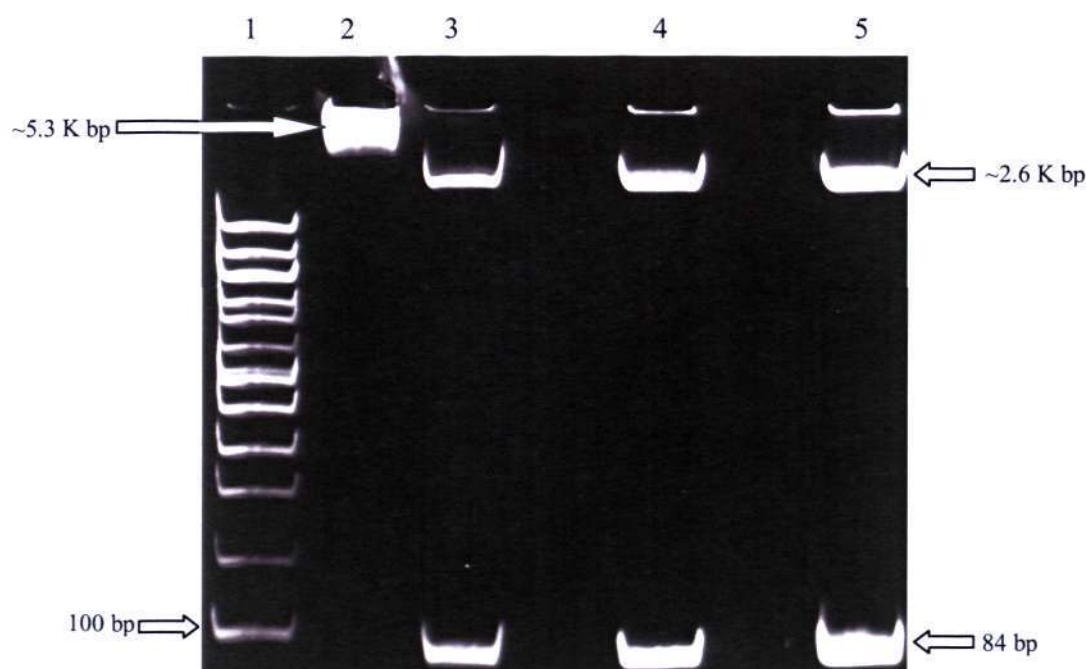


Figure 7. DNA PAGE of *EcoRV* digestion. In order to ensure complete digestion, digested plasmid was analyzed by 10% DNA PAGE in 1X TBE buffer. Lane 1 – 100 bp ladder; Lane 2 – pUC-α32S plasmid; Lane 3 – *EcoRV* digested plasmid (250 ng); Lane 4 – *EcoRV* digested plasmid (500 ng); Lane 5 – *EcoRV* digested plasmid (1000 ng). The absence of 84 bp mutlimers indicates completeness of the digest.

3.1.5. PEG fractionation

After *EcoRV* digestion, the vector DNA was removed by PEG fractionation. The *EcoRV* reaction mixture containing the vector and the insert DNA was mixed with 9.5% PEG6000 and 0.5 M NaCl, and the sample was kept on ice for 1 hour, followed by centrifugation at 27,000 g for 20 min. 84 bp DNA with free phosphate ends was obtained in the supernatant and later, it was analyzed by a 10% DNA PAGE in 1X TBE buffer (Fig. 8). Finally, the sample was ethanol precipitated and resuspended in TE (10/0.1).

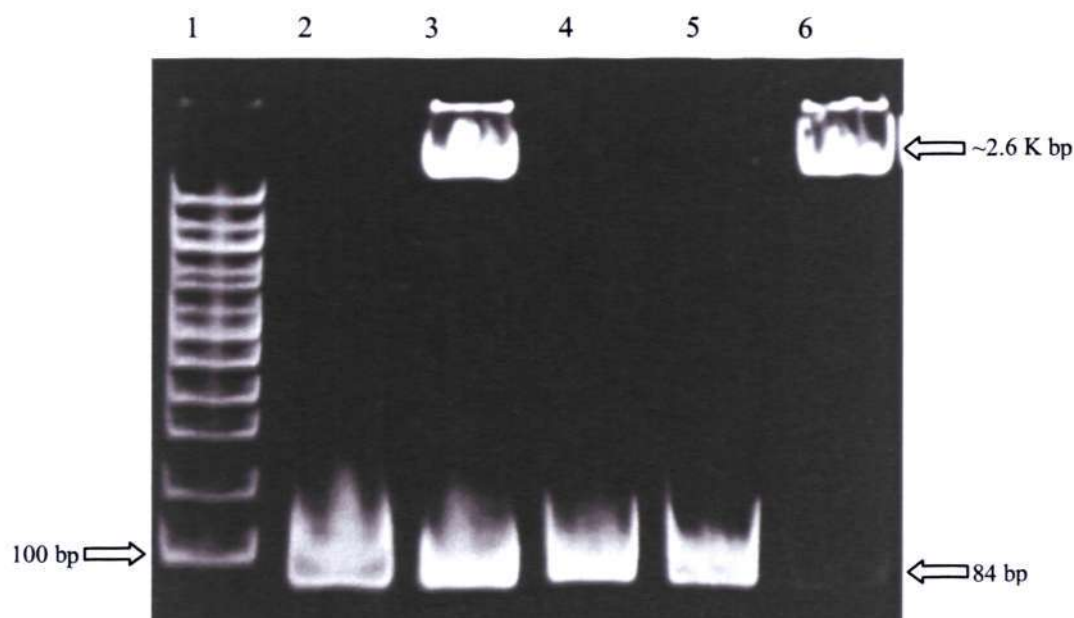
Materials and Methods

Figure 8. DNA PAGE of PEG fractionation. To ensure the separation of 84 bp from vector by PEG fractionation, the sample was analyzed by 10% DNA PAGE in 1X TBE. Lane 1 – 100 bp ladder; Lane 2 – 84 bp control; Lane 3 – Completely digested sample; Lanes 4 & 5 – PEG precipitation supernatant; Lane 6 – PEG precipitation pellet. PEG fractionation was efficient in the separation of 84 bp DNA from the vector DNA.

3.1.6. Dephosphorylation

To ensure the specificity of the end-to-end ligation in the last step of 147 bp preparation, the 5' free phosphate ends should be removed before proceeding to *Hin*I digestion. CIAP was used to perform dephosphorylation. The dephosphorylation reaction setup condition contained 2 mg/ml of 84 bp DNA in a buffer consisting of 50 mM Tris (pH 8.0), 10 mM MgCl_2 and 0.1 mM EDTA. CIAP was added at a ratio of 72 units/mg DNA. The mixture was incubated for 24 hours at 37 °C in a shaker incubator. Dephosphorylated 84 bp was then extracted with a 1:1 phenol-CIA mixture. Once the enzyme and any remaining PEG6000 from the previous step were removed, 84 bp DNA was ethanol precipitated and resuspended in TE (10/0.1). The ligation activity of the 84 bp fragment was tested using T4 ligase on a 10% DNA PAGE in 1X TBE buffer in order to ensure the completeness of dephosphorylation before proceeding to next step (Fig. 9).

Materials and Methods

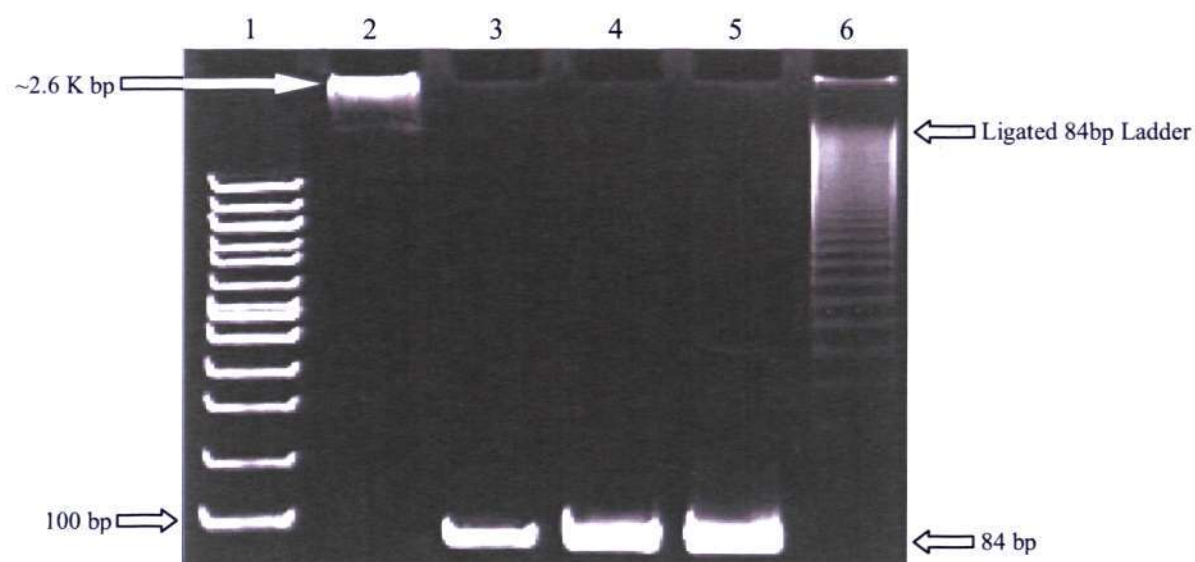


Figure 9. DNA PAGE of dephosphorylation test. The completeness of dephosphorylation of 84 bp was analyzed by 10% DNA PAGE in 1X TBE buffer. Lane 1 – 100 bp ladder; Lane 2 – pUC- α 32S vector; Lane 3 – 84 bp control; Lane 4 – Dephosphorylated 84 bp; Lane 5 – Dephosphorylated 84 bp with ligase treatment; Lane 6 – Undephosphorylated 84 bp with ligase treatment. The dephosphorylation was complete as no ligation products of 84 bp DNA in lane 5 were observed, as compared to Lane 6.

3.1.7. *Hinf*I digestion

Dephosphorylated 84 bp DNA was subjected to digestion using *Hinf*I restriction enzyme to generate 72 bp having a 5' trinucleotide overhang and 9 bp with a 5' trinucleotide overhang (termed 72+3 bp and 9+3 bp hereafter). The *Hinf*I digestion setup condition had 2 mg/ml 84 bp DNA in a buffer containing 50 mM Tris (pH 8.0), 50 mM NaCl, 10 mM MgCl₂ and 1 mM DTT. *Hinf*I enzyme was added at a proportion of 552 units/mg of DNA. The mixture was incubated for 24 hrs at 37 °C. The efficiency of the digestion was analyzed by 10% DNA PAGE in 1X TBE buffer (Fig 10).

Materials and Methods

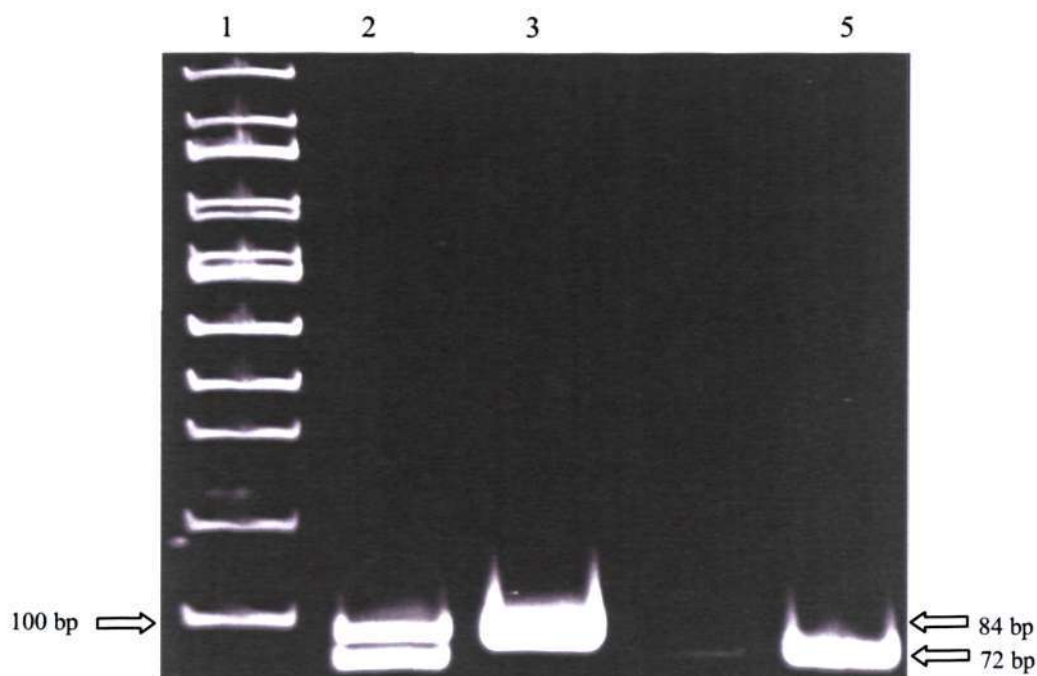


Figure 10. DNA PAGE of *Hin*fi digestion. *Hin*fi digestion of dephosphorylated 84 bp was analyzed by a 10% DNA PAGE in 1X TBE buffer. Lane 1 – 100 bp Ladder; Lane 2 – DNA with and without *Hin*fi treatment (84 bp & 72+3 bp); Lane 3 – 84 bp DNA before *Hin*fi treatment; Lane 5 – 72+3 bp obtained from *Hin*fi digestion. The *Hin*fi digestion was complete as observed on the DNA PAGE.

3.1.8. Purification of 72+3 bp DNA

72+3 bp DNA was separated using a Mono-Q anion exchange column (GE Healthcare, Uppsala, Sweden) connected to an AKTA-FPLC system (GE Healthcare, Uppsala, Sweden). A NaCl concentration gradient from 0.3 M to 1 M in a buffer containing 20 mM Tris (pH 7.4) and 0.1 mM EDTA (pH 8.0) was used in the process (Fig. 11). The 9+3 bp DNA eluted first at about 0.45 M NaCl and the 72+3 bp at about 0.68 M NaCl. The separated fractions were checked for purity on a 10% DNA PAGE in 1X TBE buffer (Fig. 12).

Materials and Methods

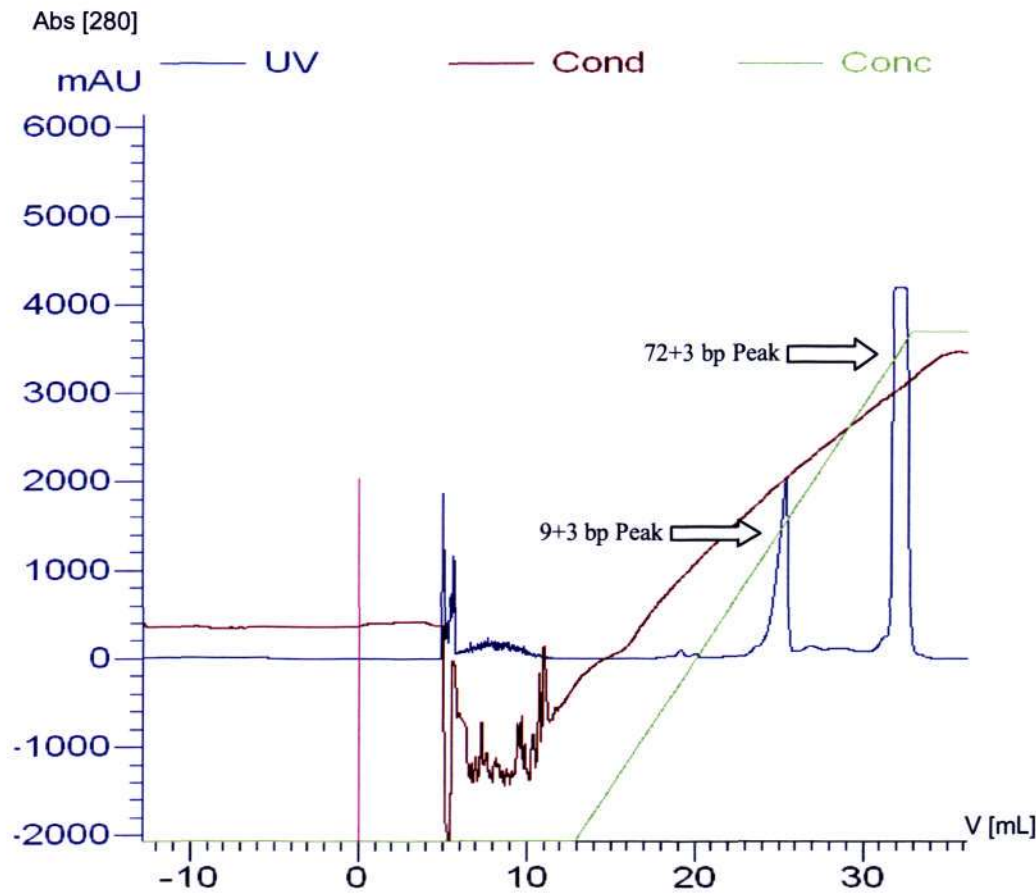


Figure 11. FPLC profile of 72+3 bp DNA purification. Mono-Q anion exchange column was used to purify the 72+3 bp DNA from 9+3 bp after *Hinf* I digestion. 10 mg DNA was injected and passed through the anion exchange column, with a NaCl concentration gradient ranging from 0.3 M to 1.0 M. The plot shows the eluting profile at 280 nm wavelength (blue line) and the NaCl concentration (green line), which increases linearly from 0.3 M – 0.7 M. The 72+3 bp is the second peak, eluting at about 0.68 M NaCl, and the 9+3 bp is the first peak, eluting at about 0.45 M NaCl. The flow rate was set at 1 ml/min throughout the process.

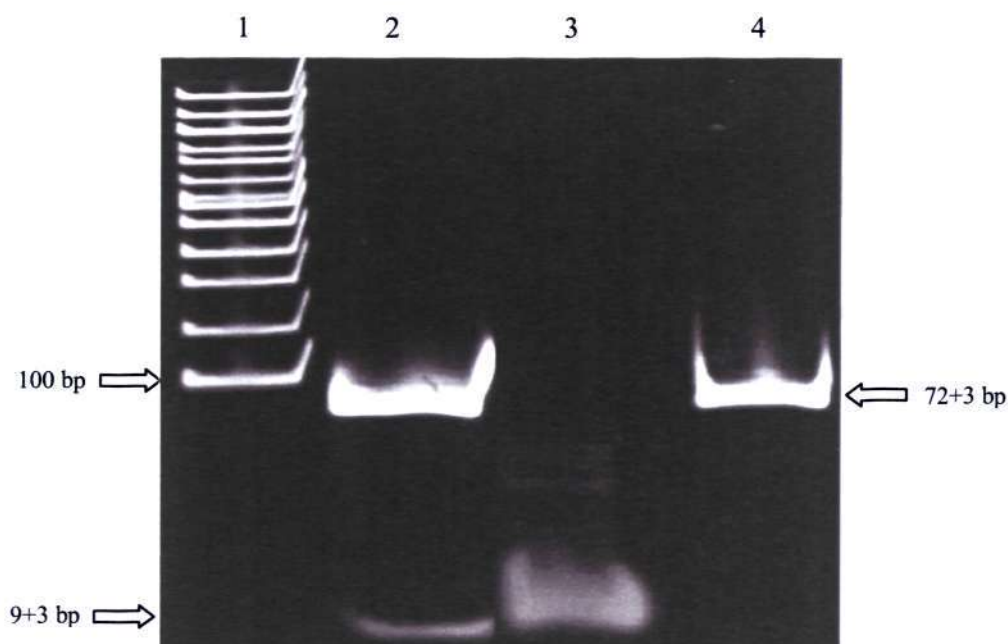
Materials and Methods

Figure 12. DNA PAGE of FPLC purified 72+3 bp DNA. Well separated peak fractions from Mono-Q purification were analyzed by 10% DNA PAGE in 1X TBE buffer. Lane 1 – 100 bp ladder; Lane 2 – sample loaded on to the column; Lane 3 – Peak corresponding to 9+3 bp; Lane 4 – Peak corresponding to 72+3 bp. The gel shows that 72+3 bp was well separated from the 9+3 bp DNA.

3.1.9. Ligation

Ion-exchange purified 72+3 bp DNA was ethanol precipitated and resuspended in TE (10/0.1). It was then subjected to ligation using T4 ligase by incubation at room temperature for 24 hrs and evaluated by a 10% DNA PAGE in 1X TBE buffer (Fig. 13). The ligation reaction contained 2 mg/ml 72+3 bp in a buffer consisting of 100 mM Tris (pH 7.6), 10 mM MgCl₂, 10 mM DTT and 2 mM rATP. T4 DNA ligase was added at a ratio of 1000 units/mg DNA.

Materials and Methods

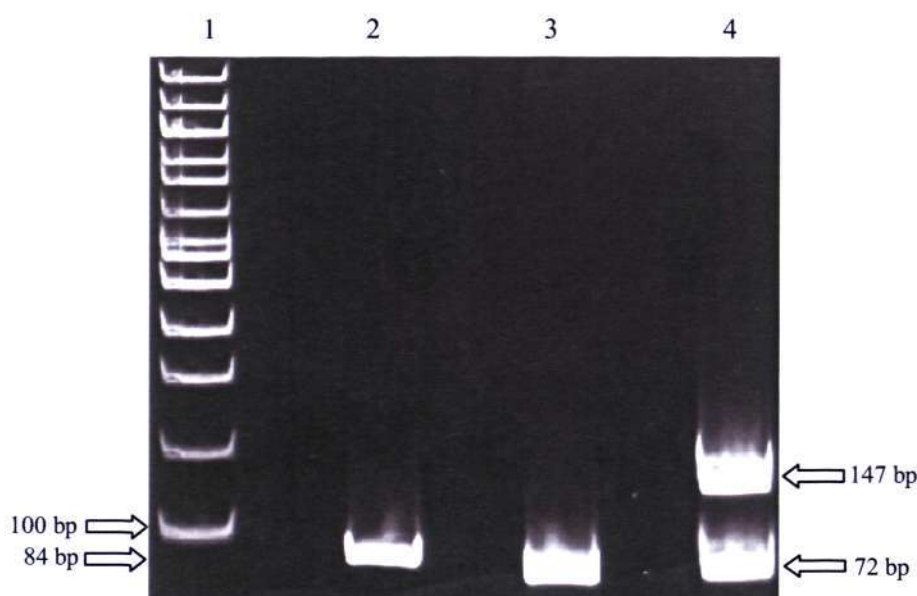


Figure 13. DNA PAGE of T4 ligation reaction. Ligation efficiency and sample purity of the 72+3 bp fragment was analyzed by a 10% DNA PAGE in 1X TBE buffer. Lane 1 – 100 bp ladder; Lane 2 – 84 bp control; Lane 3 – 72+3 bp control; Lane 4 – 147 bp (after 5 hrs of ligation reaction). There was no apparent contamination from the 9+3 bp DNA fragment, as re-formation of the 84 bp fragment did not occur with ligase treatment.

3.1.10. Purification of 147 bp DNA

The ligation product was subjected to another round of Mono-Q anion exchange purification. A sodium chloride concentration gradient from 0.3 M to 1 M was used in the process (Fig. 14). During the purification process, three peaks were seen. The first peak was rATP, which eluted immediately after injection of sample, followed by 72 bp (0.65 M) and the last peak was 147bp (0.78 M). The fractions were collected and analyzed on a 10% DNA PAGE in 1X TBE (Fig. 15). The fraction pool containing the 147 bp fragment was then ethanol precipitated and dissolved in TE (10/0.1).

Materials and Methods

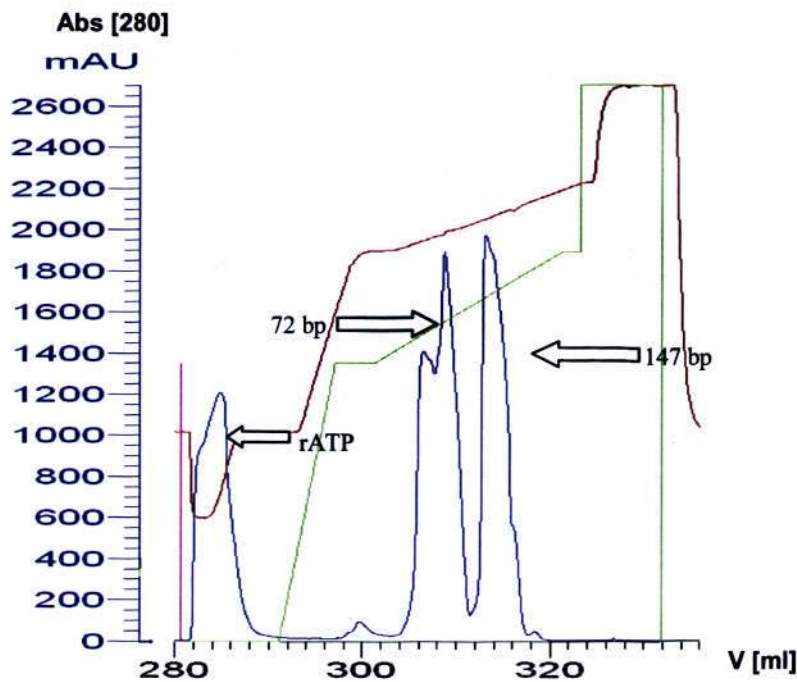
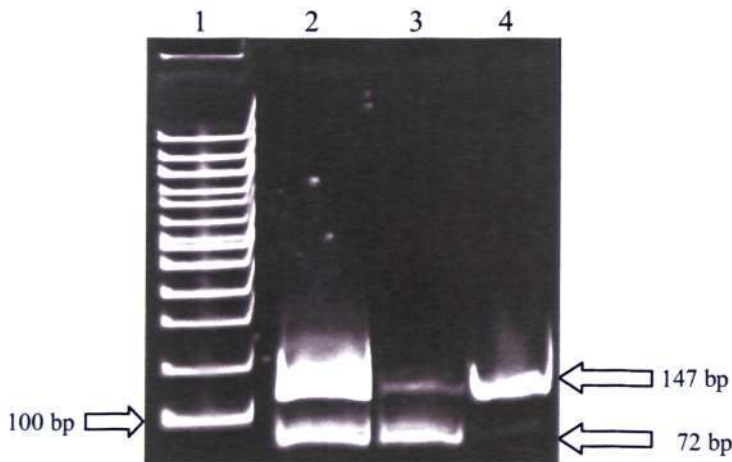


Figure 14. FPLC profile of 147 bp purification. A Mono-Q anion exchange column was used to purify the 147 bp DNA after ligation. 10 mg DNA was injected and passed through the column with a NaCl concentration gradient (green line) from 0.3 M to 1 M. It increased linearly from 0.3 M – 0.45 M and from 0.45 M – 0.8 M with a slight delay in between. The plot shows the eluting profile at 280 nm wavelength (blue line). The first peak which eluted immediately after injection was rATP, the second contained 72+3 bp fragment, eluting at about 0.65 M NaCl. Finally, the third peak contained the 147 bp construct, which eluted at about 0.78 M NaCl. A flow rate of 1 ml/min was maintained.



Materials and Methods

Figure 15. DNA PAGE of 147 bp purification. The purity of the fractionated samples obtained from FPLC was evaluated by 10% DNA PAGE in 1X TBE Buffer. Lane 1 – 100 bp ladder; Lane 2 – FPLC load (147 bp and 72+3 bp mix); Lane 3 – Peak corresponding to 72+3 bp; Lane 4 – Peak corresponding to 147 bp. A pure 147 bp DNA sample was obtained, which was used for NCP preparation.

3.2. Preparation of histones

The four core histone proteins from *Xenopus laevis* were expressed individually in *E. coli* BL21 (DE3) pLysS cells (Promega, Madison, WI, USA) using pET 3a/3d expression vectors. Furthermore, these proteins were purified under denaturing conditions using size-exclusion chromatography, followed by cation-exchange chromatography (whenever needed). All the four histones were mixed in equimolar ratio and refolded to obtain histone octamer (Luger *et al.* 1997b; Dyer *et al.* 2004; Thomas and Butler 1977). The refolded HO was then purified to homogeneity using size-exclusion chromatography.

The amino acid sequences for the four *X. laevis* histones are given below:

H2A (MW – 13.96 KDa)

SGRGKQGGKTRAKAKTRSSRAGLQFPVGRVHRLLRKGNYAERVGAGAPVYLA
AVLEYLTAEILELAGNAARDNKKTRIIPRLQLAVRNDEELNKLGRVTIAQGGV
LPNIQSVLLPKKTESSKSKSK

H2B (MW – 13.77 KDa)

AKSAPAPKKGSKKAVTKTQKKDGKKRRKTRKESYAIYVYKVLKQVHPDTGISS
KAMSIMNSFVNDVFERIAGEASRLAHYNKRSTITSREIQTAVRLLLPGELAKHAV
SEGTKAVTKYTSK

H3 (MW – 15.27 KDa)

ARTKQTARKSTGGKAPRKQLATKAARKSAPATGGVKKPHRYRPGTVALREIRR
YQKSTELLIRKLFPQRLVREIAQDFKTDLRQSSAVMALQEASEAYLVALFEDTN
LCAIHAKRVTIMPKDIQLARRIRGERA

H4 (MW – 11.23 KDa)

SGRGKGGKGLGKGGAKRHRKVLRDNIQGITKPAIRRLARRGGVKRISGLIYEETR
GVLKVFLNVIRDAVITYTEHAKRKTVTAMDVVYALKRQGRTLYGFGG

Materials and Methods

3.2.1. Transformation

One hundred ng plasmid vector (pET-3a or pET-3d encoding individual histone protein) was added to 50 μ l BL21 (DE3) pLysS competent cells. The remaining steps were as in the transformation protocol in section 3.1.1 (for 147 bp DNA preparation) except for the additional antibiotic chloramphenicol (25 μ g/ml).

3.2.2. Protein expression

Five colonies from the transformation plate were inoculated into five individual culture tubes with 4 ml medium, transferred after 3-4 hrs to 100 ml medium and finally inoculated into fifteen 2-liter flasks with 500 ml medium. The protocol was as in 3.1.2. (147 DNA preparation), except for the fact that the medium used here was 2X TYE additionally supplemented with chloramphenicol (25 μ g/ml). The culture in the 15 flasks was allowed to grow until the optical density at 600 nm (OD_{600}) approached 0.5, and then IPTG was added at a concentration of 0.4 mM. After induction, the culture was incubated for about 3 hrs at 37 °C to obtain the maximal expression level of the histone proteins. The protein expression was analyzed by 18% SDS PAGE (Fig. 16). The same procedure was followed for all the 4 histones; H2A, H2B, H3 and H4. However, only the expression profile of H3 is shown here.

3.2.3. Inclusion body preparation

After harvesting the cells at 7,000 rpm for 7 min, the cell pellet was suspended in 50 ml wash buffer, flash-frozen in liquid nitrogen and stored at -20 °C. The frozen cells were thawed in a water bath at 37 °C followed by sonication to lyse the cells. The cell debris was centrifuged down and the pellet washed twice with wash buffer containing Triton X-100. Later, the cell pellet was washed with wash buffer without Triton X-100. The final centrifugation yielded the crude histone inclusion body in pellet form.

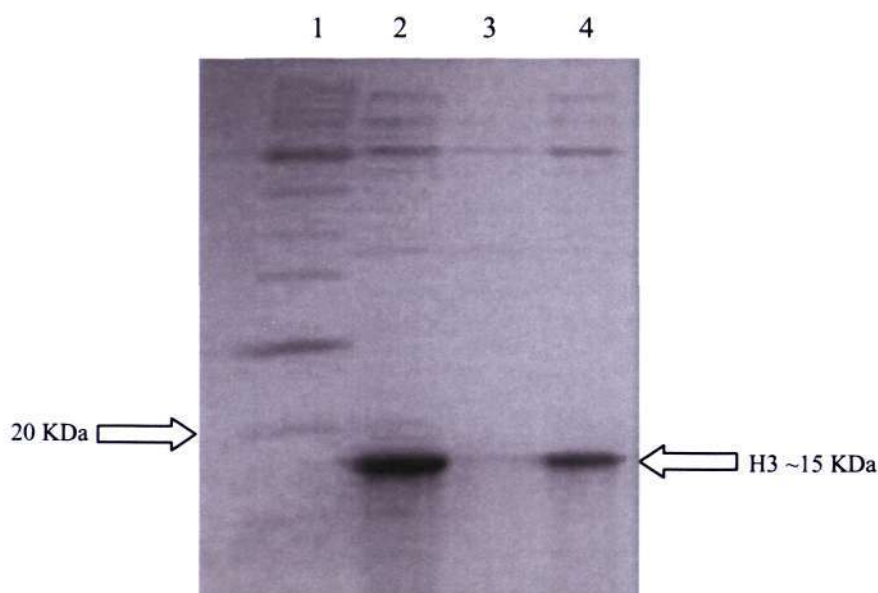
Materials and Methods

Figure 16. SDS PAGE of crude histone (H3) after expression. Expression of the protein was assessed by 18% SDS PAGE. Lane 1 – Protein marker; Lane 2 – Cell pellet after sonication, showing H3; Lane 3 – Pellet wash; Lane 4 – Cell pellet, after wash with Triton –X.

3.2.4. Purification of crude histones

Approximately 6 grams of the individual crude histone proteins was denatured in 40 ml of S-200 unfolding buffer after treating with 1 ml of DMSO. The suspension was homogenized for 1 hour and insoluble debris was removed by centrifugation, which was performed twice and the final supernatant was subjected to size-exclusion chromatography on a Sephacryl S-200 26/60 size-exclusion column (GE Healthcare, Uppsala, Sweden) connected to an AKTA FPLC system (Fig. 17). The fractionated samples were analyzed on 18% SDS PAGE to check the purity of the histones (Fig. 18). To improve the purity, when needed, it was subjected to another round of purification using Resource-S cation-exchange chromatography (GE Healthcare, Uppsala, Sweden). Purified histone proteins in denaturing buffer were dialyzed against water containing 5 mM 2-mercaptoethanol at 4 °C. The histone proteins in water were then aliquoted, lyophilized and stored at -80 °C. The purification profile of H2A is shown in Figures 17 and 18. Figure 19 illustrates all the four histones in their final purity state evaluated by 18% SDS PAGE.

Materials and Methods

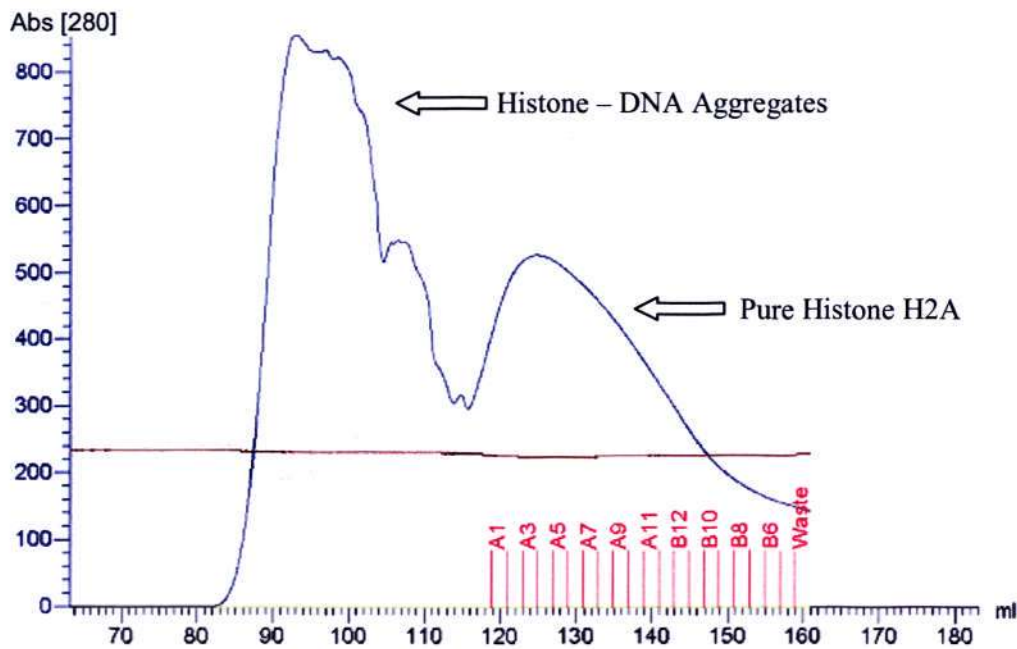


Figure 17. FPLC Profile of H2A purification. H2A protein under denaturing condition was purified using a Sephacryl S-200 26/60 size-exclusion column (GE Healthcare, Uppsala, Sweden). The protein started to elute at about 120ml. The flow rate was maintained at 1 ml/min.

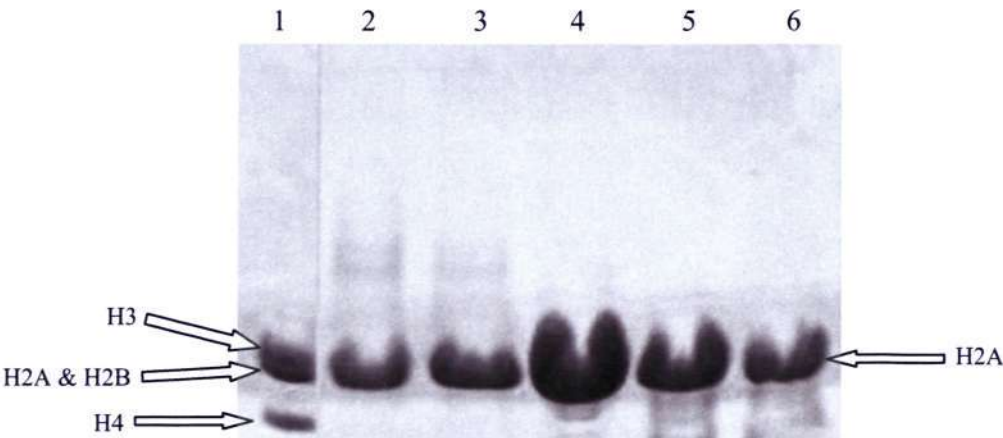


Figure 18. SDS PAGE of H2A purification. H2A fractions purified by size-exclusion chromatography (shown in Figure 17) were analyzed by 18% SDS PAGE to check the purity of the fractions. Lane 1 – Histone octamer marker; Lane 2 – Fraction A1; Lane 3 – Fraction A2; Lane 4 – Fraction A5; Lane 5 – Fraction A11; Lane 6 – Fraction B11. Fraction A1

Materials and Methods

and A2 showed some high molecular weight contamination, whereas fractions A5 to B1 were relatively pure.

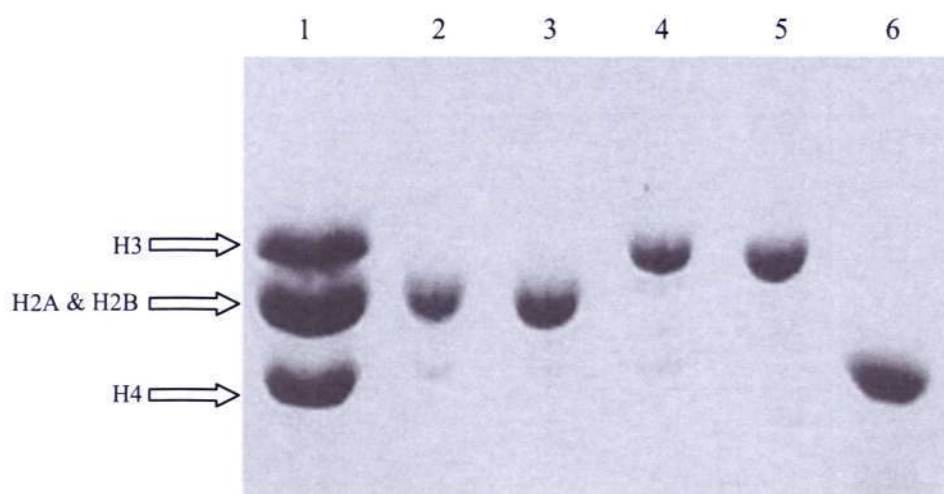


Figure 19. SDS PAGE of pure histones. Individually purified proteins were analyzed by 18% SDS PAGE. Lane 1 – Histone octamer marker; Lane 2 – H2A; Lane 3 – H2B; Lane 4 – Wild type H3; Lane 5 – C110A H3 mutant; Lane 6 – H4. The proteins appeared to be highly pure.

3.2.5. Histone octamer refolding

Purified histone aliquots were dissolved in HO unfolding buffer and allowed to mix in a shaker at 220 rpm for 1 hour. Later, all the histone proteins were mixed in an equimolar stoichiometric ratio ($H2A:H2B:H3:H4 = 4.57 \text{ mg}: 4.51\text{mg}: 5 \text{ mg}: 3.68 \text{ mg}$). This denatured mix was dialyzed against HO refolding buffer at room temperature. After two changes to fresh dialysis buffer and with an additional over-night dialysis, the obtained HO was concentrated using a 10 KDa cut-off Amicon concentrator (Millipore, USA) to about 10 mg/ml concentration.

3.2.6. Purification of histone octamer

The concentrated HO was centrifuged twice at a speed of 11,000 g for 10 min at 20 °C, before proceeding with the purification step. The HO was passed through a Sephacryl S-200 26/60 size-exclusion column to remove high molecular aggregates as well as $(H3-H4)_2$ tetramer and H2A-H2B dimer (Fig. 20). The fractions from the S-200

Materials and Methods

column were analyzed on 18% SDS PAGE (Fig. 21) to ensure the purity of the HO. Finally, the octamer was concentrated, mixed with an equal volume of glycerol and stored at -20 °C.

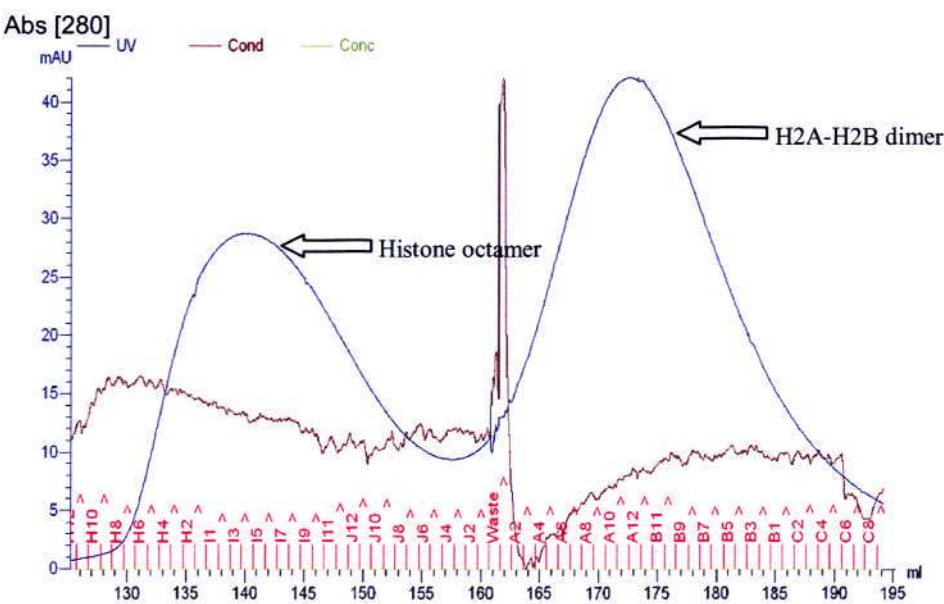
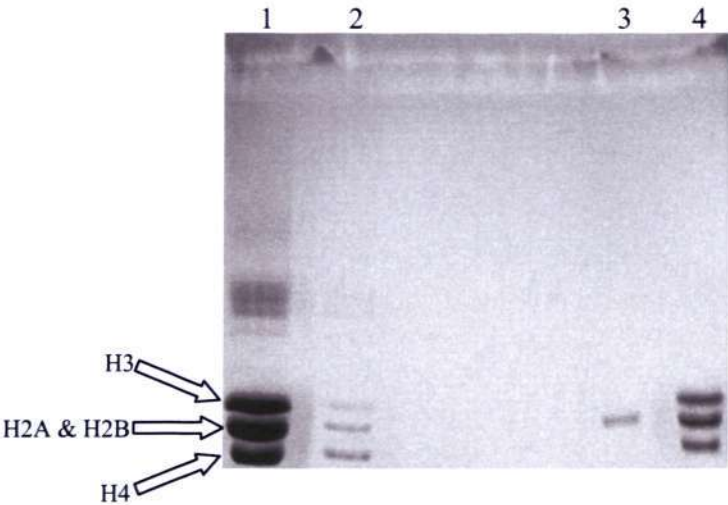


Figure 20. FPLC profile of histone octamer purification. Histone octamer sample was purified using a Sephacryl S-200 26/60 size-exclusion column in a refolding buffer which contained 2 M NaCl and 5 mM 2-mercaptoethanol. Pure histone octamer eluted at about 130 ml and the H2A-H2B dimer at about 160 ml. The flow rate throughout the process was maintained at 1 ml/min.



Materials and Methods

Figure 21. SDS PAGE of purified histone octamer. Purified Histone octamer from size-exclusion chromatography was analyzed by 18% SDS PAGE. Lane 1 – Histone octamer marker (8 μ g); Lane 2 – Histone octamer (2 μ g); Lane 3 – Peak corresponding to H2A-H2B dimer (2 μ g); Lane 4 – Peak corresponding to purified histone octamer (4 μ g). Some degree of dimer formation of the histone octamer marker could be seen on the gel and it is probably due to prolonged storage. The purified histone octamer was of good quality and used to make NCP by reconstitution with 147 bp DNA.

3.3. NCP reconstitution

Purified HO and 147 bp DNA were mixed at a ratio of 0.9:1.0 under high salt conditions. The salt concentration was gradually reduced *via* serial dialysis against lower salt concentration buffers at room temperature. During dialysis, as salt gets removed, HO and 147 bp DNA tend to associate together and form nucleosome core particle (NCP).

- The reconstitution mix was prepared by adding the following ingredients in the given order - water, 2 M KCl, 10 mM DTT, HO and 147 bp DNA.
- Dialysis against TCS-0.85 buffer for 2.5 hrs
- Dialysis against TCS-0.65 buffer for 2.5 hrs
- Dialysis against TCS-0.45 buffer for 2.5 hrs
- Final dialysis against TCS-0 buffer over night

Electrophoretic Mobility Shift Assay (EMSA) was performed using 5% DNA PAGE in 0.25XTBE buffer to check the quality of the reconstituted NCP samples. Reconstitution of longer DNA fragments is known to form a heterogeneous population of NCP with respect to the position of the DNA on the HO (Luger 2003), resulting in a uniquely positioned (centered) and off-centered NCP on an EMSA gel (Fig. 22). The majority of the reconstitution product was centered. However, when a particular batch of reconstituted sample had a significant fraction of the off-centered species, then those samples were incubated for 2 hrs at 37 °C to induce repositioning to the centered state (Luger *et al.* 1999).

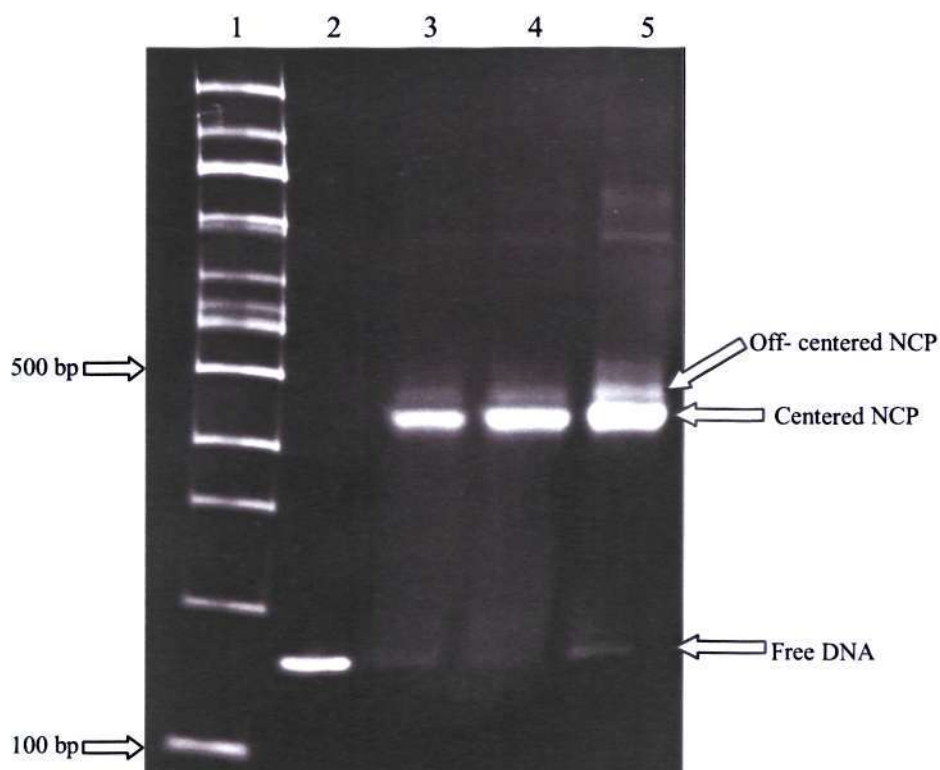
Materials and Methods

Figure 22. EMSA of reconstituted NCP. Reconstituted NCP was analyzed by 5% DNA PAGE in 0.25XTBE buffer to assess homogeneity. Lane 1 – 100 bp DNA ladder; Lane 2 – 147 bp control; Lane 3 – NCP (1 µg); Lane 4 – NCP (2 µg); Lane 5 – NCP (4 µg).

Due to slight discrepancies in the concentration estimation of HO, frequently an insufficient or excess amount of HO than the actual requirement was added to the DNA. This results in either the DNA remaining in a free form along with NCP or gives formation of a certain amount of a dimeric complex having a 1:2 stoichiometry of DNA:HO, together with NCP. In these cases, it was essential to purify the NCP from excess free DNA or the dimeric complex, which was accomplished by subjecting samples to a round of Mono-Q anion exchange purification (Buffer A – 50 mM NaCl and Buffer B – 1000 mM NaCl) (Fig. 23) or applying the Superdex S-200 (GE Healthcare, Uppsala, Sweden) size exclusion method. We successfully purified NCP using either method; although generally anion exchange worked better, wherein NCP eluted out at about 45% of buffer B and free DNA eluted out at about 70% B. Purified sample was evaluated on a 5% DNA-PAGE in 0.25X TBE buffer.

Materials and Methods

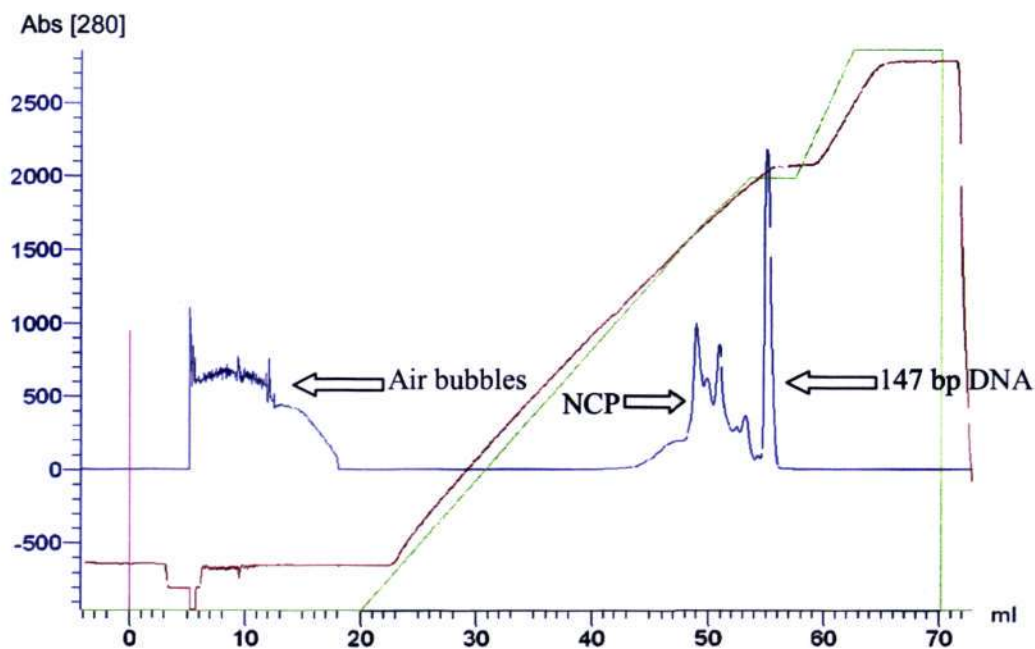
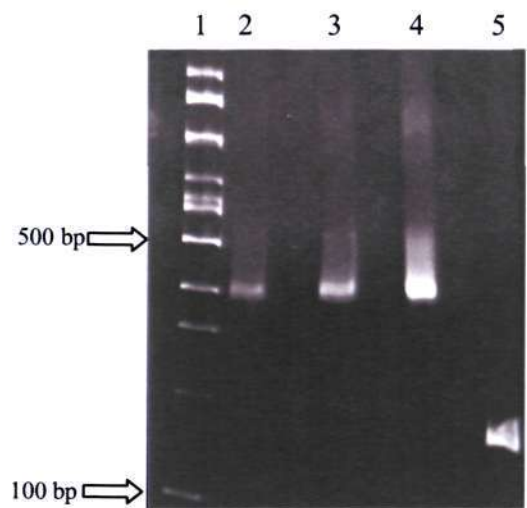


Figure 23. FPLC profile of NCP purification. A Mono-Q anion exchange column was used to purify NCP from free 147 bp DNA or other higher molecular weight materials. A NaCl concentration gradient (green line) of 0.05 M to 1 M was used, which increases linearly from 0.05 M to 0.75 M. About 1ml of NCP at a concentration of 2 mg/ml was injected in to an anion exchange column connected to an AKTA FPLC system. The plot shows the elution profile at 280 nm wavelength (blue line), where NCP elutes at about 0.45 M NaCl, and 147 bp DNA at about 0.75 M NaCl. The flow rate was maintained at 1 ml/min.



Materials and Methods

Figure 24. EMSA of ion-exchange purified NCP. NCP purified from an anion exchange column was subjected to 5% DNA PAGE in 0.25X TBE buffer. Lane 1 – 100 bp DNA ladder; Lane 2 – Purified NCP (1 µg); Lane 3 – Purified NCP (2 µg); Lane 4 – Purified NCP (4 µg); Lane 5 – Peak corresponding to 147 bp DNA. The NCP sample after purification did not show a detectable level of free DNA.

3.4. Preparation of designer DNA

DNA sequences with predicted higher affinity for binding to HO were produced. Approaches, such as consensus sequence analysis, dinucleotide steps analysis and DNA conformational studies were used to design Des 147. This non-palindromic sequence was modified from the common human α -satellite DNA sequence (147 α s; Davey et al., 2002). Three different sequences were prepared; Des-1, Des-2 and Des-3 (Fig. 25). Each Des DNA was cloned as 2 copies of full 147 bp in the pUC57 vector (a version of pUC 19). The constructs were ordered and purchased from EZBiolab (Indiana, USA).

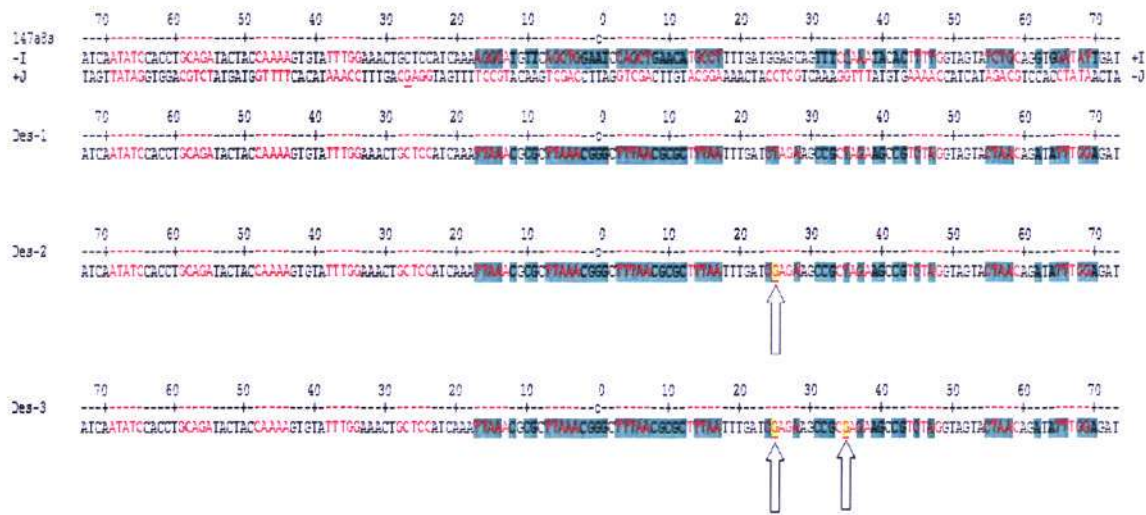


Figure 25. Comparison of 147 α s and the designer sequences. The three designer 147 bp sequences are indicated as Des-1, Des-2 and Des-3. Nucleotides shown in red correspond to regions where the minor groove faces inward towards the histone octamer. The arrows and the regions highlighted in yellow indicate sequence differences of Des-2 and Des-3 with respect to Des-1. Green highlighted regions show sequence differences of Des-1, Des-2 and Des-3 relative to the 147 α s template sequence.

Materials and Methods

3.4.1. Transformation, amplification, isolation and purification of designer DNA

Designer DNA was isolated and purified as described for pUC- α 32s (section 3.1). Two copies of 147 bp designer DNA were cloned in to the MCS (multiple cloning sites) of the vector. Since the designer DNA is cloned in as a full non-palindromic 147 bp fragment, the steps such as *Hinf*I digestion, ligation and FPLC purification were not required. However, the overall yield was low as there were only 2 copies of 147 bp in the vector pUC57 (Fig. 26), compared to 32 half-site repeats of 84 bp for pUC- α 32s.

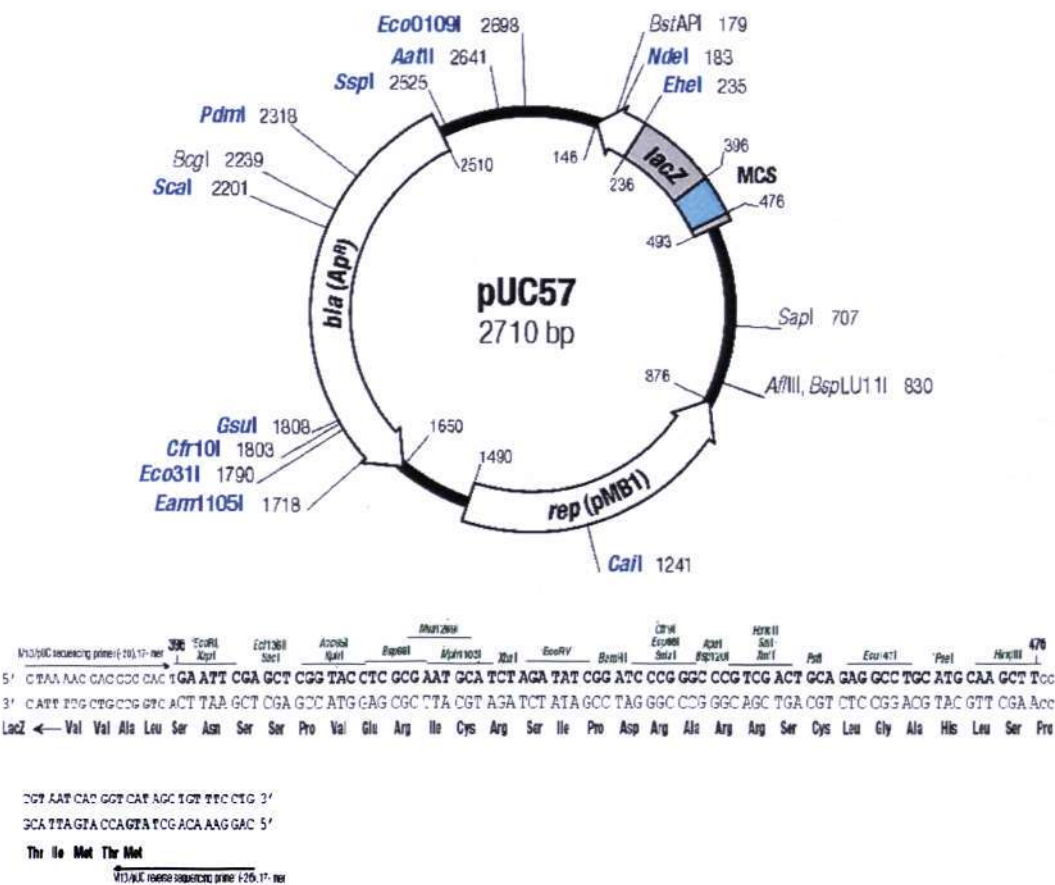


Figure 26. Plasmid vector pUC57 and details of the multiple cloning sites (MCS). Two copies of the respective designer DNA were cloned into the *Eco*RV site of this vector (Ezbiolab, Indiana, USA).

Materials and Methods

3.4.2. *EcoRV* digestion

The purified pUC-57 vector was digested with the restriction enzyme *EcoRV* to release the 147 bp DNA from the vector. The digested sample was evaluated by a 10% DNA PAGE in 1X TBE buffer (Fig. 27). The digestion reaction included 2 mg/ml of plasmid DNA in a buffer containing 50 mM Tris (pH 7.6), 100 mM NaCl, 10 mM MgCl₂ and 1 mM DTT. *EcoRV* enzyme was used at a ratio of 30 units per mg of DNA. The reaction mixture was incubated with continuous shaking for 24 hours at 37 °C.

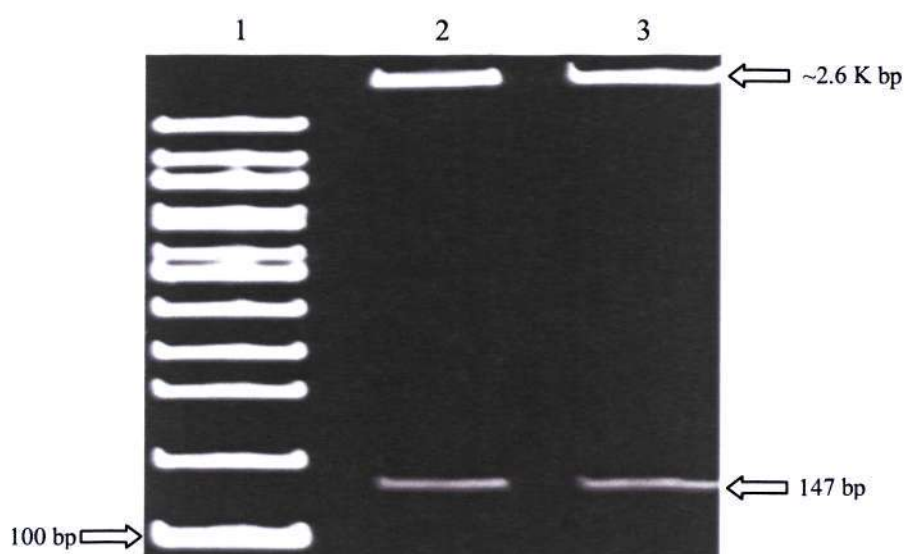


Figure 27. DNA PAGE of *EcoRV* digestion. The extent of digestion was analyzed by 10% DNA PAGE in 1X TBE Buffer. Lane 1 – 100 bp ladder; Lane 2 – *EcoRV* digested sample (250 ng); Lane 3 – *EcoRV* digested sample (400 ng). The digestion appears to be complete.

3.4.3. PEG fractionation

After *EcoRV* digestion, the vector was removed by PEG fractionation. The *EcoRV* reaction mixture containing the vector and insert was fractionated by addition of 9.25% PEG6000 and 0.5 M NaCl. Subsequently, the sample was incubated on ice for 1 hour, followed by centrifugation at 27,000g for 20 min at 4 °C. 147 bp DNA with free phosphate ends was obtained in the supernatant fraction, which was evaluated by 10% DNA PAGE in 1X TBE buffer (Fig. 28). The sample was then ethanol precipitated and resuspended in TE (10/0.1).

*Materials and Methods***3.4.4. Dephosphorylation**

To remove the 5' free phosphate ends of 147 bp DNA, CIAP was used at a ratio of 72 units per mg of DNA. The dephosphorylation reaction included 2 mg/ml of 147 bp DNA in a buffer containing 50 mM Tris (pH 8.0), 10 mM MgCl₂ and 0.1 mM EDTA. The mixture was incubated for 24 hours in a shaker incubator at 37 °C. Dephosphorylated 147 bp was then extracted with a 1:1 phenol-CIA mixture to remove the enzyme and any traces of remaining PEG. DNA fragment was then ethanol precipitated and resuspended in TE (10/0.1). To ensure the complete dephosphorylation of the 147 bp construct, a small ligation test was performed using T4 ligase, which was analyzed by a 10% DNA PAGE in 1X TBE buffer (Fig. 28).

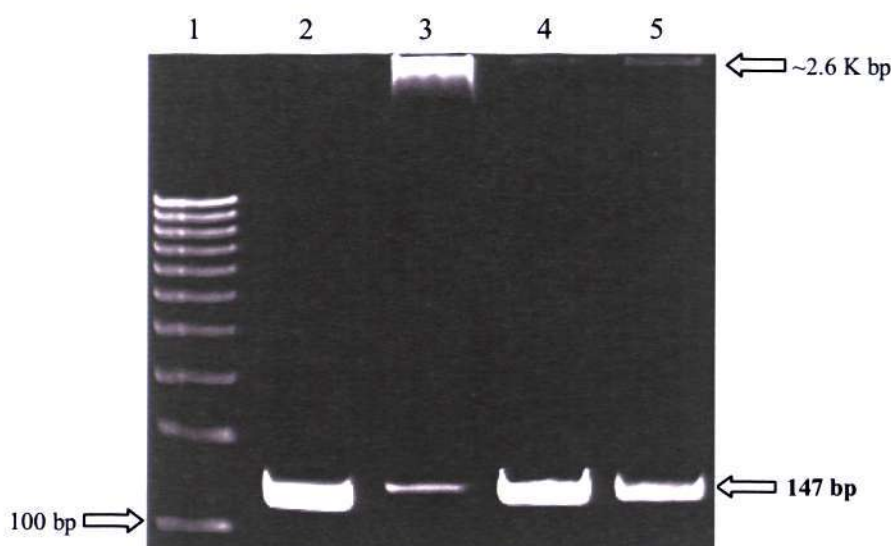


Figure 28. DNA PAGE of PEG fractionation and dephosphorylation. To ensure the separation of the 147 bp fragment from vector by PEG fractionation, the sample was analyzed by 10% DNA PAGE in 1X TBE buffer. Lane 1 – 100 bp ladder; Lane 2 – 147 bp control; Lane 3 – Undephosphorylated 147 bp DNA after ligation test; Lane 4 – PEG fractionated 147 bp DNA supernatant; Lane 5 – Dephosphorylated 147 bp DNA after ligation test. PEG fractionation was efficient in separating 147 bp DNA from the vector DNA, and the ligation test on the dephosphorylated 147 bp DNA showed that the dephosphorylation step was complete.

Materials and Methods

3.5. Crystallization of NCP

Reconstituted NCP was concentrated to > 8 mg/ml and stored in a buffer which contained 20 mM potassium cacodylate (pH 6.0) and 1 mM EDTA. Prior to crystallization of NCP, the sample concentration was adjusted to exactly 8 mg/ml by diluting with the same buffer, and later it was mixed with an equal volume of 2X crystallization buffer (170 mM MnCl_2 , 120 mM KCl, and 40 mM K cacodylate) to bring the final concentration of NCP to 4 mg/ml. The final 1X solution was initially a bit cloudy. The cloudiness disappeared in about 2 hours after incubation at room temperature. The sample was spun down at 14,500 rpm for 10 minutes at 4 °C to remove any aggregates, and it was then applied to crystallization.

Crystallization drops size varied from 4-10 μl . For screening, 4 μl drops were used, whereas to obtain bigger, diffraction quality crystals, 10 μl drops were set up. The reservoir solution in the hanging drop or sitting drop setup had 1 ml of 0.5X crystallization buffer (42.5 mM MnCl_2 , 30 mM KCl, 10 mM K cacodylate).

The most common vapour diffusion crystallizations make use of the “salting out” phenomenon, where the reservoir buffer has a precipitant concentration of 1X and that in sample would be 0.5X. But in our studies we used the “salting in” approach, which is suitable for NCP crystallization. The plates containing crystallizations were maintained in an 18 °C incubator, and the drops allowed to equilibrate against the reservoir. Crystals started growing from day three to seven, depending on the size of the drop.



Figure 29. Crystal of NCP grown under standard MnCl_2 condition.
Purified NCP can be crystallized in divalent metal-containing buffers.

In general, NCP crystals grew to full size ($\sim 150 \times 200 \times 500$ μm) in about 3 weeks (Fig. 29). Such crystals were ready for diffraction studies. These NCP crystals were

Materials and Methods

exchanged into a buffer containing 37 mM MnCl_2 , 40 mM KCl, 20 mM potassium cacodylate (pH 6.0), 24% 2-methyl-2, 4-pentanediol (MPD) and 2% trehalose by gradually increasing the concentration of MPD to 24% in steps of 4% MPD increments and incorporation of 2% trehalose in the final step. Harvested NCP crystals were maintained in this final buffer for 3 hours to overnight for stabilization purposes.

3.6. Data collection and processing

Initially, the in-house X-ray facility at NTU School of Biological Sciences was used for testing the diffraction quality of the various crystals, as well as for preliminary data collection. The radiation for these experiments was $\text{CuK}\alpha$, from a Rigaku FR generator operating at 40 kV and 20 mA. Either a MAR or a Rigaku RAXIS IV image plate were utilized.

Final X-Ray diffraction images were collected at beamlines PXI and PXII of the Swiss Light Source (SLS, Villigen, Switzerland) synchrotron using a MAR CCD or the Pilatus detector. Fluorescence spectra were taken to determine the absorption edge of the element of interest. Data were collected after tuning the wavelength to the respective absorption edge of the element, such as Ni and Co. The oscillation scan was 0.5 degree, and the exposure time was ~1.0 second per image depending upon the crystal characteristics. Crystals ranging in size from 300 to 600 μm in the longest dimension were mounted on a cryo-loop at -170°C , and data was collected. For crystals which showed diffraction to a good resolution, full data-sets of 360 frames were collected.

The collected datasets were processed using the software program XDS or MOSFLM and routines from the Collaborative Computational Project 4 package (CCP4-1994). The initial steps of data processing, indexing and integration, were performed by either using XDS (Kabsch 1993) or MOSFLM (Leslie 1992), and the remaining steps including scaling, merging, phasing and generation of anomalous maps, were carried out using the CCP4 package. The electron density maps were visualized using Coot (Emsley and Cowtan 2004). Manual refinement was carried out on COOT, and automated refinement performed with the Refmac program of CCP4.

Crystal structures were solved using the native NCP147 model as the reference for molecular replacement. This was followed by rigid body refinement and restrained

Materials and Methods

refinement. Anomalous difference electron density maps were calculated with phases from an NCP model lacking metal ions and the map was used to determine the locations of heavy metal ions.

3.7. Atomic absorption spectroscopy

Atomic absorption spectroscopy (AAS) was performed in order to ensure the complete removal of manganese ions from the crystallization buffer as well as from the NCP crystals. The technique makes use of absorption spectrometry to assess the concentration of a heavy metal in the sample, based on the Beer-Lambert absorption-concentration principle. Metals in their elemental form absorb UV light when they are excited by heat, giving rise to a diagnostic absorption spectrum. The AAS instrument detects a metal of interest by focusing a beam of ultraviolet light at a specific wavelength at the vaporized sample.

For detecting the presence of a specific heavy metal, a calibration curve is first prepared by taking readings of the metal over a range of known concentrations. The AAS instrument, connected to a PC, automatically plots the data and generates a standard curve. This standard curve enables calculation of accurate metal concentrations in the experimental samples.

Various concentrations (0, 50, 100, 200, and 400 nM) of manganese chloride were prepared for generating the standard curve (Fig 30), which was used to establish that manganese had been eliminated from the heavy metal substitutions of NCP crystals. In Table 1, samples 1 and 2 were crystal harvesting buffer without manganese containing the respective heavy metals (5 mM CoCl_2 or NiCl_2 , 40 mM KCl, 20 mM K-cacodylate, 24% MPD and 2% Trehalose). Samples 3 and 4 were crystal harvesting buffer with the respective heavy metals (5 mM CoCl_2 or NiCl_2 , 40 mM KCl, 20 mM K-cacodylate, 24% MPD and 2% Trehalose) after crystal equilibration. Samples 5 and 6 were buffer exchanged crystals (with the respective heavy metals) washed in 100 μl of water and resuspended in 20 μl of water. Analysis of the samples showed that Mn^{2+} were removed from the buffers as well as from the crystals.

Materials and Methods

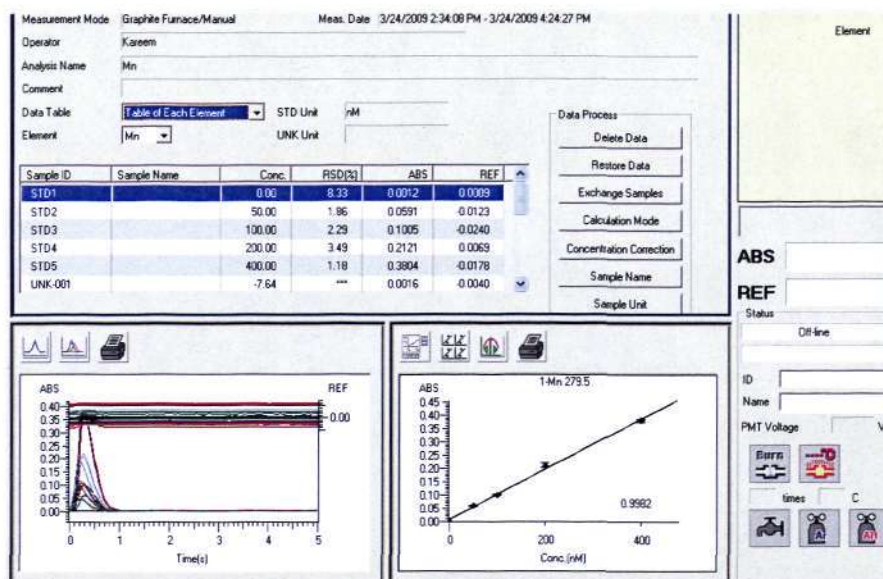


Figure 30. Generation of a standard concentration profile for Mn^{2+} by atomic absorption spectroscopy

Table 1. Atomic absorption spectroscopic readings of manganese in nickel and cobalt-containing buffers and NCP crystals

Serial no	Samples	Concentration	Absorbance	Remark
1	Co-Buffer	-7.64	0.0016	Conc based on STD Curve
2	Ni-Buffer	-7.96	0.0013	Conc based on STD Curve
3	Harvest - Co-Buffer	-6.85	0.0023	Conc based on STD Curve
4	Harvest - Ni-Buffer	-7.11	0.0021	Conc based on STD Curve
5	Crystal - Cobalt	-6.74	0.0024	Conc based on STD Curve
6	Crystal - Nickel	-6.27	0.0029	Conc based on STD Curve

Sample 1 & 2 - Cobalt and Nickel crystallization buffer before harvesting the crystals.

Sample 3 & 4 - Cobalt and Nickel crystallization buffer after harvesting the crystals.

Sample 5 & 6 - Cobalt and Nickel-exchanged crystals dissolved in water.

Materials and Methods

3.8 Buffer compositions

Crude histone denaturing buffer

7 M Urea (de-ionized)
20 mM Na-Acetate (pH-5.2)
1 M NaCl
1 mM EDTA
5 mM β -mercaptoethanol (add freshly)

S200 unfolding buffer

7 M Guanidinium HCl
20 mM Na-Acetate (pH-5.2)
10 mM DTT (add freshly)

Histone octamer refolding buffer

2 M NaCl
10 mM Tris-HCl (pH-7.5)
1 mM Na-EDTA
5 mM beta-mercaptoethanol (BME) (add freshly)

TYE agar medium – 1 Liter

Bacto Tryptone - 10 gram
Yeast Extract - 5 gram
Sodium chloride - 8 gram
Agar - 15 gram

TYE broth medium – 1 Liter

Bacto Tryptone - 16 gram
Yeast Extract - 10 gram
Sodium chloride - 5 gram
Glucose - 1%

Terrific broth (TB) – 1Liter

Bacto Tryptone - 12 gram
Yeast Extract - 24 gram
 KH_2PO_4 (1M) - 17 ml
 K_2HPO_4 (1M) - 72 ml
Glycerol (50% v/v) - 8 ml

Alkaline lysis buffers

Buffer I \rightarrow 50 mM Glucose, 10 mM EDTA and 25 mM Tris-HCl (pH-8.0)
Buffer II \rightarrow 200 mM NaOH and 1% (w/v) SDS
Buffer III \rightarrow 4 M K-Acetate and 2 M Glacial acetic acid

RESULTS

4. CRYSTALLOGRAPHIC RESULTS

In the crystallographic characterization of heavy metal binding to the NCP, we selected a few candidates which are known to strongly bind DNA. These soft metals can cause DNA damage via Fenton's reaction, where the metals generate hydroxyl radicals, which cleave the DNA. Therefore, fenton's reaction plays a role in ROS-mediated cell death. We screened a repertoire of divalent cations, including nontoxic ones, and the choice of metals was narrowed down to nickel and cobalt, which did not cause extensive damage to the NCP crystals upon substitution.

4.1. Crystallization of NCP using several divalent metals

4.1.1. Magnesium form of NCP

Crystals were originally grown and harvested as mentioned in **Materials and Methods** section 3.5. These crystals were gradually buffer-exchanged by reducing the concentration of MnCl_2 (starting with 37mM and reducing in instalments of 4 mM *per* step) while at the same time introducing MgCl_2 (4 mM *per* increment) and further increasing the concentration of MgCl_2 to 37 mM.

Crystals prepared in this manner diffracted up to 3.6 Å resolution using the in-house facility. A complete dataset was collected and processed. The differences and anomalous maps obtained from the data did not show any peak at the positions of Mn^{2+} as known from the previous native structure. Replacement of Mn^{2+} by Mg^{2+} takes place and induces some disordering of the crystal. However, at this resolution it is not possible to evaluate the influence of Mg^{2+} on NCP DNA. Accurate modeling of the low electron density of Mg^{2+} in the NCP would likely require a resolution of ~2 Å.

In order to comprehend the role of Mg^{2+} on NCP in its native state, we did a grid screening and have successfully grown NCP crystals in conditions with Mg^{2+} , avoiding Mn^{2+} completely (Fig 31). The morphology of these crystals looks different (thin and long) compared to crystals grown with Mn^{2+} . Diffraction studies were carried out, and these crystals diffracted only up to ~8 Å. We tried to grow bigger crystals under similar conditions, and using the additive screening kit (Hampton Research), but none of the crystals gave better resolution as compared to the MgCl_2 buffer-exchanged crystals.

Results

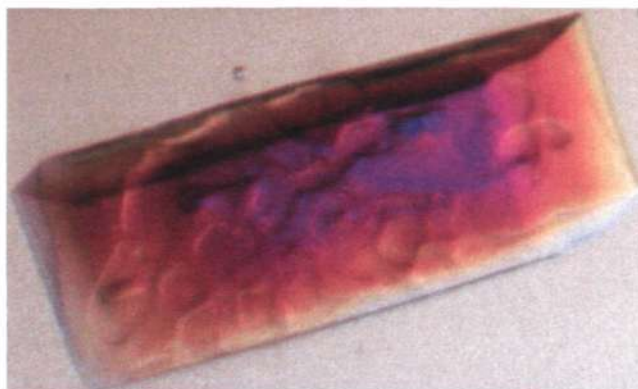


Figure 31. Crystal of NCP grown in Mg^{2+} containing buffer.

4.1.2. Calcium form of NCP

The same strategy of buffer exchange used for Mg^{2+} was applied to introduce Ca^{2+} into NCP crystals. Such crystals diffracted very poorly (maximum resolution ~ 6.5 Å) at the in-house facility. We subsequently tried to crystallize NCP *de novo* by substituting $MnCl_2$ in the standard NCP crystallization condition with $CaCl_2$ and conducting grid screening. We obtained crystals under a few conditions (Fig 32), and these crystals looked large and chunky, with some irregularities in surface, compared to crystals grown with Mn^{2+} . These crystals gave diffraction up to ~ 5.8 Å. Further, we tried to optimize these conditions using additive screening (Hampton research) but none of the conditions gave better diffracting crystals, and hence we decided that the buffer-exchanged crystals with magnesium chloride could be an option to study heavy metal-NCP interactions.

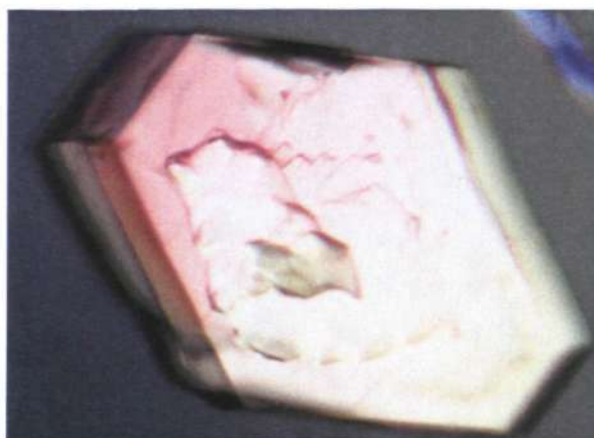


Figure 32. Crystal of NCP grown in Ca^{2+} containing buffer.

Results

4.1.3. Mercury soaked crystal data in Mg^{2+} background

NCP crystals were buffer-exchanged with $MgCl_2$, to give a final concentration of 35 mM Mg^{2+} . To the crystals prepared this way, 2 mM $HgCl_2$ was added and allowed to equilibrate for 2 days. The crystals gave very anisotropic diffraction in-house to 4.25 Å resolution. A data set was collected and processed to obtain an anomalous map. We could not see any anomalous difference peaks corresponding to Mn^{2+} positions as these would have been replaced by Mg^{2+} . There was also no indication of the presence of Hg^{2+} on the DNA. This could be due to the anomalous signal being too weakened by DNA disordering. In contrast, we could see a very strong anomalous peak (up to 12.5 sigma), corresponding to Hg^{2+} associated with the cysteine residues of the histone protein H3 (Fig 33).

From the previous studies on naked DNA, it is known that Hg^{2+} binds to nucleobases very strongly, and there was no evidence found for Hg^{2+} -phosphate interactions (Bloomfield *et al.* 2000). In addition to this, Hg^{2+} ions bind specifically and tightly to A/T-rich DNA, because of its strong affinity for the N3 of thymine (Izatt *et al.* 1971). Recent studies showed that Hg^{2+} ions bind especially to the regions with T-T mismatches (Tanaka *et al.* 2006; Miyake *et al.* 2006). The 147 bp DNA in NCP does not have any such T-T mismatch regions and probably that is why we do not see any Hg^{2+} interaction with DNA. Due to the above reasons and poor resolution we stopped further investigations with Hg^{2+} .

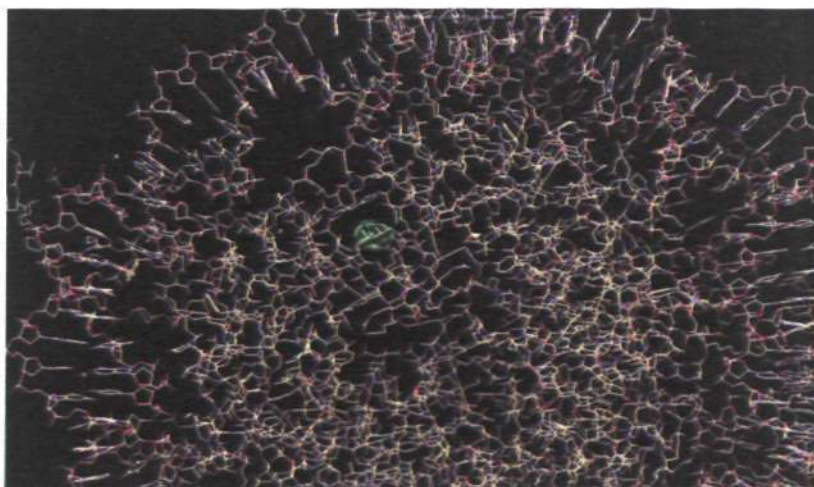


Figure 33. *Anomalous map contoured at 9σ shows the signal of Hg^{2+} binding to cysteine residues C110 of H3.*

Results

4.1.4. Cadmium soaked crystals

Crystals were buffer exchanged as mentioned in Mg^{2+} soaked crystal procedure to 35 mM MgCl_2 and exchanged to 2 mM CdCl_2 . But these crystals diffracted very poorly. In order to circumvent this problem, we decided not to change the crystals to MgCl_2 and instead slowly bring down the concentration of MnCl_2 (6 mM lower concentration of Manganese *per* step) until the diffraction quality weakens, as checked in each step. Until 4 mM, the diffraction quality did not deteriorate much. To this condition, we added 1 mM CdCl_2 and allowed to equilibrate for different time intervals. Only the crystal soaked for less than 1 hour gave good diffraction data.

These crystals diffracted in house to 3.6 Å and a complete dataset was collected. Data were processed to obtain an anomalous map. In the anomalous map, we observed a strong anomalous peak of 11.25 sigma on the cysteine residue of H3. This clearly indicates the presence of Cd^{2+} .

With different crystal preparations, observation of the cysteine site where Cd^{2+} binds was not well reproducible. Apparently, with short soaking times, although diffraction is strong, Cd^{2+} exchange is incomplete. Also, with full equilibration of Cd^{2+} exchange (> 3h to days) diffraction is prohibitively poor. It is clear that without full equilibration we cannot accurately investigate the influence of Cd^{2+} on NCP.

Buffer exchange experiments with Cu^{2+} , Zn^{2+} and Pb^{2+} gave very similar poor diffraction results as for the other heavy metals described above. On the other hand, we were able to conduct full replacement of Mn^{2+} with Ni^{2+} and Co^{2+} with only a modest loss of diffraction quality. In general, it appears that the similarity in coordination geometry and limited softness of Ni^{2+} and Co^{2+} allows them to serve a similar function in maintaining a preformed crystal lattice as Mn^{2+} (discussed in detail in Discussion section). Hence, we investigated these metals in detail and their influence on NCP structure.

4.2. Crystallographic characterization of Ni^{2+} binding to NCP

Initially, we tried to crystallize NCP using various concentrations of nickel chloride via grid screens with replacement of manganese chloride. This condition did not yield any crystals even several weeks after setting up crystallizations. Therefore, the next approach was to either co-crystallize, whereby we added nickel chloride into the

Results

manganese chloride-based condition or to exchange metal in the NCP crystals pre-grown in Mn-buffers.

First, we started with co-crystallizations by adding nickel chloride to the original MnCl_2 condition (85 mM MnCl_2 , 60 mM KCl and 20 mM K-cacodylate pH-6.0). Different concentrations of NiCl_2 , varying in the range of 1 to 20 mM (increment in steps of 2.5 mM) were used. Almost all the conditions gave crystals, showing the importance of MnCl_2 in the crystallization process, but the crystals which were grown in the presence of more than 5 mM nickel chloride were small, thin and had a different shape in comparison with the crystal grown in the standard condition. These crystals were harvested in the same way as mentioned in the **Materials and Methods** section 3.5, in the presence of nickel chloride at the respective concentration.

Crystals grown in simultaneous presence of manganese chloride and nickel chloride were diffracting poorly as compared to the crystals grown in the original condition. Moreover, the resolution limit was roughly proportional to increasing concentration of nickel chloride. However, crystals grown in the presence of 5 mM or less nickel chloride were similar in size and shape as compared to crystals grown in the standard condition, also gave better diffraction.

The presence of manganese chloride in the crystallization buffer as well as in the harvesting buffer posed a major issue. Differentiating Mn from Ni ions based on anomalous difference maps is difficult as both metals have similar X-ray absorption properties. This has led to an alternate strategy. The crystals were initially harvested in the same way as mentioned in **Materials and Methods** section 3.5. Once the crystals were equilibrated in 24% MPD-containing harvest buffer, substitute buffer containing 37 mM NiCl_2 in place of MnCl_2 was used to wash out manganese. This involved reducing the buffer volume in which the crystals sit to 200 μl , followed by addition of 1 ml of the Ni buffer and allowing equilibration over ~10 minutes by light mixing. Subsequently, buffer was removed down to 200 μl and the process repeated 10 times in total. This yields a theoretical dilution of Mn^{2+} of 60.5 million-fold. Atomic Absorption Spectroscopy (AAS) was used in order to ensure the complete removal of manganese from our samples, and we confirmed that the contamination contribution by manganese is less than 10 nM (the detection limit of our AAS instrument).

Results

The Ni^{2+} -substituted crystals, prepared in the above manner, were used to obtain a diffraction data set of 2.65 Å resolution at the SLS synchrotron. Wavelength was tuned based on the Ni fluorescence spectral maximum, and data was collected accordingly at the experimental Ni absorption edge (1.498 Å). The overall structure of NCP147 with nickel ions is shown in Figure 34. The detailed statistics of the crystal and final refinement of the structure are provided in Table 2.

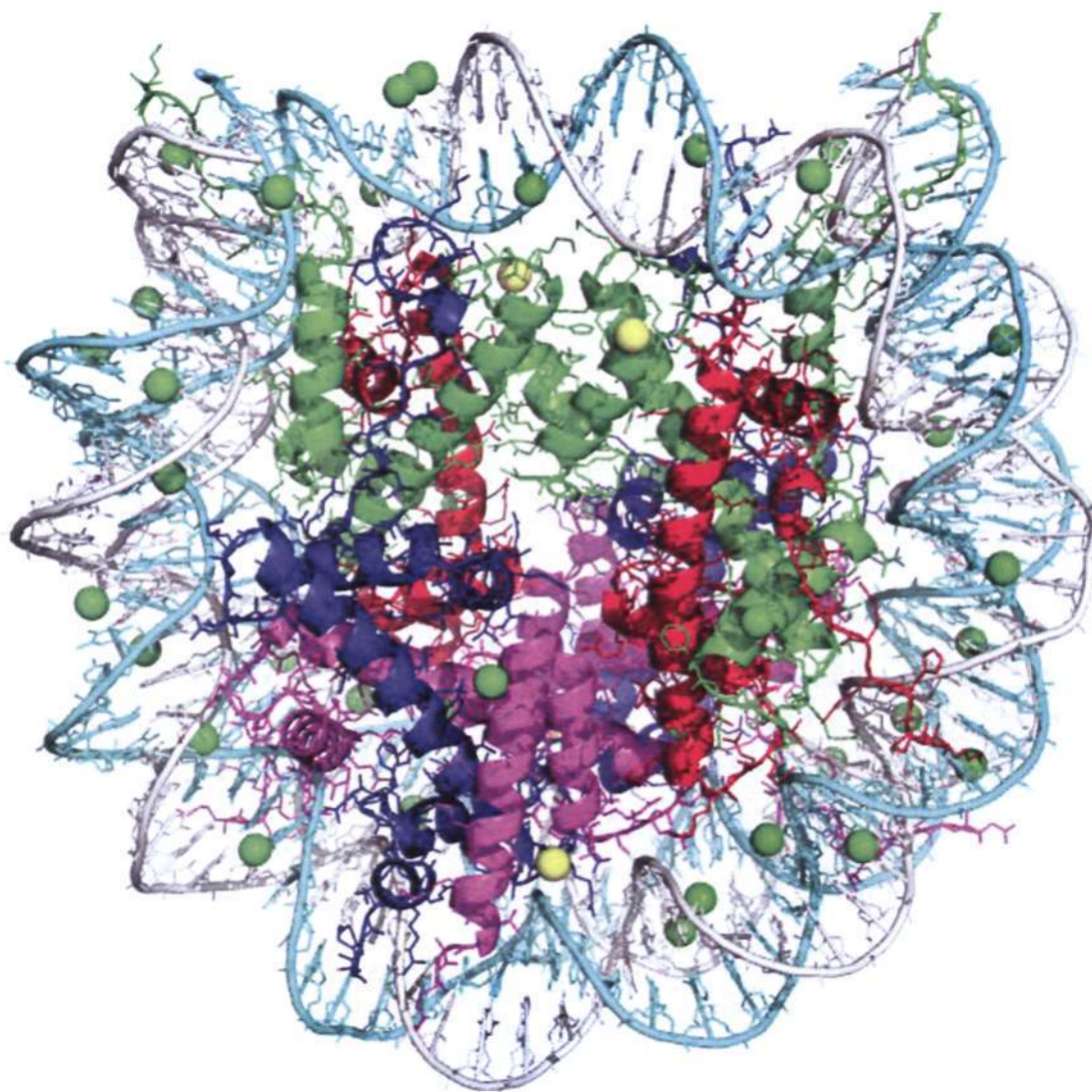


Figure 34. *Crystal structure of the NCP in the presence of 37 mM Ni^{2+} . H3-green, H4-red, H2A-blue, H2B-magenta, I chain DNA-cyan and J chain DNA-grey. Ni^{2+} are denoted as green spheres and chloride ions as yellow spheres.*

Results

Table 2. Crystallographic statistics for Ni²⁺-NCP

Space group	<i>P</i> 2 ₁ 2 ₁ 2 ₁
Unit cell dimensions (Å)	
<i>a</i>	106.12
<i>b</i>	109.64
<i>c</i>	181.10
Resolution range (Å)	2.65-50.97
Unique reflections	61575
Redundancy (last shell)	5.6 (4.3)
Completeness (%) (last shell)	98.2 (89.2)
I/σ	13.7 (2.3)
<i>R</i> _{merge} (last shell)	0.067 (0.495)
<i>R</i> _{factor}	0.244
<i>R</i> _{free}	0.292
<i>R</i> _{anomalous} (overall)	0.045
Anomalous completeness (%) (last shell)	95.8 (78.4)
Anomalous multiplicity (%) (last shell)	2.9 (2.3)
Number of aminoacids	774
Number of Bases	292
Rmsd	
Bond (Å)	0.0076
Angles (°)	1.219
Average B-factor (Å ²)	
Protein	56.54
DNA	113.15

* Numerical values in parentheses are for the highest resolution shell.

4.2.1. General features of Ni²⁺ in NCP structure

The 2.65 Å resolution data provided useful information on the characteristics of Ni²⁺ binding to the NCP. We used the initial model of NCP147 (PDB id-1KX5) to solve the structure of Ni²⁺-NCP. The nickel atoms were observed in the 2*Fo*-*Fc* electron density map at the early stages of refinement. Ni²⁺ were identified based on anomalous difference electron density maps calculated with phases from an NCP model lacking

Results

metal ions. Ni^{2+} were identified as anomalous peaks with magnitudes ranging from 4.0 to 26.4 (highest anomalous peak was observed at a histone site) times the *rms* variation in electron density (σ). Details of ion location and refinement are provided in tables 3 and 4 (Pages 78 and 79).

A few major differences between the Ni^{2+} -NCP and Mn^{2+} -NCP structures were observed. The most conspicuous difference is an alteration of DNA register in the -2 to +2 SHL regions with a shifting of one base pair. In addition, we observed Ni^{2+} at as many as 38 sites, compared to only 14 sites for the manganese structure. Mn^{2+} generally binds only to guanine bases, whereas Ni^{2+} were observed to bind to guanine and adenine bases. The base steps GG and GC were preferred by Mn^{2+} . Whereas, in the case of Ni^{2+} , in addition to GG and GC, GA and AG were also observed as binding sites. Certain sites which were predicted to bind Mn^{2+} were unoccupied, even in the high resolution 1.9 Å structure (Davey and Richmond 2002). This might have been due to the fact that data was not collected at the long-wavelength, Mn-absorption edge (weaker binding sites not detected), which is generally very damaging to crystals. However, in our current structure, several of these sites were found to be occupied by Ni^{2+} , and in addition there were other Ni^{2+} binding sites. In our structure there are two locations where Ni^{2+} is found in the minor groove of NCP, differing from a single site observed previously for Mn^{2+} .

For the histone proteins, Mn^{2+} was found at only one site as compared to Ni^{2+} , which were observed at six locations. The protein site where manganese atom was found forms a contact with the neighboring NCP (Davey and Richmond 2002). In the case of Ni^{2+} , in addition to that site, there is another location where nickel atom is stabilizing an inter-particle contact.

The subtle and major conformational changes induced by Ni^{2+} on the DNA of the NCP were calculated by employing the CURVES program (Lavery and Sklenar 1988), which showed differences in the values of the geometrical parameters such as roll, twist, shift, slide and tilt.

4.2.2. Register shift of DNA in NCP upon nickel ions binding

The DNA in the NCP is highly distorted and the major and minor grooves alternatively face in and out relative to the HO. The high resolution structure of NCP147

Results

(Davey *et al.* 2002; Richmond and Davey 2003) showed that these major and minor groove blocks consist of 5 bp sections, with the exception of the ± 2 and ± 5 superhelix locations (SHL; number of double-helical turns from the central base pair at the particle pseudo dyad axis), which contain 6 bp. There is an extra base pair in the major groove blocks at these SHL compared to other locations. However, this was not observed at one particular position (-2 SHL) in the first high resolution structure of NCP, which contains 146 bp DNA, as well as in 146b (with a different 146 bp DNA sequence) at the -5 SHL position, and in human NCP146 (SHL ± 5) which contains the same 146 bp DNA, but with *Homo sapiens* histone proteins. In these major groove blocks, the occurrence of 5 instead of 6 bp is accommodated by elongation and over-twisting of DNA in relation to other sites, as explained for the structure of NCP145 (Ong *et al.* 2007).

NCP147 containing Ni^{2+} with the complete removal of Mn^{2+} via buffer exchange showed a shift of DNA register between the -2 to +2 SHL. There is an unambiguous stretch of DNA starting from the -2 SHL position. As a result of this stretch, the histone-DNA register is clearly shifted by one base pair, which continues until +2 SHL. We tried to locate the missing base pair using 146 and 145 bp models of NCP as well as with omit maps. Because of the moderate resolution (2.65 Å) and the poor electron density in the regions from ± 2 to ± 1.5 SHL, we were unable to locate the missing base pair. The stretching and base pair shift is clearly supported by the positions of the Ni^{2+} on the DNA as well as by the electron density of the DNA bases.

4.2.3. Stretching of DNA from -2 to -1.5 SHL

The parameters of NCP 147 are similar to those of NCP145 for individual steps; however, due to stretching in NCP145 there is a large difference in roll. Stretching of nucleosomal DNA was observed at the -2 SHL in the structure of Ni^{2+} -treated NCP. The stretching starts at -20 bp and continues until -14 bp. The DNA stretching was quite obvious based on the electron density maps and the position of the metals in the dyad region. The DNA of NCP145 also reveals clearly stretching at two sites SHL -2 to -1 and SHL 1.5, and this DNA is similar to that of NCP147 except for the deletion of a base pair at ± 3 position on the either side of the particle dyad axis (Fig 35). This DNA was designed such that the critical DNA bases maintain the same histone base-pair register for

Results

the outer regions relative to NCP147. However, Ni^{2+} treatment of NCP147 alters the base pair register near the dyad region, which must arise from ion binding imposed modulation of DNA conformation.

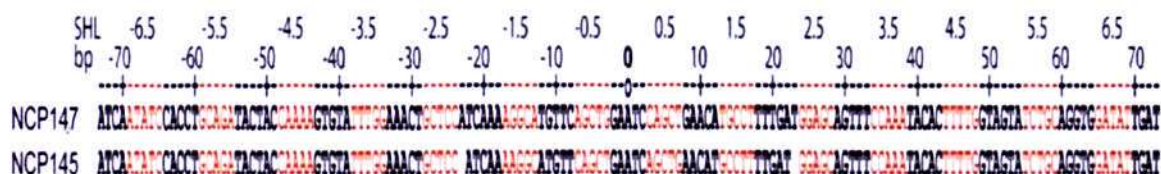
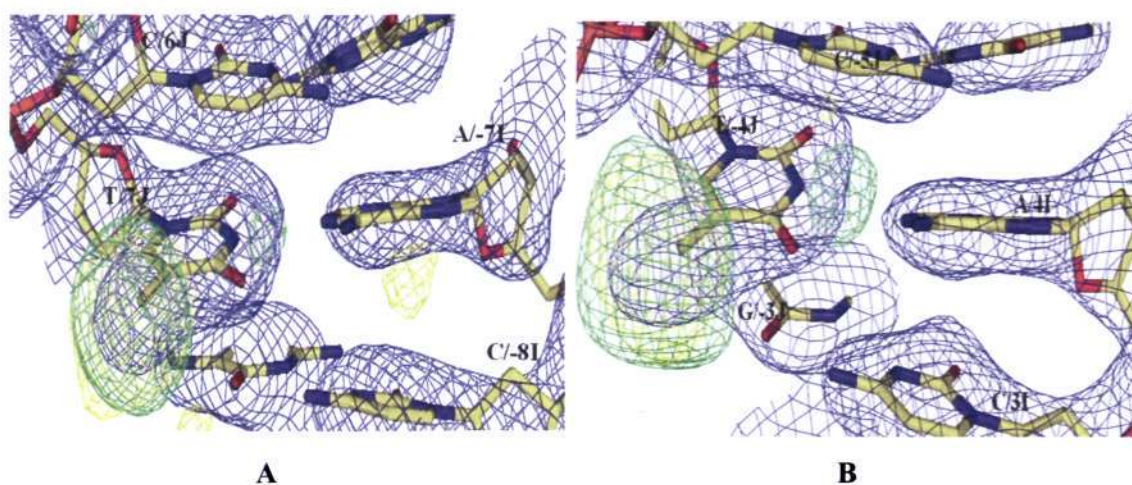


Figure 35. Comparison of DNA sequences from the crystal structures of NCP147 and NCP145. Minor groove blocks are highlighted in orange, and the base pair numbering scheme is relative to NCP147. A gap in the DNA sequence represents a shift in histone–base-pair register from stretching (The figure is adapted from Ong *et al.* 2007).

4.2.4. Position of nickel ions

The NCP147 model without Mn^{2+} was used to solve the structure of heavy metal-treated NCP. Most of the strongest binding sites of Ni^{2+} , identified based on the anomalous signal, were identical to those of Mn^{2+} . Around the NCP center, the initial anomalous map based on the molecular replacement model indicated that the Ni^{2+} binding of the methyl groups of thymine bases (Fig. 36 and 37). Such mode of binding is inconsistent with chemical principles, as methyl groups of thymines are neutral and unable to react with the positively charged metal ion. These apparent positions of Ni^{2+} revealed that the DNA of NCP147 is shifted by one base pair from the -2 to +2 SHL region. Since the DNA of NCP147 is palindromic, it was essential to validate the direction of shifting.



Results

Figure 36. Position of nickel ions near the NCP dyad from the initial molecular replacement model. Ni^{2+} ion binding sites were observed adjacent to thymidine bases (A) 7T/J and (B) -4T/J. A $2fo-fc$ map (contoured at 1.5σ) is colored in blue, a $+fo-fc$ map (contoured at 3σ) in green and an anomalous difference map (contoured at 3σ) in yellow.

We observed two positions occupied by Ni^{2+} near thymine residues 7T/J and -4T/J (Fig. 36). If the DNA shifts one base pair to the side of 7T/J, then the 7T/J position is replaced by 8G/J and that of -4T/J by -3G/J (Fig. 37C). If the shift occurred towards the other direction (Fig. 37D), then both metal positions would be occupied by cytosine bases, which should not be capable of forming coordinating interactions with cations. Thus, the base shift occurs clearly in the -2 to +2 SHL direction (Fig. 37C).

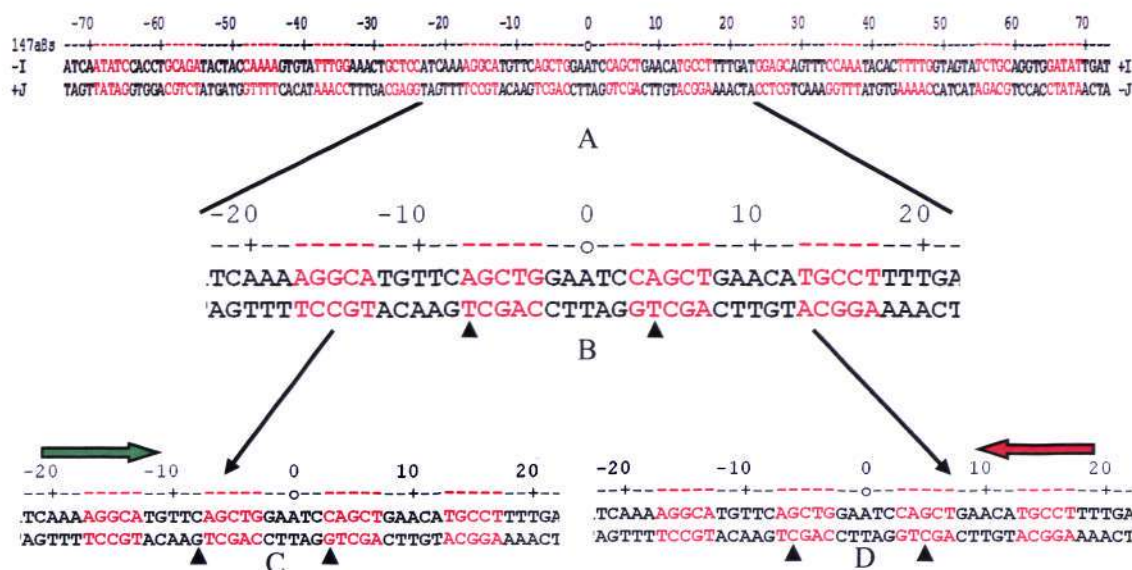


Figure 37. Orientation of the DNA with respect to metal ions. (A) NCP147 DNA sequence. (B) Enlarged view of the dyad region with the initial metal atoms positions indicated by triangle symbols. (C) Shifting of the DNA from 7T/J to 8T/J results in alteration of the base from thymine to guanine. Shifting in this orientation also leads to change in the base in the other metal binding site from thymine to guanine (-4T/J to -3G/J). Orientation in this direction is highly favored and is represented by green arrow. (D) Orientation in the opposite direction is not favored and is represented by a red arrow. Change of register in this direction yields replacement of thymine with cytosine in both instances; hence this orientation is not favored.

Results

4.2.5. Electron density of the DNA bases

In addition to the position of metals, shifting of the DNA bases was confirmed by the electron density profiles. Although electron density was overall poor at the -2 SHL position, the density from -1 SHL to +1.5 SHL is very clear and it reveals the shift of DNA bases in this region. When the register is shifted by one base pair, the atoms of the bases fit properly within the electron density map (Fig. 38) and the position of metals in the major groove show clear coordination with the N7 atom of guanines. Moreover, there was an obvious distinction between the purines and pyrimidines in the map. After a cycle of refinement, there was no negative electron density observed in the shifted bases. Hence, this verifies the direction and extent of the shift.

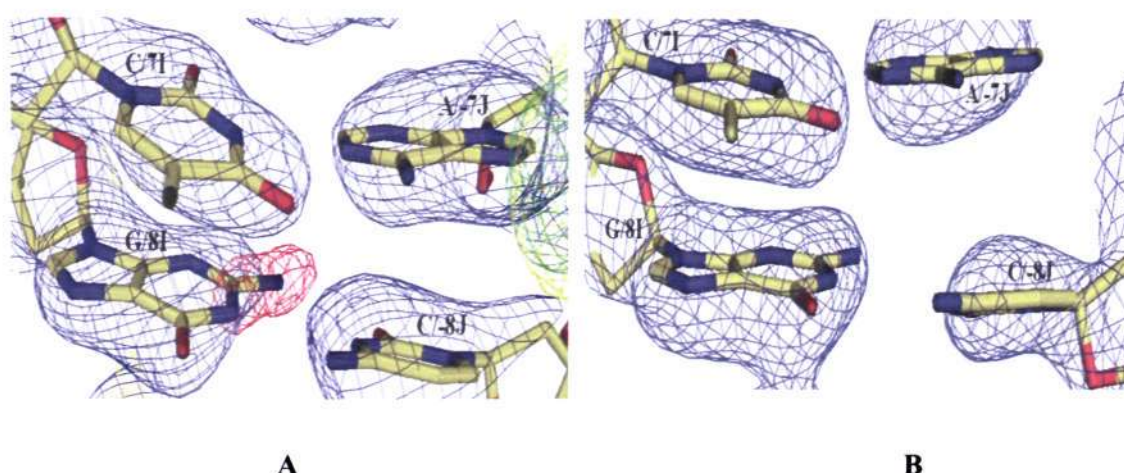


Figure 38. Electron density map for the initial NCP147 model. (A) Initial maps calculated from Mn^{2+} -NCP147 as a starting model showed negative difference electron density (red map) associated with 8G/I before shifting the base register. This location is supposed to be occupied by the adjacent thymidine nucleotide (7T/I) (B) Electron density maps after shifting register, followed by refinement. $2fo-fc$ maps (1.5σ) are colored in blue, $+fo-fc$ maps (3σ) in green, $-fo-fc$ maps (3σ) in red and an anomalous difference map (3σ) in yellow.

4.2.6. Missing base pair in the compaction region

Stacking of DNA termini between adjacent particles in the crystal helps to stabilize DNA stretching (Ong *et al.* 2007). In our Ni^{2+} treated crystal, we observed stretching starting at -2 SHL, resulting in shifting of bases by one base pair that was

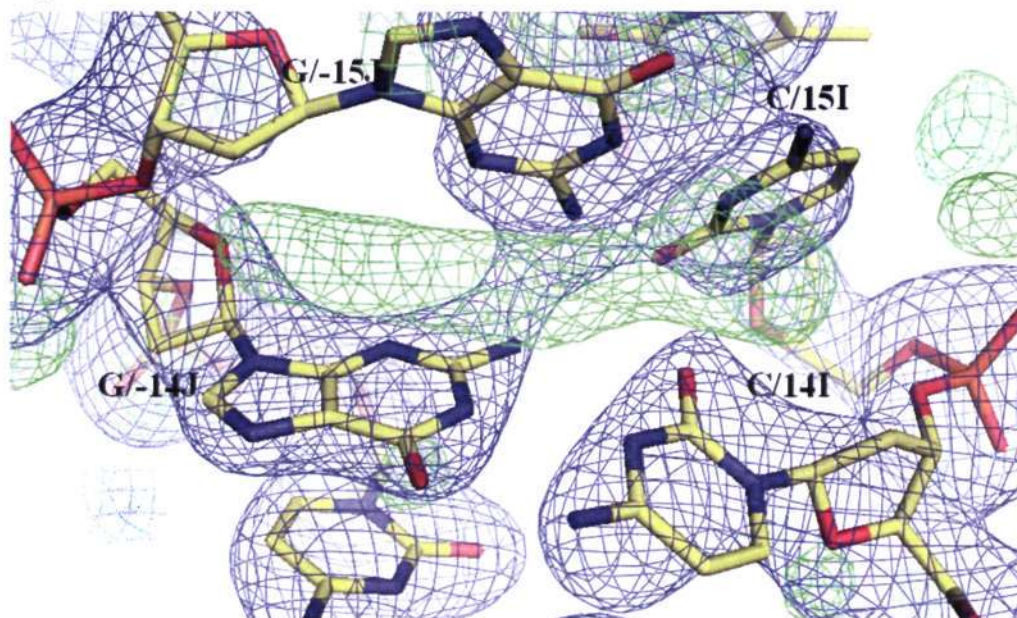
Results

apparently stabilized up to the +2 SHL region. This region will be referred to as the compaction region henceforth. Electron density in the compaction region (+1.5 to +2 SHL) was poor probably due to the presence of flipped out bases. We were unable to locate the missing base pair in this region. However, the shifting of bases apparently does not extend beyond +2 SHL, which is indicated by the in-register presence of Ni^{2+} at prominent downstream guanine sites, starting with 27G/I. Also, there is clear electron density beyond the +2 SHL region, allowing unambiguous discrimination of bases.

Thus, the expansion zone in the other particle half, where stretching starts from the -2 SHL region, is confirmed by the presence of in-register guanine-metal binding sites upstream, starting at 27G/J, which makes a key inter-particle crystal contact (explained in detail in 4.2.12 section of this chapter). Therefore, it is evident that a base pair is flipped out or out of the double helical stack around the compaction region. In order to confirm this, we prepared omit maps, and we also made use of other NCP models, including NCP146 and NCP145.

4.2.7. Different NCP models and omit maps to locate the missing base pair in the compaction region

We scrutinized two different NCP models, NCP146 and NCP145, in order to identify the missing base pair in the compaction region, since the NCP147 structure is nearly identical to that of NCP146 and NCP145.



Results

Figure 39. A view of the electron density map in the compaction region calculated using the NCP145 model. A single missing base pair was observed in the compaction region of Ni^{2+} -NCP147 relative to NCP145. The electron density map shows the missing base pair (green). A $2fo-fc$ map (1.5σ) is colored in blue, and a $+fo-fc$ (3.0σ) map in green.

When we used NCP146 as a model, we did not observe any positive density in the compaction region or any other region of the DNA. Even the backbone density of the DNA appeared continuous and did not provide any information about the missing base pair. Moreover, when we utilized the double-stretch NCP145 as our model to solve the structure of Ni^{2+} -NCP147, we did not observe the sought after two additional base pairs in one of the stretched regions of NCP145. In this case, we only found evidence for one base pair missing from the compaction region relative to the NCP145 model (Fig. 39).

The next step was to create omit maps to locate the missing base pair by deleting the atoms in the compaction region as well as in the stretching region, followed by cycles of refinement. Even then, the difference density maps in the compaction regions did not reveal any extra density (Fig. 40).

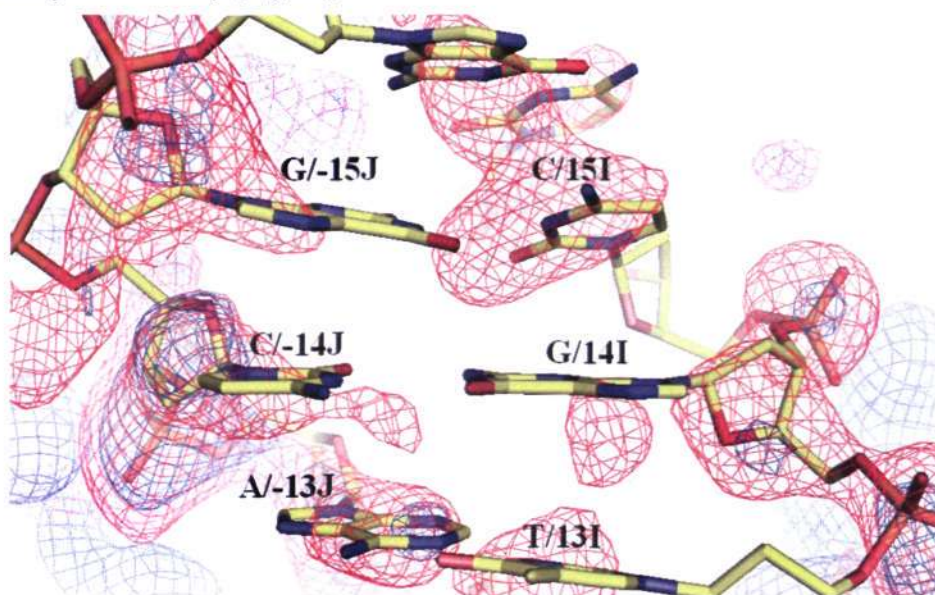


Figure 40. Omit map in the compaction region. A zone of eight base pairs was deleted in the compaction region followed by refinement to generate an omit map of the region. Electron density in the compaction region of NCP147 was so poor that we observed only one strand of the DNA in the omit map (red). Original coordinates of NCP147 are shown

Results

for clarity. A $2fo-fc$ (1.5σ) map is colored in blue and a $+fo-fc$ (3.0σ) map in red.

In addition to omit maps, we also introduced an extra base pair in the compaction region followed by a cycle of refinement, but the maps showed negative density. Thus, we refined our final model by deleting an A:T base pair (near the compaction region) and renumbering the DNA to 146 bp (I chain = 5' -73 to +72 3' and J chain = 5' -72 to +73 3'). As a result, the locations of metals occupying the same relative positions in both halves will differ from each other by \pm one bp. Table 4, column 2 shows the respective positions of metal ions from each half of the DNA, where they are clearly represented by their current numbers. For example, previously the 61/I location would correspond to the 61/J position, whereas after the deletion of one base pair with the present numbering, this would be 60/I versus 61/J.

4.2.8. Occupancy and B-values for nickel atoms in the Ni^{2+} -NCP structure

In order to get accurate values for metal thermal factors (B-factors) and occupancies, we used the program Mlphare in the CCP4 suite. This program aided in the accurate determination of atomic parameters based on the anomalous difference signal of the heavy atom (Nickel). Multiple cycles of Mlphare were applied until the independently refined B-factors and occupancies converged. The anomalous occupancy values are initially on an arbitrary scale. These were subsequently normalized with respect to the known fully occupied divalent metal binding site, which mediates a histone-histone interparticle contact in the crystal (Davey et al., 2002; Table 3 [ATOM1]).

4.2.9. Sites of Ni^{2+} binding

Like Mn^{2+} , Ni^{2+} also bind preferably to the DNA major groove of NCP, where they interact with the N7 and O6 atoms of guanine and the N7 atom of adenine residues (Tables 3 and 4). In general, the major groove edge of DNA presents highly favorable binding sites for cations as a result of the prominent electronegative region associated with the N7 and O6 atoms of guanine (Pullman and Pullman 1981; Hunter 1993; Packer et al. 2000; Davey and Richmond 2002). The interactions of Ni^{2+} with different base

Results

steps (GG, GC, GA, GT, AG and AA) are mediated by either direct coordination to the N7 and O6 atoms and/or via the water molecule ligands of the metal. Due to lack of high resolution data and relatively high B-factors, water molecules are generally not observed in proximity to the DNA. In any case, Ni^{2+} shares a preference with Mn^{2+} for octahedral coordination geometry, meaning the two ion types are expected to display similar solvent-mediated interactions.

Interaction between the metal ions and its coordination shell water molecules occurs electrostatically by means of the positive charge of the metal ion, which is effectively propagated outward through the hydrogen atoms of the bound water molecules that are oriented to interact with the acceptor species. Overall, there are 10 different types of dinucleotide steps, of which 9 are present in the NCP147-DNA sequence. Only the CG base step is not represented. In fact, due to the position of the electropositive cytosine amino group which protrudes into the major groove of DNA, the CG base step is usually not suited for cation binding (Auffinger and Westhof 2000).

Table 3. Occupancy and B-factors for Ni²⁺ calculated using the MLPhare program

	Position	Real Ligand Bfac (A)	Real Bfac Ni ²⁺ (B)	Normalized Occupancy (C)	Aso Signal (D)	Cycle 6 Bfac	Cycle 6 Aocc	Cycle 5 Bfac	Cycle 5 Aocc	Cycle 4 Bfac	Cycle 4 Aocc	Cycle 3 Bfac	Cycle 3 Aocc	Cycle 2 Bfac (E)	Cycle 2 Aocc (F)	Cycle 1
ATOM1	77ASP/E	44.32	47.89	1.00	23.6	116.92	17.55	115.53	17.40	115.53	17.40	115.53	17.40	115.67	17.16	
ATOM2	27GDI/J	96.43	70.08	0.73	15.4	118.71	12.81	117.69	12.81	117.69	12.72	117.69	12.72	118.43	12.47	
ATOM3	60GDI	97.72	70.98	0.82	14.6	137.24	14.39	130.81	13.65	130.81	13.65	130.81	13.65	121.91	12.59	
ATOM4	3GDI	86.46	48.09	0.56	12.1	137.35	9.87	131.09	9.38	131.09	9.38	131.09	9.38	122.72	8.68	
ATOM5	61GDI/J	109.97	69.5	0.78	12	145.26	13.69	137.04	12.91	137.04	12.91	137.04	12.91	125.70	11.80	
ATOM6	48GDI/J	105.55	78.64	0.76	11.5	130.17	13.36	125.57	12.88	125.57	12.88	125.57	12.88	119.22	12.20	
ATOM7	3GDI/J	72.48	59.38	0.62	11.3	116.77	10.91	115.31	10.76	115.31	10.76	115.31	10.76	113.31	10.51	
ATOM8	47GDI/J	105.41	83.04	0.70	10.6	124.81	12.20	124.85	11.80	124.85	11.80	124.85	11.80	119.05	11.18	
ATOM9	106HS/D	61.67	98.29	0.72	9.6	144.16	12.71	137.27	12.06	137.27	12.06	137.27	12.06	127.04	11.06	
ATOM10	56GDI/J	119.92	111.17	0.81	8.7	175.98	14.28	159.08	12.60	159.08	12.60	159.08	12.60	136.86	10.44	
ATOM11	79HS/H	64.19	49.12	0.31	8.6	91.47	5.37	95.38	5.62	95.38	5.62	95.38	5.62	101.40	5.97	
ATOM12	8GDI/J	81.31	55.37	0.35	8.3	100.40	6.18	102.66	6.33	102.66	6.33	102.66	6.33	106.15	6.53	
ATOM13	6GDI/J	94.85	61.14	0.41	8.3	111.34	7.16	112.37	7.29	112.37	7.29	112.37	7.29	113.10	7.41	
ATOM14	26GDI/J	85.09	52.26	0.49	7.7	123.73	8.61	121.59	8.48	121.59	8.48	121.59	8.48	117.40	8.18	
ATOM15	106HS/H	69.61	79.41	0.47	7.1	127.62	8.32	124.93	8.15	124.93	8.15	124.93	8.15	119.59	7.79	
ATOM16	55GDI/J	116.78	75.12	0.69	7.1	163.92	12.10	151.54	10.96	151.54	10.96	151.54	10.96	133.68	9.32	
ATOM17	35GDI/J	95.25	81.95	0.56	6.8	125.48	9.84	122.63	9.67	122.63	9.67	122.63	9.67	116.17	9.36	
ATOM18	29ADI/J	102.2	72.79	0.51	6.7	168.09	8.99	155.26	8.26	155.26	8.26	155.26	8.26	137.20	7.22	
ATOM19	34GDI/J	107.35	97.18	0.42	6.4	150.14	7.36	140.79	6.94	140.79	6.94	140.79	6.94	128.49	6.38	
ATOM20	79HS/D	72.43	61.17	0.41	6.2	130.36	7.17	126.34	6.96	126.34	6.96	126.34	6.96	119.87	6.59	
ATOM21	18ADI/J	134.41	72.5	0.38	6.2	146.33	6.74	138.78	6.37	138.78	6.37	138.78	6.37	127.66	5.79	
ATOM22	38-64AD/J	90.59	60.85	0.26	5.9	115.91	4.55	115.63	4.60	115.63	4.60	115.63	4.60	113.67	4.62	
ATOM23	5GDI/J	107.92	62.41	0.40	5.8	122.61	7.06	122.01	7.11	122.01	7.11	122.01	7.11	118.65	7.00	
ATOM24	23GDI/J	117.02	62.11	0.27	5.4	107.65	4.69	109.81	4.83	109.81	4.83	109.81	4.83	111.84	4.98	
ATOM25	64GDI/J	102.56	90.54	0.57	5.3	160.18	9.93	147.60	8.98	147.60	8.98	147.60	8.98	130.80	7.70	
ATOM26	28ADI/J	97.1	73.48	0.42	5.2	135.00	7.43	129.28	7.17	129.28	7.17	129.28	7.17	121.38	6.78	
ATOM27	33GDI/J	108.21	62.77	0.32	5.2	122.89	5.67	120.96	5.67	120.96	5.67	120.96	5.67	117.32	5.61	
ATOM28	57GDI/J	93.42	80.57	0.38	5	198.58	6.64	173.71	5.76	173.71	5.76	173.71	5.76	143.46	4.67	
ATOM29	34GDI/J	92.46	56.39	0.27	5	101.38	4.77	104.60	4.98	104.60	4.98	104.60	4.98	108.38	5.24	
ATOM30	14GDI/J	141.56	69.54	0.29	4.8	128.53	5.00	125.95	4.94	125.95	4.94	125.95	4.94	120.36	4.74	
ATOM31	38-69AD/J	109	88.94	0.42	4.8	168.67	7.36	153.77	6.54	153.77	6.54	153.77	6.54	133.68	5.48	
ATOM32	52GDI/J	139.8	79.84	0.51	4.6	193.81	9.03	173.05	7.80	173.05	7.80	173.05	7.80	145.15	6.20	
ATOM33	70GDI/J	88.27	69.97	0.28	4.6	129.54	4.96	124.66	4.80	124.66	4.80	124.66	4.80	117.70	4.56	
ATOM34	64GDI/J	142.73	92.67	0.31	4.5	232.13	5.47	198.19	4.45	198.19	4.45	198.19	4.45	155.97	3.27	
ATOM35	6GDI/J	91.62	89.96	0.31	4.5	223.73	5.43	189.48	4.47	189.48	4.47	189.48	4.47	151.38	3.43	
ATOM36	51GDI/J	133.1	77.05	0.33	4.4	139.92	5.79	133.37	5.53	133.37	5.53	133.37	5.53	121.09	5.14	
ATOM37	90ASP/C	49.05	53.13	0.29	4.3	141.84	5.02	133.90	4.72	133.90	4.72	133.90	4.72	123.45	4.35	
ATOM38	71GDI/J	91.19	56.03	0.21	4.3	94.64	3.77	98.46	3.96	98.46	3.96	98.46	3.96	104.54	4.25	
ATOM39	65GDI/J	146.54	108.18	0.47	4.1	171.05	8.28	155.06	7.43	155.06	7.43	155.06	7.43	134.23	6.28	
		99.12	72.55													

(D) Peak heights observed in the anomalous difference map. The highest signal was found for a histone site at 23.6σ. 4σ was set as the minimum value for introducing metal ions into the model. (E) The anomalous occupancy values were refined using the Mlphare program, with each cycle consisting of 30 rounds of refinement. In the first cycle, only occupancy was refined, and in the subsequent cycle only the (E) B-factor was refined. Anomalous occupancy and B-factor were alternately refined until both converged, which occurred in the 6th cycle. (C) Occupancy values were normalized with respect to the highest converged value. (B) Real B-factor values were obtained by applying the normalized anomalous occupancy values to refinement using the Refmac program. (A) B-factor values of the ligand atom to which nickel ion was bound in the NCP structure.

Table 4. Ni²⁺ sites in the DNA of NCP

Site (A)	Location bp (B) I/J chain	Sequence 5'-3' (C)	Bond distance (Å) I/J chain (D)	Anomalous Signal (σ) I/J chain	Occupancy I/J chain	Average occupancy	B-factor (Å ²) I/J chain	Mode of binding	Roll ° (E)	Shift (Å)	Slide (Å)	Slide at 5' TG _n (Å)	5' N7-3'O6 distance (Å)
1-GG	60/61	AGGT	2.0/2.2 N	14.6/12	0.82/0.78	0.8	71/69	3-bond	11.6	-0.88	-0.25	-	4.02
2-GG	47/48	TGGT	2.3/2.2 N	10.6/11.5	0.70/0.76	0.73	83/79	3-bond	-12.9	-0.74	0.49	0.9	4.35
3-GG	-3/-3	TGGA	2/2.6 N	12.1/11.3	0.56/0.62	0.59	48/59	3-bond	-5.65	-0.48	0.42	0.43	4.14
4-GG	-35/-34	TGGA	2.4/2.6 N	6.8/6.4	0.56/0.42	0.49	82/97	4-bond	-15.9	0.99	0.71	1.06	3.41
5-GC	26/27	AGCA	2.5/2.4 O	-	-	-	-	-	-	-	-	-	-
6-GC	-/5	AGCT	2.2/2.1 N	7.7/15.4	0.49/0.73	0.61	52/70	3-bond	-7.18	-0.84	0.13	-	-
7-GC	-/14	TGCC	-/2.2 N	-/5.8	-/0.4	0.2	-/62	3-bond	-2.37	-0.71	-0.27	-	-
8-GG	64/-	TGGA	-/2.2 N	-/4.8	-/0.29	0.145	-/70	3-bond	11.9	-0.01	0.46	0.4	-
9-GA	-56/-55	AGAT	2.3/- N	5.3/-	0.57/-	0.285	91/-	3-bond	5.82	-0.45	-0.32	-	-
10-GC	-6/-6	AGCT	2.5/2.3 N	8.7/7.1	0.81/0.69	0.75	111/75	3-bond	4.5	-0.3	-0.31	-	-
11-GA	-8	TGAA	2.6/2.2 N	4.5/8.3	0.31/0.41	0.36	90/61	3-bond	-1.52	-0.7	-0.07	-	-
12-GG	-34/-33	TGGA	-/2.3 N	-/8.3	-/0.35	0.175	-/55	3-bond	-3.4	-1.14	0.72	-0.36	-
13-GG	-/64	TGGA	2.2/2.2 N	5/5.2	0.27/0.32	0.295	56/63	3-bond	-3.18	-1.88	0.09	-	-
14-AG	28/29	CAGT	-/2.5 N	-/4.5	-/0.31	0.155	-/93	3-bond	3.81	-0.83	0.51	-1.66	3.11
15-GT	51/52	AGTA	2.5/2.4 N	5.2/6.7	0.42/0.51	0.465	73/73	3-bond	4.7	-0.8	0.28	-	-
16-GA	70/71	TGAT	2.6/2.1 O/N	4.4/4.6	0.33/0.51	0.42	77/80	3-bond	9.98	-0.43	-0.14	-	-
17-GC	-/58	TGCA	2.5/2.2 N	4.6/4.3	0.28/0.21	0.245	70/56	3-bond	-0.25	-1.58	0.42	0.62	-
18-GG	23/0	TGGA	-	-	-	-	-	-	-	-	-	-	-
19-GG	-25	TGGA	2.5/- N	5.4/-	0.27/-	0.135	62/-	3-bond	-5.73	1.04	0.06	0.23	3.58
20-GC	57/-	TGCA	-	-	-	-	-	-	-	-	-	-	-
21-AA	-/18	AAAG	2.5/- O	5/-	0.38/-	0.19	81/-	3-bond	-1.47	0.47	-0.09	1.52	-
22- <u>sg</u>	64	GGA	-/2.2	-/6.2	-/0.38	0.19	-/72	3-bond	6.59	-0.2	0.24	-	-
23- <u>sg</u>	69	TTG	-	5.9	0.26	0.13	-	Minor grv.	-	-	-	-	-
24- <u>sg</u>	13	ATG	-	4.8	0.42	0.21	-	Minor grv.	-	-	-	-	-

(A) Ni²⁺ binding sites. All sites are in the DNA major groove except for 22-sg, 23-sg and 24-sg in the minor groove. GG, GC, GA, GT, AG and AA denote the type of base step to which the Ni²⁺ is binding. Mn²⁺ binding sites are occupied by Ni²⁺ are denoted by **gray background**. (B) Distance in base pairs from the site of the central base pair (bp 0) on the molecular dyad axis. Chain "I" runs from base pair -73 at the 5' terminus, whereas Chain "J" runs from base pair +72 at the 5' terminus to -73 at the 3' terminus. Although 147-bp DNA is 2-fold sequence symmetric about bp 0, but due to the single base pair missing, it is renumbered to 146X version of 147. (C) Dinucleotide step defining Ni²⁺ binding sites in the major groove are underlined. Direct binding of Ni²⁺ to a base highlighted in blue. (D) Bond distance from metal center to the N7 and O6 ligands of DNA atom. The two values correspond to the two halves of the DNA superhelix. (E) Parameter values are the average for two base steps, one from the identical sequence in each half of the DNA superhelix. DNA geometrical parameters are defined in (Dickerson 1989). Since certain sites were not occupied by Ni²⁺ in both of the halves, thus, parameter value is derived based on single site.

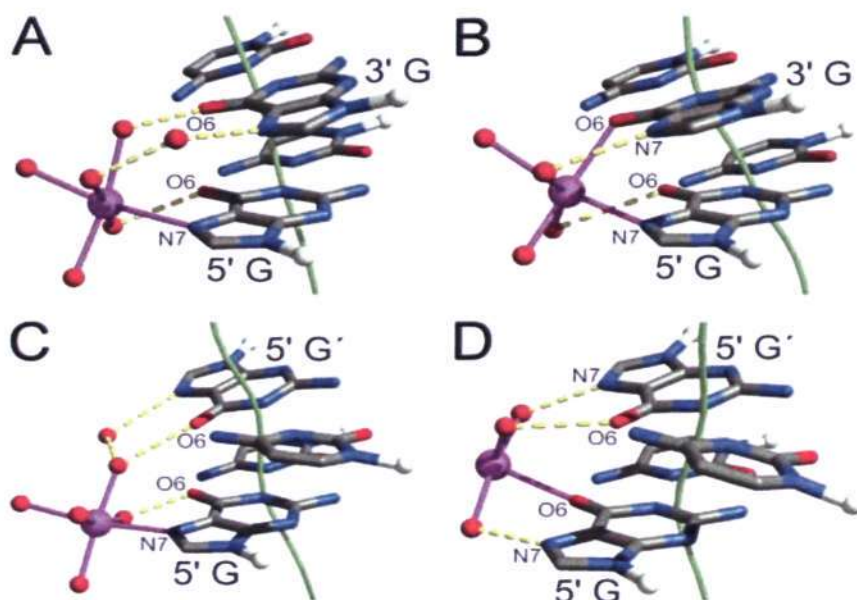
Results

4.2.10. Modes of Ni^{2+} binding in the major groove

Even though with the moderate resolution (2.65 Å) where smaller number of water molecules was distinguishable, we could derive the mode of metal ion binding to the DNA based on the distance between the metal ions and DNA atoms of the NCP. As a general rule, metal atoms maintain well coordinated water molecules, but only at a higher resolution can they be discerned.

On the whole, there are two modes of metal binding that occur in the DNA major groove. In the case of Mn^{2+} , the three-bond and four-bond modes were observed for both GG and GC steps (Fig. 41 A–D), whereas for Ni^{2+} the four-bond mode was observed only at two GG step (Table 4). Therefore, three-bond mode was predominant in the case of Ni^{2+} .

In three-bond mode, metal ions directly bind to one of the N7 atoms of guanine bases (5' for GG), and indirectly with its coordinated water molecule to the O6 atom of the same guanine base (Fig. 41 A and C). There is another coordinated water molecule which forms a hydrogen bond with the O6 atom of the second guanine (3' for GG). The 3' guanine N7 atom is linked to the same or a third metal-coordinated water molecule by means of bridging additional water molecule.



Results

Figure 41. Binding mode of manganese ions to the DNA major groove of NCP. Mn^{2+} are depicted in Magenta. GG and GC base steps are shown here for both three and four bond mode. A and C indicate the three- bond mode of GG and GC steps. B and D indicate the four-bond mode of GG and GC steps. A non-zero shift parameter for a base step is visualized as a deviation of the double helix axis (green). Coordination bonds (magenta) between the metal ions (magenta) and water molecules (red), and hydrogen bonds (yellow) between bases and first and second shell, coordinated water molecules are shown. This being a high resolution structure, all the manganese atoms were found to be completely hydrated and interactions with DNA atoms were quite visible. In the case of Ni^{2+} , GC four-bond mode was not seen in the dyad region of the NCP. Though this site was occupied by nickel ions in one half of the DNA (site-6), it formed a three-bond mode instead of four. The figure is adapted from Davey and Richmond (2002).

In the case of four-bond mode (GG), the coordination of the 5' guanine is similar to that in the three-bond mode, but metal mediates another direct contact with the O6 atom of other guanine. In the GC four-bond mode, the N7 and O6 atoms have interchanged metal ion and metal-coordinated water molecule interactions (Fig. 41-D). The metal-coordinated water molecule forms bond with the N7 and O6 atoms of second guanine in four-bond GC mode.

In the high resolution NCP147, there were a total of 8 three-bond mode sites observed for Mn^{2+} (6 at GG step and 2 at GC step). The four-bond mode sites were characterized by 2 at GG and 2 at GC steps. In contrast, in the structure containing Ni^{2+} , we classified a total of 28 three-bond mode site, out of which 11 were at GG steps and 7 at the GC steps. The four-bond mode was observed twice and it was only for GG steps. The four-bond mode GC site observed in the dyad region (5 bp, Fig. 41-D) for Mn^{2+} was not seen in the case of Ni^{2+} . Instead Ni^{2+} was coordinated in three-bond mode. This is probably due to the overall conformation changes of DNA near the dyad region induced by the binding of this soft metal.

4.2.11. New metal binding sites in the Ni^{2+} -NCP structure

In addition to GG and GC steps, which are predominantly occupied by metal, there are other steps such as GA, GT, AG and AA to which Ni^{2+} are coordinated, which were not predicted to be metal binding sites based on the high resolution Mn^{2+} data

Results

(Davey and Richmond 2002). In the Ni^{2+} -NCP147 structure, GA steps were occupied at five locations, GT and AG at two sites and AA at one. We presume that all these base steps form three-bond interactions. In the case of GA steps, nickel ion binds directly to the N7 atom of the guanine base, and based on the distance, we surmise that it binds indirectly with its water molecule to the O6 atom of the same guanine and with another water molecule to the adjacent N7 atom of the 3' - adenine base.

In GA base steps, nickel ions occupied several sites (9, 11 and 16 - Table 4) on the NCP-DNA. We compared the GG site from the high resolution Mn^{2+} structure, 61/I chain, 5'-AGGT-3', which differs by one base (G instead of A) with the Ni^{2+} tetra-nucleotide site (-56/I chain, 5'-AGAT-3') by least squares superposition (LSS) of DNA backbone. Both structures appeared similar, thus nickel ion might bind to the GA step similarly as it binds to GG steps, provided the conformation of the tetra-nucleotide is similar (Fig. 42).

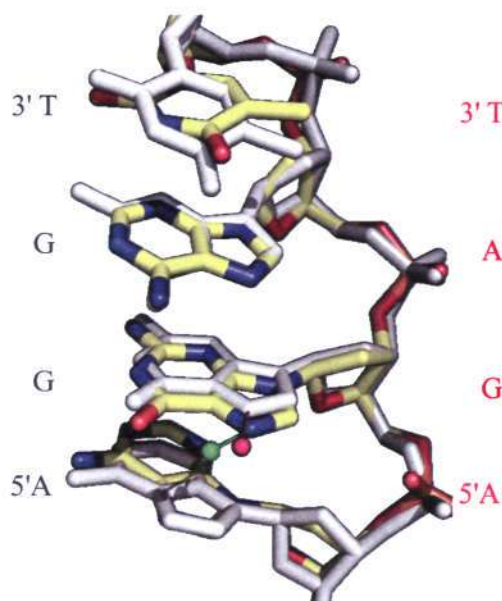


Figure 42. Structural comparison of 5'-AGAT-3' (multi-color) with 5'-AGGT-3' (gray) using least squares superposition (LSS). 5'-AGAT-3' tetra-nucleotide superposed with 5'-AGGT-3' showed no major differences in the conformation of the tetra-nucleotide and thus suggesting that conformation of the tetra-nucleotide favors binding of nickel ions.

The other possible GA base steps are TGAA and TGAT in the DNA of NCP147. For TGAA and TGAT, only half of the sites were occupied by Ni^{2+} , comparing to AGAT

Results

sites, which were all occupied. Furthermore, G-bases of the GA steps such as 5'-GGAT-3' were occupied by nickel ions.

Mn^{2+} are known to be highly selective for GG and GC base steps (Davey and Richmond 2002). Based on the conformational similarity between the two tetra-nucleotides 5'-AGGT-3' and 5'-AGAT-3', we assume that the Mn^{2+} can discriminate between GA from a GG steps. Even though the conformation of both tetra-nucleotides are similar (Fig. 42), Mn^{2+} shows selectivity toward specific base steps of the DNA in the NCP.

Ni^{2+} appears to interact with the guanine bases wherever possible, provided the base step conformation is favorable for ion binding. This feature could be seen in an additional base step, GT. When we superposed the tetra-nucleotide (5'-AGTA-3') with (5'-AGCA-3'), which is a known metal binding site for Ni^{2+} as well as for Mn^{2+} , the superposed structure did not show any major structural differences and the overall conformation of the tetra-nucleotide appeared to be similar (Fig. 43). This supports the notion that if preferred DNA conformation provided, Ni^{2+} has a strong affinity for the guanine base.

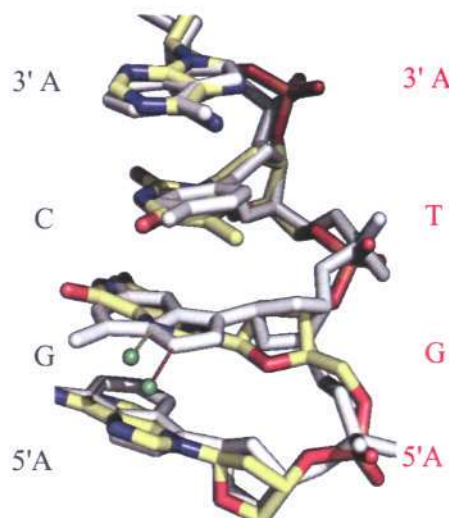


Figure 43. Structural comparison of 5'-AGTA-3' (multi-color) with 5'-AGCA-3' (gray) using LSS. 5'-AGTA-3' tetra-nucleotide and nickel ion forming direct contact (yellow) with N7 atom of guanine superposed with 5'-AGCA-3' and nickel ion (red) in direct contact with N7 atom of guanine. No major differences in the conformation of the tetra-nucleotide are observed suggesting this tetra-nucleotide favors binding of nickel ions.

Results

In two sites (14 and 21; Table-3), Ni^{2+} showed preference for adenine over guanine where it was binding directly to the N7 atom of the adenine base. Site 14 is in the base step AG (5'-CAGT-3'). This is the first crystallographic structure which shows the binding of nickel ions to an adenine base. Binding of nickel ions has been described in the crystal structure of oligonucleotide DNA d(CGTATATACG) which is rich in AT base steps (Abresica *et al.* 1999). In the study of this AT rich oligonucleotide, the interactions of nickel ions were observed only with the entire guanine base, but not with the adenine residues, even though the concentration of nickel chloride was not limiting (10 mM) and there were no constraints on DNA caused by histone proteins, as in the case of NCP-DNA. Thus, this implies that specific DNA sequence and the conformation changes on DNA imposed by association with HO, as well as the initial binding of Ni^{2+} at more favored sites, may predispose adenine base (Fig. 44A) in other regions, such as (28/I-29/J) to Ni^{2+} attack. In addition, there is one more site where Ni^{2+} was found to bind to an adenine base. The site (5'-AAAG-3') was quite unusual and pointed to a new base step AA (Fig. 44B), potentially with important implications. It was localized in the compaction region of the DNA where one base pair was missing. The anomalous signal for the Ni^{2+} in this site is 6.2σ (site 21; Table-4). Moreover, we did not observe any anomalous signal in the other half of the NCP-DNA.

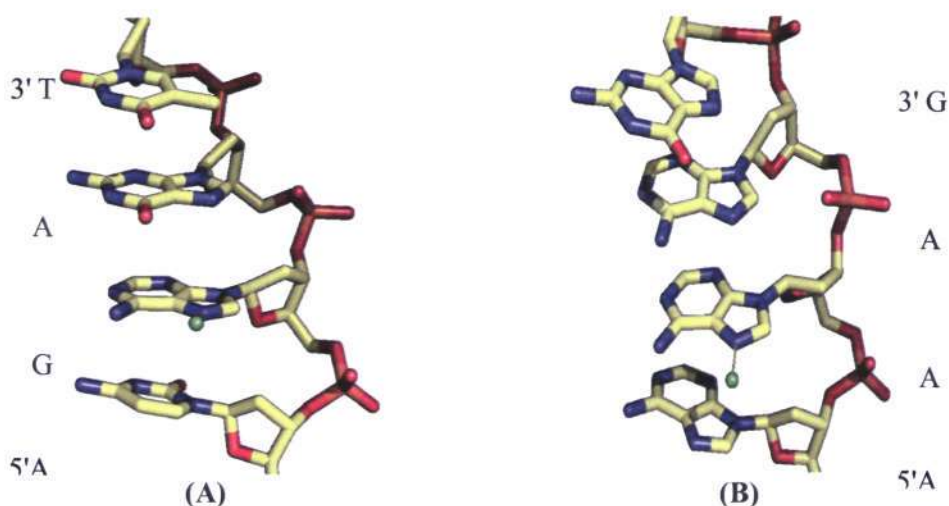


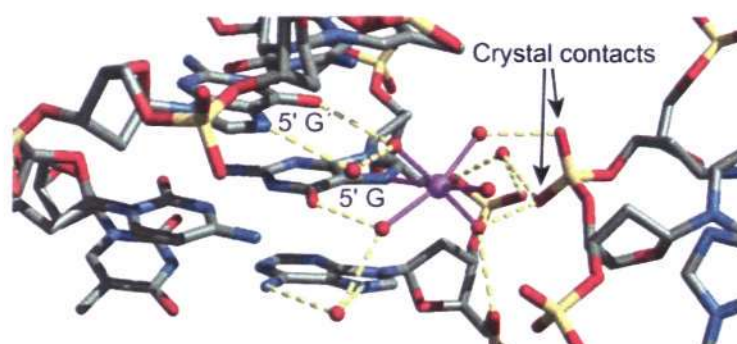
Figure 44. Ni^{2+} binding to adenine base. (A) Structure showing the tetra-nucleotide 5'-CAGT-3' where Ni^{2+} prefers to bind to adenine over guanine. (B) Structure showing the tetra-nucleotide 5'-AAAG-3' where nickel ion binds to an adenine base.

Results

Based on distances and observed interactions, we gather that GA, GT, AG and AA base steps form a three-bond mode of binding with Ni^{2+} in the major groove of NCP-DNA. Such a variety of metal-binding base steps has not been previously reported. This suggests that in addition to unique conformation of the nucleosomal DNA, which is strikingly different from naked DNA, properties of a specific heavy metal determine the binding selectivity to chromatin.

4.2.12. Ni^{2+} mediated crystal contact site in NCP-DNA

The DNA crystal contact site (27/J) is a key binding site, where metal ions form a bridge between the guanine base of 5'-AGCT-3' and a neighboring phosphate group via the metal-coordinated water molecules serving as hydrogen bond donors to the acceptor groups of phosphate. This interaction is apparently crucial for crystal packing stability. At this site, both Ni^{2+} and Mn^{2+} are bound in the respective structures. The anomalous signal peak and the occupancy of the Ni^{2+} is greater than in the other half of the NCP molecule (26/I chain), which contains the Ni^{2+} that is not bound to the neighboring NCP molecule and whose anomalous signal and occupancy is comparatively lesser. This indicates that the conformation of the tetra-nucleotide favors the binding of metal atom, but the crystal contact site is essential for proper crystal packing (Fig. 45). This type of metal-mediated networking interaction might be significant for compaction of nucleosomes into a higher-order structure and for stabilization of the chromatin fiber. Previous work shows that concentration and ion types are the contributors for chromatin compaction (Widom 1986; Clark and Kimura 1990; Blank and Becker 1995; Schwarz *et al.* 1996;). During the first stage of mitosis, there is major influx of divalent cations (Ca^{2+} , Mg^{2+}) occurs (Strick *et al.* 2001). The compaction process corresponds to crossing an energy barrier to go from a stable (interphasic) to a metastable (metaphasic and gaped) state.



Results

Figure 45. Inter-particle DNA contact site. In the contact site, 5-GC makes a crosslink to the adjacent NCP via a Mn^{2+} . Additional interactions occur between the metal-coordinated water molecules and phosphate oxygen atoms. The figure is adapted from Davey and Richmond (2002).

4.2.13. Tetra-nucleotide binding features of Ni^{2+}

The DNA sequence of NCP has 4 different types of tetra-nucleotides which have GG dinucleotide in its center (AGGT, TGGT, TGGA and AGGC). All the tetra-nucleotides are present twice in the NCP-DNA, with an exception of TGGA which occurs 8 times. Both AGGT and TGGT were found to be occupied by Mn^{2+} as well as by Ni^{2+} , whereas TGGA tetra-nucleotide elements had only half of the possible sites bound by Mn^{2+} , while seven sites were occupied by Ni^{2+} , in the respective crystal structures. In contrast, neither Mn^{2+} nor Ni^{2+} were binding to AGGC tetra-nucleotide. This is due to conformational change of DNA which impedes the cation binding to the major groove of NCP-DNA (Fig. 46).

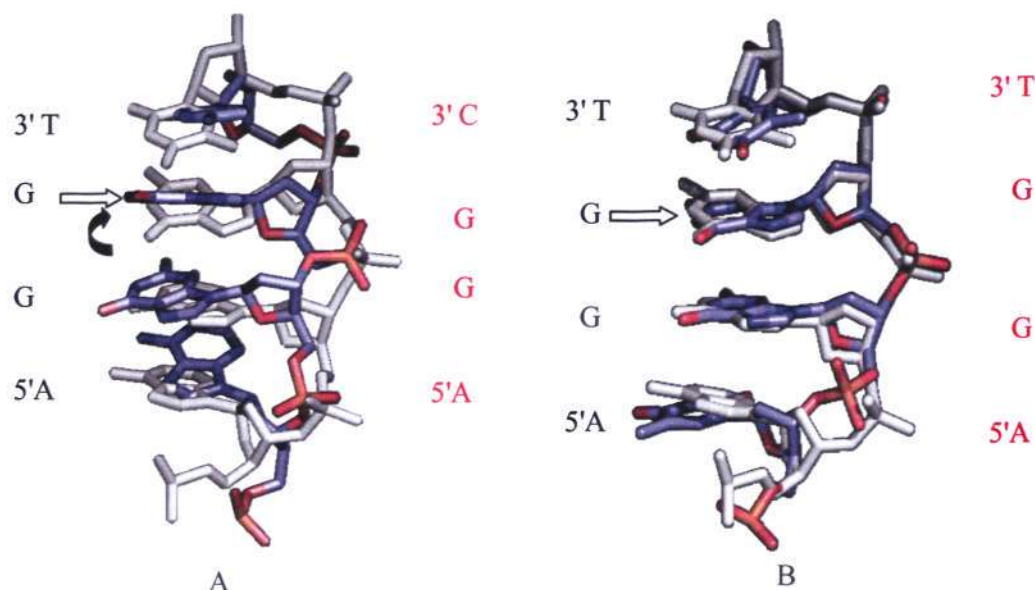


Figure 46. Structural Comparison between the two tetra-nucleotides (5'-AGGC-3' and 5'-AGGT-3') and (5'-TGGT-3' and 5'-AGGT-3'). Least squares superposition showed the difference in conformation of the tetra-nucleotides. (A) 5'-AGGC-3' (multi-colored) compared with 5'-AGGT-3' (grey), where in the former tetra-nucleotide the 3' guanine conformation is altered, likely hindering the binding of Ni^{2+} . (B) Both of the tetra-nucleotides bind Ni^{2+} [5'-TGGT-3' (multi-colored) compared with 5'-

Results

AGGT-3' (grey)] and their conformations are highly similar at GG dinucleotide base step.

Based on the analysis, Ni^{2+} appears to bind to any tetra-nucleotide with a GG step in its center, as long as it is allowed by its conformation, demonstrating that Ni^{2+} has strong affinity for DNA. This is potentially detrimental *in vivo*, causing DNA disruptions, which may lead to cancer (Salnikow and Zhitkovich 2008). In the following section, the preference of Ni^{2+} for GG dinucleotides is discussed in further detail.

4.2.14. Di-nucleotide binding features of nickel ions

In NCP147, there are 14 GG dinucleotides, and out of these, 11 are occupied by Ni^{2+} , which binds directly to one of the guanine bases. In the high resolution structure of Mn^{2+} -NCP147, only eight sites had Mn^{2+} bound at the GG step, showing apparently greater specificity of Mn^{2+} towards the nucleosomal DNA. However, Ni^{2+} being a softer metal, has much stronger affinity for the aromatic N7 atom of guanine bases of DNA, as observed from the current structure as well as from the oligonucleotide DNA crystal structures with Ni^{2+} (Abresica *et al.* 1999), where all the guanine bases were occupied by Ni^{2+} , with one case where a single Ni^{2+} was forming coordinate bonds with two guanine N7 atoms. Therefore, only major structural differences like that for the tetra-nucleotide 5'-AGGC-3' impede the binding of Ni^{2+} in the major groove of NCP.

4.2.15. Four-bond mode Ni^{2+} binding in Ni^{2+} -NCP DNA

Only two of the four-bond mode interactions found for Mn^{2+} were observed for Ni^{2+} . Ni^{2+} was observed at -35I/-34J sites, whereas for Mn^{2+} , there were two additional (4 total) sites present at 5/I - 5/J. At the 5/I - 5/J sites, Ni^{2+} formed a three-bond interaction instead of four (discussed in next section). At -35I/-34J, where Ni^{2+} binds via the four-bond mode, an additional Ni^{2+} was bound to the consecutive guanine base, -34I/-33J, forming a three-bond interaction, which was not observed in the high resolution Mn^{2+} structure (Davey and Richmond 2002). Furthermore, this is seen only with 5'-TGGA-3' tetra-nucleotides (Fig. 47). The combined occupancy values for the two metal ions were less than one (Table-4). This indicates that the two Ni^{2+} may not be binding to the consecutive nucleotides simultaneously, especially that the distances between the two

Results

Ni^{2+} at these sites, in the respective halves, are 3.41 Å and 4.52 Å, which would make a concurrent presence mutually exclusive. Perhaps the affinity for these two neighboring sites is very close, resulting in partial occupancy.

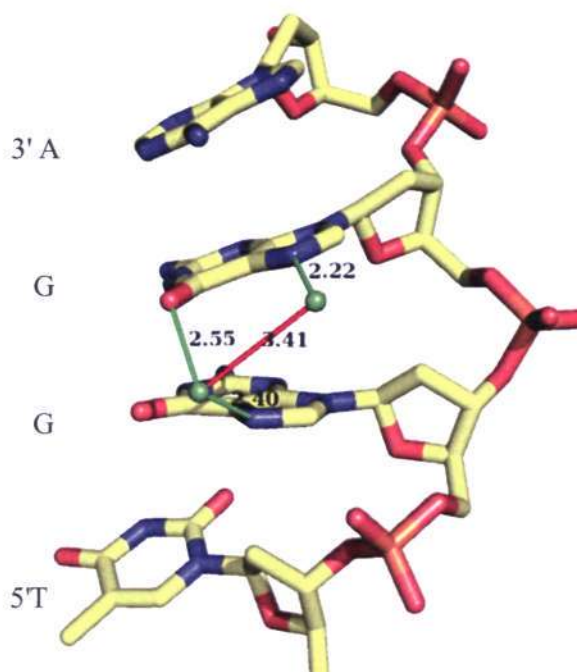


Figure 47. Tetra-nucleotide, with two different Ni^{2+} binding directly to the GG nucleotide. The occupancy values are less than one and hence the two Ni^{2+} may not be binding to the consecutive nucleotides simultaneously.

4.2.16. Three-bond mode Ni^{2+} binding in Ni^{2+} -NCP DNA

The two 5 I/J sites in the high resolution Mn^{2+} -NCP structure bind Mn^{2+} via the four-bond mode by having a direct interaction with the O6 atom of the guanine base. In the Ni^{2+} -NCP structure, only one site is occupied by Ni^{2+} (5/J) while the corresponding location in the other half empty. Moreover, Ni^{2+} makes a direct contact with the N7 atom of guanine, forming a three-bond mode instead of a four-bond mode (Fig. 48A). Most likely the presence of Ni^{2+} in the neighboring strand of the DNA (-6/I) and the opposing half (-6/J) contribute to this occurrence (Table 3). The conformational change in the DNA at this site (Fig 48 B) was only minor, which we confirmed by the superposition of tetra-nucleotides from the high resolution structure with Mn^{2+} .

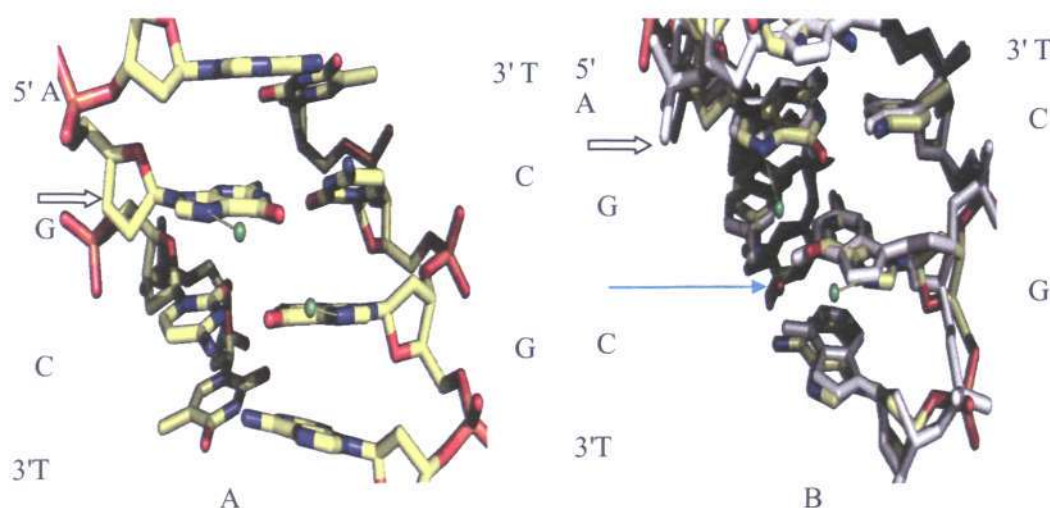


Figure 48. Four-bond mode interactions. (A) In double-stranded tetra-nucleotide DNA (AGCT), Ni^{2+} forms a direct contact with the N7 (5'/J and -6/I) atoms of guanine bases in both of the strands. This interaction likely hindered the Ni^{2+} from forming a four-bond mode at this site. (B) The same double stranded tetra-nucleotide DNA (AGCT) from the Ni^{2+} structure (multi-colored) superposed with the Mn^{2+} structure (grey color) showed no major conformational changes, but the Mn^{2+} atom (red colored sphere) preferred to form a direct bond with the O6 atom of guanine instead of N7. This resulted in the formation of a four-bond interaction at this site. Thus, the location of additional Ni^{2+} as well as their preferred mode of coordination determines binding preference.

4.2.17. Ni^{2+} binding in the minor groove of NCP

Nickel ions found at two sites in the minor groove of the NCP-DNA, whereas Mn^{2+} was identified only at one site (in the respective structure), which was different from the ones occupied by Ni^{2+} . In this location, the Mn^{2+} maintains its full octahedral hydration shell while being bound at the surface of the minor groove. Three water ligands of the Mn^{2+} interact with the H2B α C-helix coming from an adjacent NCP in the crystal (Fig. 49A). The other three water ligands aid in creating an extensive network with acceptor grooves of adenine, thymine and guanine bases, as well as deoxyribose O4' atoms. Mn^{2+} was not found at the symmetry-related sites in the other particle half, which is not juxtaposed with a nearby NCP. These inter-nucleosomal histone–cation–DNA interactions, as observed from the manganese data (Bin and Davey 2010), are relevant in the process of chromatin compaction. The histone N-terminal tails are necessary for full compaction chromatin fiber, elevated Mg^{2+} concentrations can partially compensate for their absence, indicating

Results

some overlap in how the two species types mediate nucleosome–nucleosome interactions. The tails are observed to induce compaction by forming internucleosomal DNA cross-links in molecular dynamics simulation studies. In crystals, the tails bind variably to intraparticle minor groove sites, and they snake over and between neighboring core particles, frequently engaged in remote minor groove interactions. Basic side chains of the tails in general, but especially arginine side chains in particular, are well suited to bind within narrowed minor groove elements. Thus, the tails apparently mediate the same types of nonspecific minor groove interactions whether they bind on the inside or outside of the DNA supergroove or form internucleosomal contacts (Bin and Davey 2010). Chromatin compaction with divalent cations was also suggested by sedimentation analysis of oligonucleosomes (Schwarz *et al.* 1996).

In the minor groove, Ni^{2+} were present at two sites of NCP; one at 64/I and the other at 69/I (Table-3). In both of the locations, we did not observe the coordinated water molecules of nickel ions due to moderate resolution, but the anomalous signal from these sites was sufficiently convincing (Table-3). Based on the distance, we inferred that it binds to the cytosine base (-64/J) and the sugar molecule via its coordinated water molecules, and also it can coordinate with the neighboring phosphate atom of 26/J through its water ligands, forming an inter-particle contact (Fig. 49B).

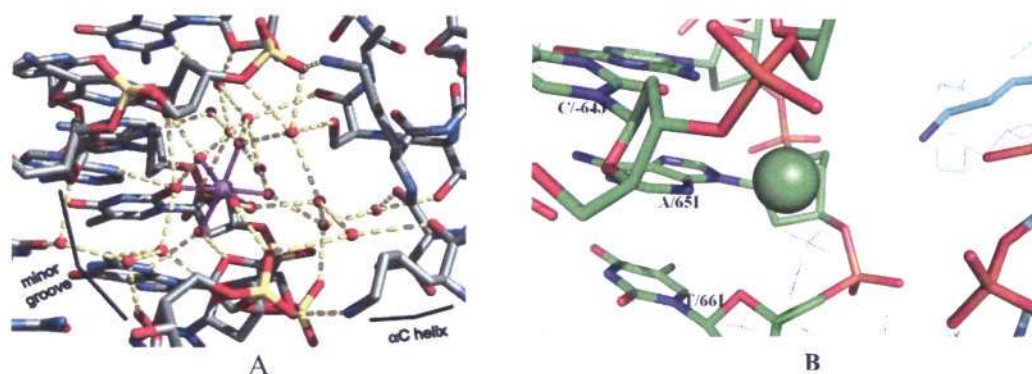


Figure 49. Metal binding in the minor groove of NCP. (A) Mn^{2+} was found at only one site in the minor groove of NCP. This metal ion was fully hydrated and interacted through its water ligands with the neighboring NCP (The figure is adapted from Davey and Richmond, 2002). (B) Ni^{2+} was observed at two sites in the minor groove of NCP. Ni^{2+} was found inside the pocket of the minor groove of NCP (-64/J) forming contacts with the neighboring NCP.

Results

4.2.18. Ni^{2+} binding to histone proteins

Ni^{2+} were observed binding to histone proteins in several locations. In contrast, Mn^{2+} was observed only at one site in the high resolution Mn^{2+} -NCP147 structure (absent in the other symmetry related half). This involved an inter-particle site displaying perfect octahedral geometry, with coordination to a carboxylate oxygen atom of ASP77-H3 and a coordinate bond with the peptide carbonyl oxygen atom of Val45-H2B from a neighboring NCP. Similarly, nickel atom was also observed at this position forming contacts with both Asp77-H3 and with the adjacent NCP atom from Val 45-H2B. This appears quite critical as it is located at the midpoint on the C terminus of the H2B- α 1 helix, providing excellent electrostatic stabilization from the helix dipole.

Table 5 - Protein binding sites of Ni^{2+} in the NCP

Site (A)	Anomalous signal	Occupancy	B-factor	Remark
1)ASP77E/H3'-VAL45D/H2B	23.6	1.00	48	Inter-particle site
2)HIS106D/H2B - HIS18F/H4	9.6	0.72	98	Inter-particle site
3)HIS79D/H2B	6.2	0.41	61	-
4) HIS79H/H2B'	8.6	0.31	49	-
5)HIS106/H2B'	7.1	0.47	79	-
6)ASP90C/H2A	4.3	0.29	49	-

(A) The histone amino acids highlighted in light blue are from the neighboring NCP molecule, involved in the formation of inter-particle contacts.

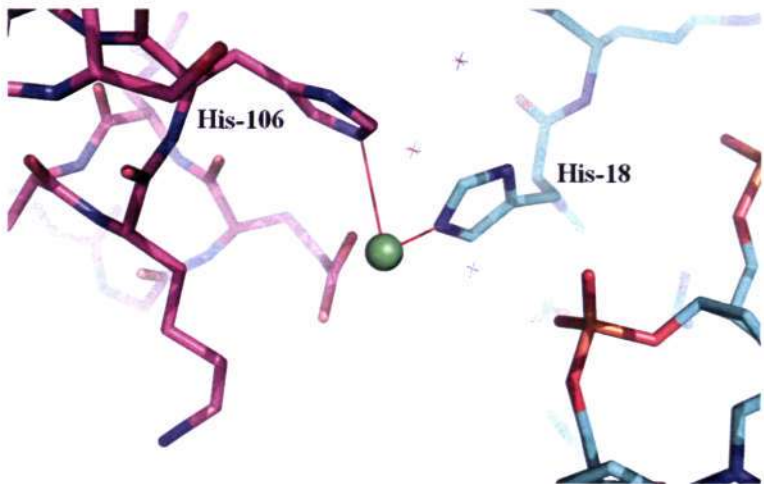


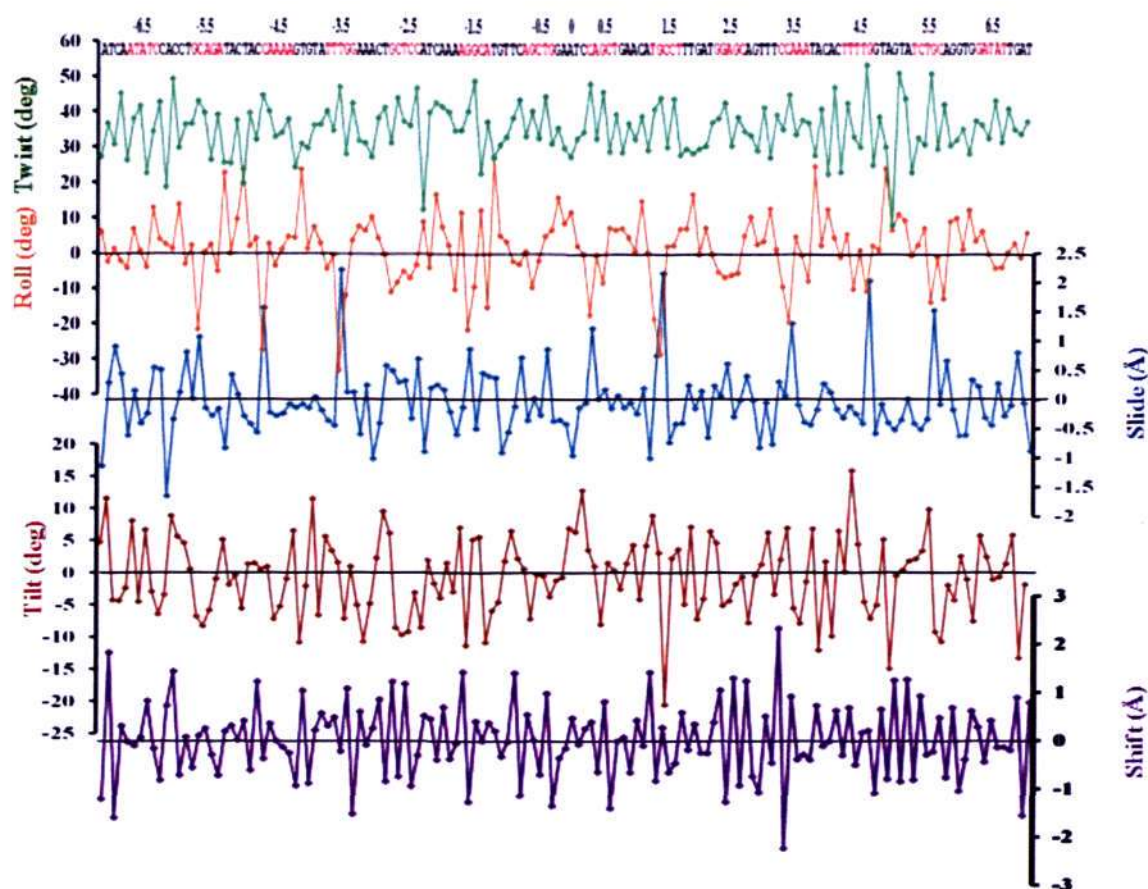
Figure 50. Binding of Ni^{2+} to histidine residues at the inter-particle site. Inter-particle interaction between Ni^{2+} and histidine residues His18/H4 (cyan-multicolor) and His106/H2B (magenta-multicolor) of the neighboring NCP.

Results

As mentioned, Ni^{2+} was observed at several locations and more importantly, it formed an additional inter-particle interaction via histidine. Ni^{2+} formed a direct bond with the nitrogen atom (NE2) of histidine (His18/H4'-chain F) and with the adjacent nitrogen atom (NE2) of histidine (His106/ H2B-chain D). However, in the symmetry-related half, nickel atom was not observed (Fig. 50). Binding of Ni^{2+} to histidine (His18/H4') could potentially result in changes to acetylation of the lysine residues (discussed in detail in the Discussion section). Furthermore, Ni^{2+} interacted with the nitrogen atom (NE2) of histidine of H2B protein (Table-5).

4.2.19. Geometric parameters of DNA in Ni^{2+} -NCP structure

The conformational parameters for the DNA in the NCP were calculated using the program CURVES (Lavery and Sklenar 1988). We analyzed the global base pair parameters and obtained the geometric parameter values such as roll, slide, shift, tilt and twist in order to show the effect of nickel ion on DNA base steps (Table-4). The global base pair values for the entire DNA of the NCP are shown in figure 51.



Results

Figure 51. DNA geometric parameters for Ni^{2+} -NCP. The graph shows the global base pair parameters of the NCP-DNA147 of Ni^{2+} data calculated using CURVES software.

4.3. Crystallographic characterization of Co^{2+} binding to NCP

In order to structurally characterize the binding of Co^{2+} to NCP, we followed a strategy similar to that mentioned for Ni^{2+} . For the most part, results were very similar for both nickel and cobalt ions. Therefore, in this section, we focus on differences between the two.

When NCP was crystallized in the presence of CoCl_2 , instead of MnCl_2 , the resulting crystals were of similar size and shape as those grown in Mn^{2+} . However, crystals started to degrade in about 2 weeks after they first appeared. Moreover, they diffracted poorly and the pattern appeared anisotropic. Since the maximum resolution reached at the synchrotron was only 5 Å, we decided to pursue the strategy of Mn-crystallization followed by buffer exchange, which we developed for Ni^{2+} . We obtained comparatively better diffracting crystals using 37 mM cobalt chloride (same concentration as that of nickel chloride). These crystals diffracted to 2.6 Å resolution at the SLS synchrotron, using X-rays tuned to the cobalt absorption edge. The crystallographic statistics are mentioned in the table 6.

Moreover, same strategy as that for Ni^{2+} was applied in order to get accurate occupancy and B-factor values for Co^{2+} . In order to get accurate values for metal thermal factors (B-factors) and occupancies, we used the program *mlphare* in the CCP4 suite. This program aided in the accurate determination of atomic parameters based on the anomalous difference signal of the heavy atom (Cobalt). Multiple cycles of *mlphare* were applied until the independently refined B-factors and occupancies converged. The anomalous occupancy values are initially on an arbitrary scale. These were subsequently normalized with respect to the known fully occupied divalent metal binding site, which mediates a histone-histone interparticle contact in the crystal (Davey et al., 2002; Table 7 [ATOM1]).

Results

Table 6. Crystallographic statistics for Co²⁺-NCP

Space group	<i>P</i> 2 ₁ 2 ₁ 2 ₁
Unit cell dimensions (Å)	
<i>a</i>	106.50
<i>b</i>	109.94
<i>c</i>	183.35
Resolution range (Å)	2.6-52.63
Unique reflections	65267
Redundancy (last shell)	5.1 (2.8)
Completeness (%) (last shell)	97.7 (86.5)
<i>I</i> / σ	13.6 (2.2)
<i>R</i> _{merge} (last shell)	0.065 (0.332)
<i>R</i> _{factor}	0.249
<i>R</i> _{free}	0.291
<i>R</i> _{anomalous} (overall)	0.046
Anomalous completeness %)(last shell)	92.0 (63.8)
Anomalous multiplicity %)(last shell)	2.7 (1.6)
Number of aminoacids	775
Number of Bases	292
Rmsd	
Bond (Å)	0.0075
Angles (°)	1.188
Average B-factor (Å ²)	
Protein	53.62
DNA	108.14

* Numerical values in parentheses are for the highest resolution shell.

Table 7. Occupancy and B-factors for Co²⁺ calculated using the MLPhare program

	Position	Real Bfac ligand (A)	Real Bfac Co ²⁺ (B)	Normalized Occupancy (C)	Ano Signal (D)	Cycle 6 Bfac	Cycle 6 Ano	Cycle 4 Bfac	Cycle 4 Ano	Cycle 3 Bfac	Cycle 3 Ano	Cycle 2 Bfac (E)	Cycle 2 Ano (F)
	ATOM1	77ASP/E	44.83	52.24	1	26.4	109.20	2.97	109.54	2.99	110.03	3.00	3.00
	ATOM2	60GD/I	93.07	64.24	0.6	15.7	133.02	1.78	127.23	1.69	119.87	1.58	1.58
	ATOM3	27GD/J	84.89	60.66	0.66	14.8	119.76	1.95	118.47	1.93	115.93	1.88	1.88
	ATOM4	61GD/J	106.08	66.49	0.75	14.2	119.78	2.23	117.76	2.20	114.81	2.14	2.14
	ATOM5	48GD/J	91.92	58.29	0.48	12.6	103.95	1.41	105.34	1.44	107.60	1.47	1.47
	ATOM6	47GD/I	93.58	66.66	0.51	11.6	105.67	1.52	106.76	1.54	108.71	1.56	1.56
	ATOM7	3GD/J	72.96	57.26	0.57	11.3	145.15	1.69	137.08	1.58	125.79	1.42	1.42
	ATOM8	26GD/I	80.27	52.54	0.47	10.6	112.01	1.41	112.11	1.41	111.93	1.42	1.42
	ATOM9	35GD/I	90.21	75.38	0.54	9.9	131.61	1.60	126.49	1.54	119.26	1.45	1.45
	ATOM10	6GD/J	88.48	63.83	0.45	9.2	147.98	1.35	139.30	1.27	127.50	1.15	1.15
	ATOM11	3GD/I	85.62	72.39	0.61	9.2	148.89	1.80	139.03	1.68	126.20	1.52	1.52
	ATOM12	18HIS/F	93.96	78.7	0.52	8.8	134.37	1.55	129.24	1.48	121.47	1.39	1.39
	ATOM13	79HIS/H	63.03	45.7	0.21	7.8	86.38	0.63	90.09	0.66	97.03	0.71	0.71
	ATOM14	34GD/J	93.33	84.32	0.49	7.8	161.91	1.44	148.91	1.32	132.11	1.15	1.15
	ATOM15	56GD/I	113.58	82.88	0.48	7.6	176.07	1.43	158.06	1.26	135.30	1.05	1.05
	ATOM16	106HIS/H	60.92	77.18	0.33	7.2	120.84	0.97	118.00	0.95	114.45	0.92	0.92
	ATOM17	8GD/J	82.66	68.83	0.46	7.2	149.75	1.38	139.85	1.27	126.39	1.13	1.13
	ATOM18	45GD/J	110.59	97.89	0.43	6.7	136.13	1.28	130.93	1.22	123.11	1.13	1.13
	ATOM19	29AD/J	98.2	56.64	0.28	6.2	142.46	0.84	134.11	0.79	124.30	0.73	0.73
	ATOM20	52GD/J	131.82	83.67	0.39	5.9	182.63	1.17	163.90	1.01	139.68	0.82	0.82
	ATOM21	71GD/J	90.83	82.24	0.32	5.7	162.46	0.95	150.71	0.87	134.43	0.76	0.76
	ATOM22	58GD/J	107.49	63	0.23	5.7	121.39	0.68	120.13	0.67	117.05	0.64	0.64
	ATOM23	464CD/I	130.2	64.83	0.25	5.5	170.82	0.73	154.31	0.66	133.94	0.57	0.57
	ATOM24	28AD/I	88.22	48	0.19	5.3	105.69	0.58	107.30	0.60	108.95	0.62	0.62
	ATOM25	70GD/I	88.71	63.69	0.23	5.3	130.99	0.67	126.76	0.65	120.26	0.62	0.62
	ATOM26	64GD/I	103.36	52.78	0.3	5	133.48	0.89	128.36	0.86	121.18	0.81	0.81
	ATOM27	79HIS/D	65.93	39.76	0.21	4.9	106.41	0.63	107.24	0.63	108.58	0.63	0.63
	ATOM28	5GD/J	107.57	76.86	0.26	4.9	196.86	0.78	170.78	0.67	141.20	0.54	0.54
	ATOM29	23GD/I	110.1	69.55	0.22	4.9	101.77	0.64	102.89	0.65	105.24	0.66	0.66
	ATOM30	33GD/J	91.8	54.04	0.19	4.9	129.63	0.55	127.86	0.55	121.70	0.52	0.52
	ATOM31	64GD/J	135.02	65.54	0.39	4.6	155.51	1.15	144.26	1.05	128.90	0.93	0.93
	ATOM32	25GD/I	116.26	57.23	0.2	4.5	146.62	0.59	136.55	0.55	123.10	0.49	0.49
	ATOM33	57GD/I	88.82	79.08	0.19	4.4	199.08	0.58	179.55	0.50	151.15	0.40	0.40
	Average		94.07	66.13									

(D) Peak heights observed in the anomalous difference map. The highest signal was found for a histone site at 26.4σ. 4σ was set as the minimum value for introducing metal ions into the model. (F) The anomalous occupancy values were refined using the Mlphare program, with each cycle consisting of 30 rounds of refinement. In the first cycle, only occupancy was refined, and in the subsequent cycle only the (E) B-factor was refined. Anomalous occupancy and B-factor were alternately refined until both converged, which occurred in the 6th cycle. (C) Occupancy values were normalized with respect to the highest converged value. (B) Rcal B-factor values were obtained by applying the normalized anomalous occupancy values to refinement using the Refmac program. (A) B-factor values of the ligand atom to which nickel ion was bound in the NCP structure.

Table 8. Co²⁺ sites in the DNA of NCP

Site (A)	Location bp (B) I/J chain	Sequence 5'-3' (C)	Bond distance (Å) I/J chain (D)	Anomalous Signal (σ) I/J chain	Occupancy I/J chain	Average occupancy	B-factor (Å ²) I/J chain	Mode of binding	Roll ° (E)	Shift (Å)	Slide (Å)	Slide at 5' TG, (Å)	5' N7-3' O6 distance (Å)
1-GG	60/61	AGGT	2.1/2.3 N	15.7/14.2	0.6/0.75	0.675	64/66	3-bond	10.89	-0.85	-0.25	-	3.97
2-GG	47/48	TGCT	2.1/2.4 N	11.6/12.6	0.51/0.48	0.495	67/58	3-bond	-9.01	-0.48	0.68	0.97	4.09
3-GG	-3/-3	TGGA	2/2.6 N	9.2/11.3	0.61/0.57	0.590	72/57	3-bond	-5.11	-0.12	0.44	0.47	3.97
4-GG	-35/-34	TGGA	2.6/2.5 N	9.9/7.8	0.54/0.49	0.515	75/84	4-bond	-6.65	0.76	0.88	0.60	3.37
			2.6/2.3 O	-	-	-	-	-	-	-	-	-	-
5-GC	26/27	AGCA	2.2/2.5 N	10.6/14.8	0.47/0.66	0.565	53/61	3-bond	-2.66	-1.24	-0.12	-	-
6-GC	-/5	AGCT	-/2.3 O	-/4.9	-/0.26	0.130	0/77	4-bond	-1.78	-0.65	0.13	-	-
7-GC	-/14	TGCC	-	-	-	-	-	-	-	-	-	-	-
8-GG	64/-	TGCA	2.5 N	5/-	0.3/0.51	0.405	53/0	3-bond	4.74	-0.38	-0.17	-	-
9-GA	-56/-55	AGAT	2.3/2.5 N	7.6/6.7	0.48/0.43	0.455	83/98	3-bond	4.27	-0.77	-0.46	-	-
10-GC	-6/-6	AGCT	-/2.4 N	-/9.2	-/0.45	0.275	0/64	3-bond	5.92	-1.15	-0.17	-	-
11-GA	-/8	TGAA	-/2.3 N	-/7.2	-/0.46	0.23	0/69	3-bond	-16.3	-0.96	0.97	-	-
12-GG	-34/-33	TGCA	-/2 N	-/4.9	-/0.19	0.095	0/54	3-bond	-8.72	-1.62	0.31	-	-
13-GG	-/64	TGGA	-/2.5 N	-/4.6	-/0.39	0.195	0/66	3-bond	2.69	-0.81	0.67	-0.85	4.54
14-AG	28/29	CAGT	2.2/2.6 N	5.3/6.2	0.19/0.28	0.235	48/57	3-bond	4.82	-1.37	0.15	-	-
15-GT	51/52	AGTA	-/2.5 O	-/5.9	-/0.39	0.195	0/84	3-bond	8.15	-0.12	0.28	-	-
16-GA	70/71	TGAT	2/2 N	5.3/5.7	0.23/0.32	0.275	64/82	3-bond	5.47	-0.81	0.26	0.42	-
17-GC	-/58	TGCA	-/2.6 N	-/5.2	-/0.23	0.115	0/63	3-bond	-12.09	-0.45	0.85	0.04	-
18-GG	23/-	TGGA	2.6/- N	4.9/-	0.22/-	0.110	70/0	3-bond	-4.91	1.33	-0.19	0.81	3.69
19-GG	-/25	TGGA	-/2.6 N	-/4.5	-/0.2	0.100	0/57	3-bond	0.59	-1.28	-0.31	-	-
20-GC	57/-	TGCA	2.6/- N	4.4/-	0.19/-	0.095	79/0	3-bond	-1.01	-0.36	0.36	1.76	-
21-AA	-/18	AAG	-	-	-	-	-	-	-	-	-	-	-
22-sg	64	GGA	-	5.5	0.25	0.125	65	Minor grv.	-	-	-	-	-
23-sg	69	TTG	-	-	-	-	-	Minor grv.	-	-	-	-	-
24-sg	13	ATG	-	-	-	-	-	-	-	-	-	-	-

(A) Co²⁺ binding sites. All sites are in the DNA major groove except for 22-sg, 23-sg and 24-sg in the minor groove. GG, GC, GA, GT, and AG denote the type of base step to which the Co²⁺ is binding. Mn²⁺ binding sites are occupied by Co²⁺ are denoted by **gray background**. Co²⁺ binding sites, not occupied by Ni²⁺ are represented in **green**, while Ni²⁺ binding sites, not occupied by Co²⁺ are colored **red**. (B) Distance in base pairs from the site of the central base pair (bp 0) on the molecular dyad axis. Chain "I" runs from base pair-73 at the 5' terminus to +72 at the 3' terminus, whereas Chain "J" runs from base pair +72 at the 5' terminus to -73 at the 3' terminus. Although 147-bp DNA is 2-fold sequence symmetric about bp 0, but due to the single base pair missing, it is renumbered to 146X version of 147. (C) Dinucleotide step defining Co²⁺ binding sites in the major groove are underlined. Direct binding of Co²⁺ to a base highlighted in blue. (D) Bond distance from metal center to the N7 and O6 ligands of DNA atom. The two values correspond to the two halves of the DNA superhelix. (E) Parameter values are the average for two base steps, one from the identical sequence in each half of the DNA superhelix. DNA geometrical parameters are defined in (Dickerson 1989). Since certain sites were not occupied by Co²⁺ in both of the halves, thus, parameter value is derived based on single site.

Results

Table 9 - Protein binding sites of Co²⁺ in the NCP

Site (A)	Anomalous signal	Occupancy	B-factor	Remark
1)ASP77E/H3'-VAL45D/H2B	26.4	1.00	48	Inter-particle site
2)HIS18F/H4- HIS106D/H2B	8.8	0.52	79	Inter-particle site
3)HIS79D/H2B	5	0.21	40	-
4) HIS79H/H2B'	7.8	0.21	49	-
5)HIS106/H2B'	7.2	0.33	77	-
6)ASP90C/H2A	-	-	-	-

(A) The histone amino acids highlighted in light blue are from the neighboring NCP molecule involved in the formation of inter-particle site. Amino acids highlighted in red are not bound to Co²⁺ whereas Ni²⁺ bound to this residue.

4.3.1. Similarities between Co²⁺ and Ni²⁺ binding to NCP

In general, binding of Co²⁺ to the NCP crystal was similar to that of Ni²⁺; although subtle differences exist in cobalt data. Like Ni²⁺, Co²⁺ also had high affinity for binding to the DNA. It was found interacting at 28 sites. Co²⁺ was binding to guanine and adenine bases at the various base steps (GG, GC, GA, GT and AG) similar to Ni²⁺. Co²⁺ also displayed preference for GG steps over other base steps. Most of the Co²⁺ binding occurred in the major groove of the DNA which again is the case for other divalent metals. The mode of bond formation was similar to Ni²⁺; however, the four-bond mode occurred at three sites as compared to two sites in Ni²⁺-NCP (Table-6). In the minor groove of NCP, Co²⁺ was located only at one site (64/I) forming analogous interactions as those of nickel (Table-7). As far as interactions with histone proteins, cobalt was observed at five locations, comparable to Ni²⁺ (Table-8). The DNA of Co²⁺-NCP structure displayed a histone-register shift similar to that of Ni²⁺-NCP.

4.3.2. Differences between Co²⁺ and Ni²⁺ binding to NCP

The major difference between Co²⁺ and Ni²⁺ binding to the NCP is in the number of ions interacting with the NCP, which for Ni²⁺ was 38, while it is 33 for Co²⁺. Most of these changes were observed within the DNA of the NCP. In a few places where nickel atoms were present in both halves of NCP, Co²⁺ were not observed; especially the three sites on the chain “I” (Table -7). At -6 bp (10-GC) of chain I in the dyad region of the NCP no Co²⁺ was observed, while the other half of the DNA (-6bp of “J” chain) contained one. The other two locations were at -34/I (12-GG) and 51/I bp (15-GT). Co²⁺

Results

was not observed at the -6/I site, although metal binding occurs here in the Ni^{2+} structure. Binding at this site may be precluded by Co^{2+} binding at 5/J and forming a direct bond with the O6 atom instead of N7 atom (as is in case for Ni^{2+}), allowing for a four-bond mode such as that seen for Mn^{2+} (Davey and Richmond 2002). Hence, the coordination geometry of one ion in the context of the local DNA conformation may determine the binding of the neighboring ions to the NCP-DNA (Fig. 52).

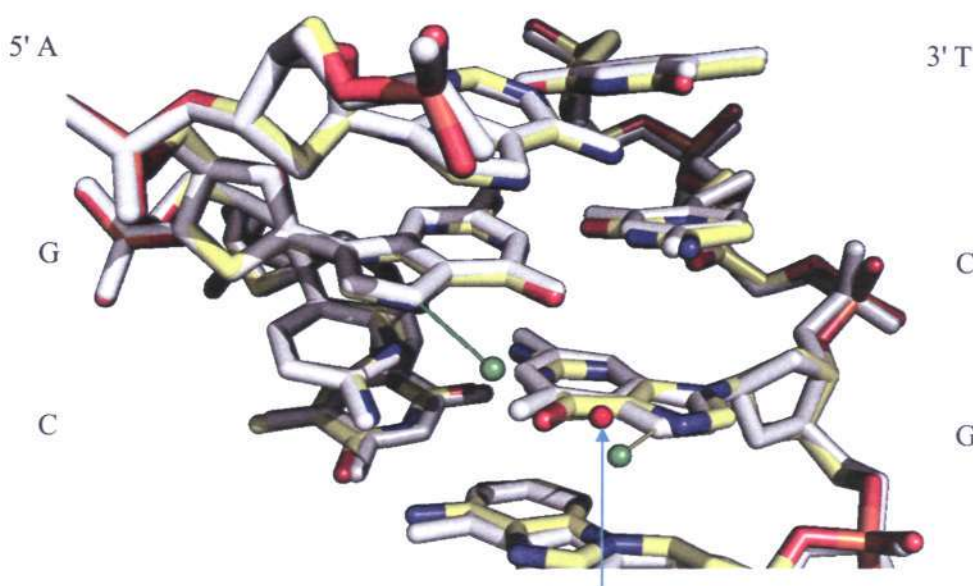


Figure 52. Four-bond mode site in Co^{2+} -NCP DNA. When we superposed the double stranded tetra-nucleotide DNA 5'-AGCT-3' (5/J and -6/I) of Ni^{2+} data (grey color) with that of Co^{2+} (multi-color), we did not observe any noticeable conformational changes, but Co^{2+} (red color) formed a direct bond with the O6 atom of guanine resulting in the four-bond mode, which was similar to that of Mn^{2+} . Whereas in the case of Ni^{2+} (green color), metals formed direct bonds with the N7 atoms of guanine bases in both of the strands. This interaction would not allow Ni^{2+} to form a four-bond mode at this site. Thus the position of the ion and manner of DNA attack determine the mode of interaction.

On the other hand, two extra sites where Co^{2+} were observed at 25/J and -58/J, which were not occupied by Ni^{2+} . The site 25/J was a predicted metal binding site based on DNA conformation in the high resolution Mn^{2+} data. This additional Co^{2+} site and the one occupying only one half of NCP were observed in the J chain of the DNA.

Results

Similarly to Mn^{2+} , Co^{2+} was observed at one site in the minor groove of the NCP [22-small groove (sg)]. However its location was different from that of Mn^{2+} , but similar to one of the minor groove binding sites of Ni^{2+} , whereas Co^{2+} was not observed at the other site (23-sg) for Ni^{2+} . For the histone proteins, Co^{2+} occupied five sites, which is one fewer than Ni^{2+} (90ASP/C).

4.3.3. Geometric parameters of DNA in Co^{2+} -NCP structure

The overall DNA geometrical parameters of the Co^{2+} -bound DNA in NCP, which were calculated by the program CURVES, were similar to those of nickel. We analyzed the global base pair parameters (Fig 53) deriving values such as roll, slide, shift, tilt and twist in order to assess the effects of Co^{2+} on DNA base steps (Table-8).

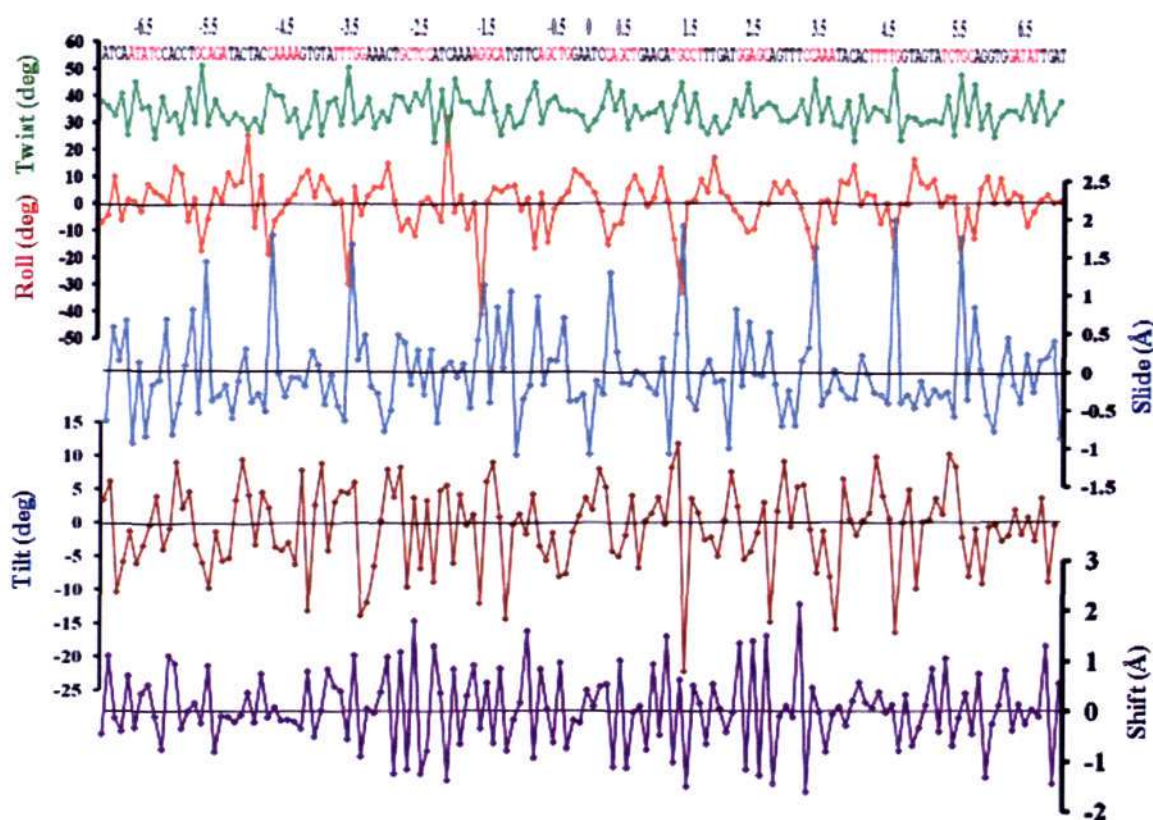


Figure 53. DNA geometric parameters for Co^{2+} -NCP. Graph shows the global base pair parameters of the Co^{2+} -NCP-DNA147, calculated using CURVES software.

Results

In summary, Ni^{2+} and Co^{2+} have the capability of sliding the DNA of NCP in the crystalline state by inducing a stretch at the -2SHL region, which results in the shifting of the DNA by one base pair from -2SHL to +2 SHL. Moreover, these metals show higher affinity of binding to both DNA and protein of the NCP. The binding nature of these ions indicate that they have a very strong preferences for the N7 atom of guanine and wherever a favorable conformation of the DNA exists, these ions tend to bind the guanine with diminished importance of the electrostatic favorably of the particular sequence element.

4.4. Crystallographic characterization of monovalent heavy metals binding to NCP

The backbone of the DNA is highly negatively charged, and thus it is strongly engaged in electrostatic interactions. In general, this charge is neutralized by cations in solution, or by proteins via basic amino acids. In the NCP, the negative charge of the DNA is partly neutralized by the side chains of basic amino acids from the histone proteins. All previous monovalent heavy atom binding studies were done with naked DNA (Mirzabekov and Rich 1979; Rouzina and Bloomfield 1998; Denisov and Halle 2000), rather than with nucleosomes. We examined whether any sequence-dependent association exists between NCP and monovalent cations. In the minor groove of DNA, water molecules act as a bridge between the bases from the two opposite strands of the DNA by forming hydrogen bonds between N3 of adenine and the O2 atoms of thymine residues. Nevertheless, it is difficult to differentiate between monovalent Na^+ and water molecules in the electron density map. Such ions are present frequently in crystallization buffers, and they are important elements of the eukaryotic nucleus. Therefore, it is important to understand the role of monovalent ions in the context of nucleosomal DNA binding.

Confirming the identity of the lighter monovalent (Na^+ and K^+) ions in an X-ray structure is quite problematic, even with ultra high resolution structural data. Moreover, it is very challenging to obtain such high resolution NCP data due to its inherent characteristics such as high B-factor, solvent content and molecular weight, as well as DNA sliding. Therefore, we decided to study the interaction of heavy monovalent metal ions, such as Rb^+ and Cs^+ , with the NCP147.

NCP147 crystals were harvested as mentioned in the **Materials and Methods** section 3.5, followed by buffer exchange in a step-wise fashion (as described for nickel chloride) with rubidium chloride and rubidium cacodylate (pH 6.0) in order to remove all of the KCl and K-cacodylate, maintaining the original concentration of Mn^{2+} . The same buffer exchange strategy was followed in the case of cesium chloride-treated NCP147 crystals, wherein cesium chloride and cesium cacodylate (pH 6.0) were used.

Rubidium chloride-treated NCP147 crystal data was collected at the SLS (Swiss light source, Villigen, Switzerland). The wavelength used for diffraction was 0.8146 Å, which is the absorption edge for rubidium. Rubidium treated-NCP147 crystals diffracted

Results

up to 2.55 Å. The structure was solved using the NCP147 model with Mn²⁺. Crystallographic statistics are summarized in table 10.

Table 10. Crystallographic statistics for Rb⁺-NCP

Space group	<i>P</i> 2 ₁ 2 ₁ 2 ₁
Unit cell dimensions (Å)	
<i>a</i>	106.46
<i>b</i>	109.68
<i>c</i>	182.21
Resolution range (Å)	2.55-94
Unique reflections	69593
Redundancy (last shell)	7.2 (6.1)
Completeness (%) (last shell)	99.2 (95)
I/σ	25.2 (6.6)
Rmerge (last shell)	0.046 (0.284)
Rfactor	0.243
Rfree	0.275
Number of aminoacids	774
Number of Bases	294
Rmsd	
Bond (Å)	0.007
Angles (°)	1.146
Average B-factor (Å ²)	
Protein	37.5
DNA	81

**Numerical values in parentheses are for the highest resolution shell.*

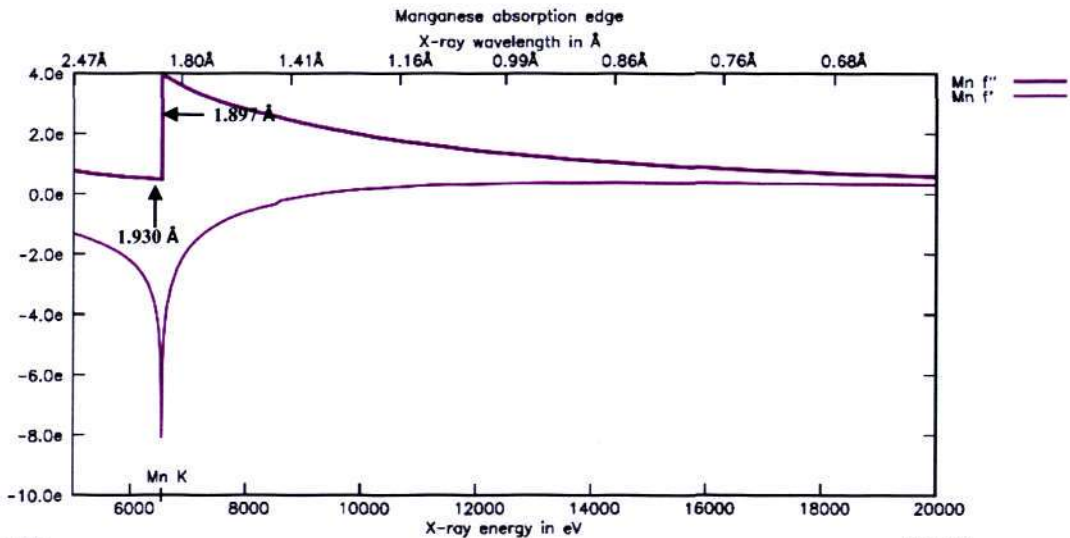
In the case of cesium chloride, data were collected at a wavelength of 1.93 Å, which is the inflection point of Mn²⁺ (Fig 54). Since this wavelength falls in the soft X-ray category, it reduced the intensity of diffraction and as a result our NCP crystals diffracted only up to 3.15 Å. The major reason why we collected the data at this wavelength was that we wanted to ensure that there are no anomalous signal contributions from Mn²⁺. The structure of cesium-treated NCP147 crystal data was solved using NCP147 with Mn²⁺.

Results

Table 11. Crystallographic statistics for Cs⁺-NCP

Space group	<i>P</i> 2 ₁ 2 ₁ 2 ₁
Unit cell dimensions (Å)	
<i>a</i>	106.51
<i>b</i>	109.66
<i>c</i>	182.60
Resolution range (Å)	3.15–94
Unique reflections	37672
Redundancy (last shell)	7.0 (5.7)
Completeness (%) (last shell)	99.8 (98.5)
<i>I</i> / σ	17.8 (3.1)
<i>R</i> _{merge} (last shell)	0.091 (0.477)
<i>R</i> _{factor}	0.217
<i>R</i> _{free}	0.255
Number of aminoacids	776
Number of Bases	294
Rmsd	
Bond (Å)	0.009
Angles (°)	1.474
Average B-factor (Å ²)	
Protein	51.25
DNA	101

*Numerical values in parentheses are for the highest resolution shell.



Results

Figure 54. Manganese absorption edge. Manganese absorption edge is shown in the figure. The peak for Mn is at 1.89 Å and data was collected at 1.93 Å for cesium NCP147. (The figure is adapted from www.bmsc.washington.edu/scatter)

From the high resolution structure of NCP (Davey *et al.* 2002), we inferred that Mn^{2+} stabilizes the major inter-particle site at 77ASP/E or H3' with the 45VAL/D or H2B of neighboring NCP. This site is essential for proper crystal packing. When we analyzed the anomalous map, we did not observe any anomalous signal for Mn^{2+} at this site, even when we contoured the map to 2σ . This indicated that any anomalous signal we identify should come from cesium ions. Based on datasets of both of the monovalents, we observed monovalent ions at two sites, which are identical for the two, as well as an additional site, which was unique for the Cs^+ (Table -12).

Table 12. Monovalent ion sites in the DNA minor groove of NCP

Metal	Site (A)	Location bp (B) I/J chain	Sequence 5'-3'	Occupancy I/J chain	B-factor (Å ²) I/J chain	Anomalous signal
Rb	1-AT	-66/-66	ATC	0.45/0.55	70/8	6.3/5.3
Cs	2-AT	-66/-66	ATC	0.29/0.52	89/112	6.9/5.6
Cs	3-TC	-26	CTC	0.46	100	6.2

(A) All the sites are in the DNA minor groove. AT and TC are the base steps where monovalent ions were bound.

(B) Distance in base pairs from the site of the central base pair (bp 0) on the molecular dyad axis. Chain "I" runs from base pair -73 at the 5' terminus to +73 at the 3' terminus, whereas Chain "J" runs from base pair +73 at the 5' terminus to -73 at the 3' terminus. 147-bp DNA sequence is symmetric about bp 0.

4.4.1. Monovalent metals in the minor groove DNA of NCP

The new crystallographic data of NCP147 reveals for the first time the binding of monovalent heavy atoms Rb^+ and Cs^+ to the minor groove of the NCP. These ions were found in deep pockets of the minor grooves, especially in A/T-rich tracts. Due to moderate resolution of these structures we were not able to identify the neighboring water molecules. As observed previously using X-ray, NMR and molecular mechanics results suggest that binding of these monovalent ions may help stabilize narrowing of the minor groove (McFail-Isom *et al.*, 1999). These heavy alkali metal ions seem to have partial

Results

occupancy and are capable of replacing a water molecule that links the keto-oxygens of thymines from opposite strands. Rb^+ were observed at two sites in the minor groove, which occurred in both halves of the NCP (Table-12). Similar kinds of interactions were observed for the Cs^+ -treated NCP crystal (Fig. 55A), with an extra Cs^+ ion observed at -26T/I present only in one half, which is also a narrow minor groove element. This ion formed an intra-strand interaction with the O2 atoms of thymine and cytosine (Fig. 55B). This type of interaction was not observed in the case of rubidium. This is consistent with a the previous study on naked DNA (Tereshko *et al.* 1999). There were 15 possible AT dinucleotide steps present in the DNA147 and only two sites were occupied by these ions. The binding of these ions at two sites (each half of the palindromic DNA) indicates that the sequence and conformation of the DNA dictates the binding of monovalent ions in the minor groove of NCP.

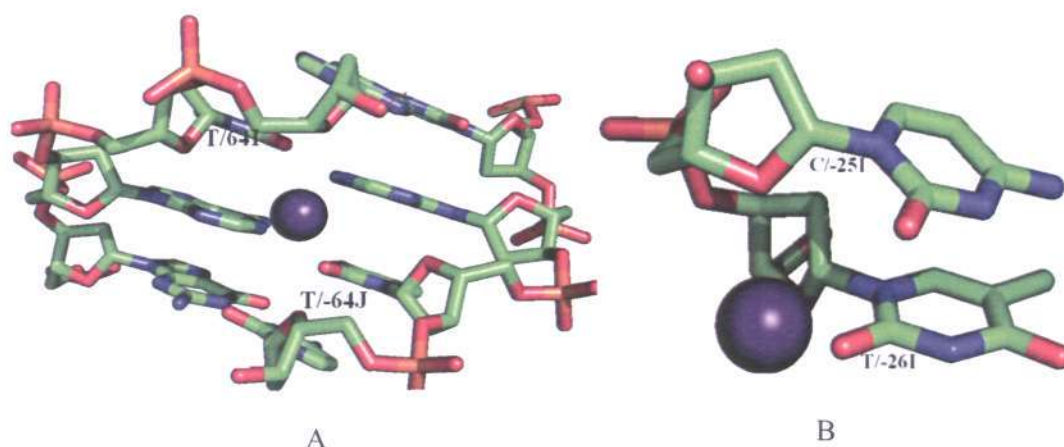
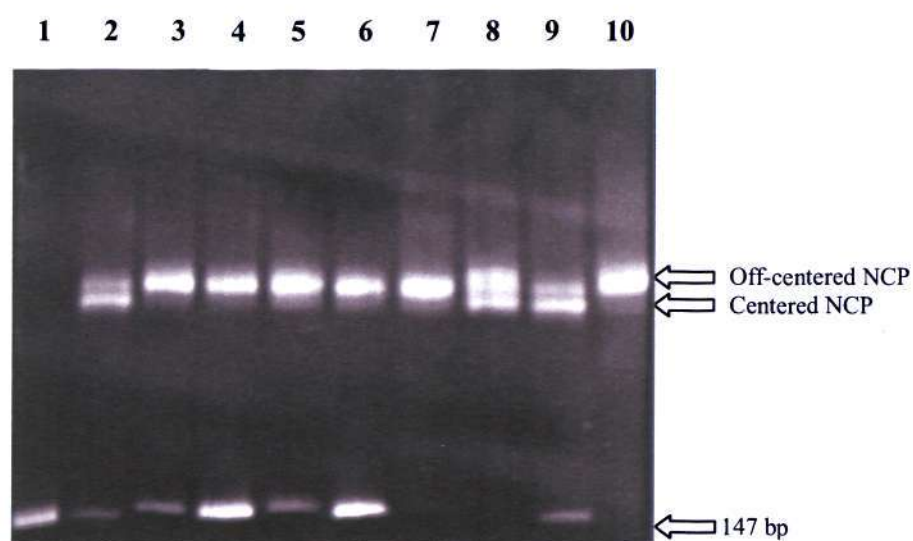


Figure 55. Cs^+ in the minor groove of NCP. (A) Cs^+ is observed at AT-tract in the minor groove of NCP147. (B) Cs^+ was found in between thymine and cytosine bases forming an intra-strand linkage.

5. NEW DNA SEQUENCES (147*) AND THEIR SEQUENCE CONFORMATION-RELATIONSHIPS IN NCP

To date, all the solved nucleosome core particle structures contained only palindromic DNA, with exception of one, in which the DNA was modified from the palindromic DNA, just by introducing a 16 bp Poly (dA.dT) element. These NCP crystals diffracted poorly due mixed orientation of the DNA and poor lattice formation (Bao *et al.* 2006). We were interested in structurally characterizing a non-palindromic DNA of NCP. Our designer sequence (Fig. 25) was also originally modified from the palindromic DNA, substituting 54 bp of the original sequence.

We used three different designer DNAs in our study: Des1, Des 2 and Des3 (Fig. 25). Designer DNA after reconstitution with HO gave the respective designer-NCP and was analyzed on an EMSA gel (Fig. 56). The majority of the designer NCP turned out to be off-centered (Luger *et al.* 1999), even after heating at 50 °C for 1 hour, except for Des 3, where ~40 % of the NCP was centered (Lane 8). We used various ratios of HO to DNA in order to assess whether a limiting concentration of DNA would not result in the majority of the NCP being off-centered. However, changing HO:DNA ratio did not appear to make any difference (Shown for Des 1 in this EMSA gel).



Results

Figure 56. EMSA of reconstituted designer NCP: Reconstituted Designer NCPs were analyzed by 5% DNA PAGE gel in 0.25X TBE buffer. Lane 1 – 147 bp DNA; Lane 2 – P α 32S -NCP (1 μ g); Lane 3 – Des 1 NCP (2 μ g), HO/DNA Ratio 0.6/1; Lane 4 – Des 1 NCP (2 μ g), HO/DNA Ratio 0.4/1; Lane 5 – Des 1 NCP (2 μ g), HO/DNA Ratio 0.6/1 Δ at 50°C for 1 hr; Lane 6 – Des 1 NCP (2 μ g), HO/DNA Ratio 0.4/1 Δ at 50°C for 1 hr; Lane 7 – Des 2 NCP(2 μ g), HO/DNA Ratio 0.6/1 Δ at 50°C for 1 hr; Lane 8 – Des 3 NCP (2 μ g), HO/DNA Ratio 0.6/1 Δ at 50°C for 1 hr; Lane 9 – P α 32S-NCP (1 μ g); Lane 10 – Des 3 NCP (2 μ g), HO/DNA Ratio 0.6/1 not Δ .

5.1. Designer 2 NCP crystallization

Concentrated designer NCP (8 mg/ml) in 20 mM K-Cacodylate (pH-6.0) buffer was used for crystallization. Initially, we tried the same condition as that for standard NCP (having 147 bp palindromic human α -satellite DNA) crystallizations; *i.e.* 85 mM MnCl₂, 60 mM KCl and 20 mM K-Cacodylate (pH-6.0). However, the designer crystals obtained under these conditions were thin, small and highly twinned. Standard NCP147 crystals usually appear within 5 days, in contrast to 2 weeks required for the designer crystals. A drop size of 4 μ l (initial) was used for screening. A comparison of the crystal morphologies for standard NCP147 and designer NCP147 can be seen in the figure 57. These designer crystals diffracted very poorly with a resolution of \sim 25 Å (Fig. 58).

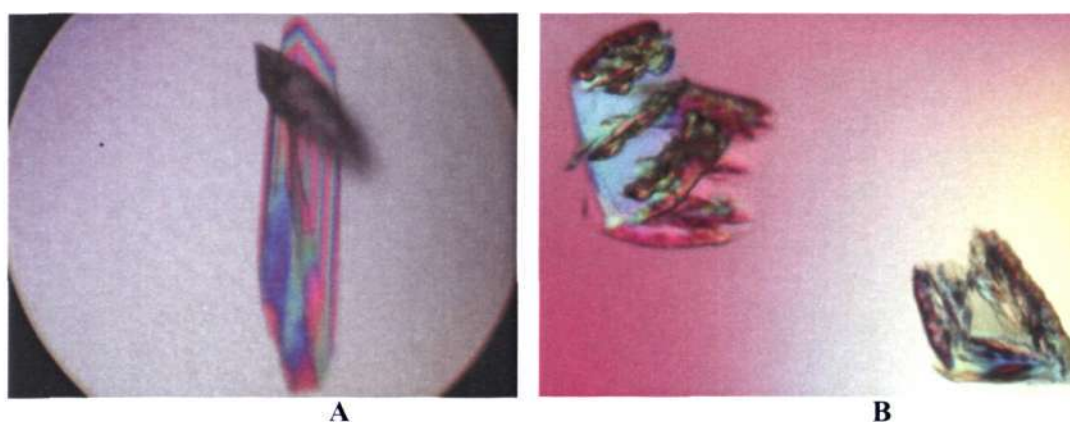


Figure 57. Crystals of NCP grown in MnCl₂ condition. (A) Standard NCP147 crystals **(B)** Des 2 NCP crystals under the same conditions.

Results

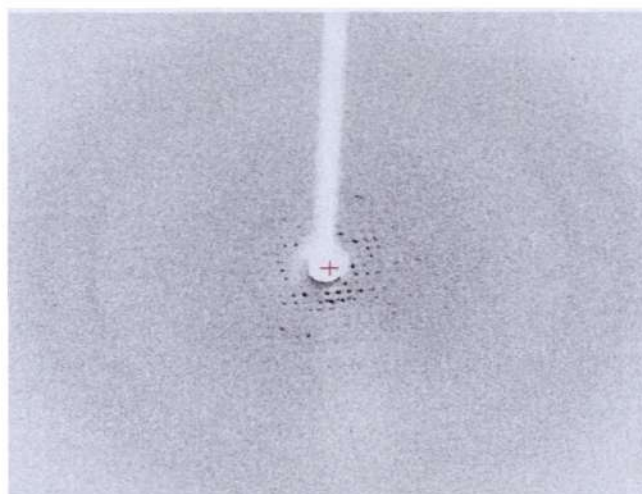


Figure 58. Diffraction pattern of des 2 NCP grown in $MnCl_2$ conditions.
Des 2 crystals grown in $MnCl_2$ buffer gave very poor diffraction.

Utilizing the standard NCP crystallization condition as a starting point, we have attempted an additive screening using the additive Kit from Hampton Research. A majority of the additives did not yield better crystals, except for 2-methyl-2, 4-pentenediol (MPD) which is a known DNA precipitant and suitable NCP crystal dehydrating agent. The presence of MPD was found to improve crystal morphology and the crystallization process became faster, wherein crystals appeared within a week. But the size of the crystal was small compared to the crystals grown in the original conditions and the diffraction quality was even worse.

From our experience with other metal binding studies, we knew that incorporation of mercuric chloride can improve NCP crystal morphology. Thus, in addition to 12 % MPD, we incorporated 2 mM mercuric chloride in our crystallization condition. We got crystals with a relatively lower degree of twinning. Although of better shape, crystals were still thin (Fig. 59A). These designer crystals yielded moderate resolution ~ 6 Å, the diffraction was anisotropic and the intensity of the spots was also weak (Fig. 59B).

Results

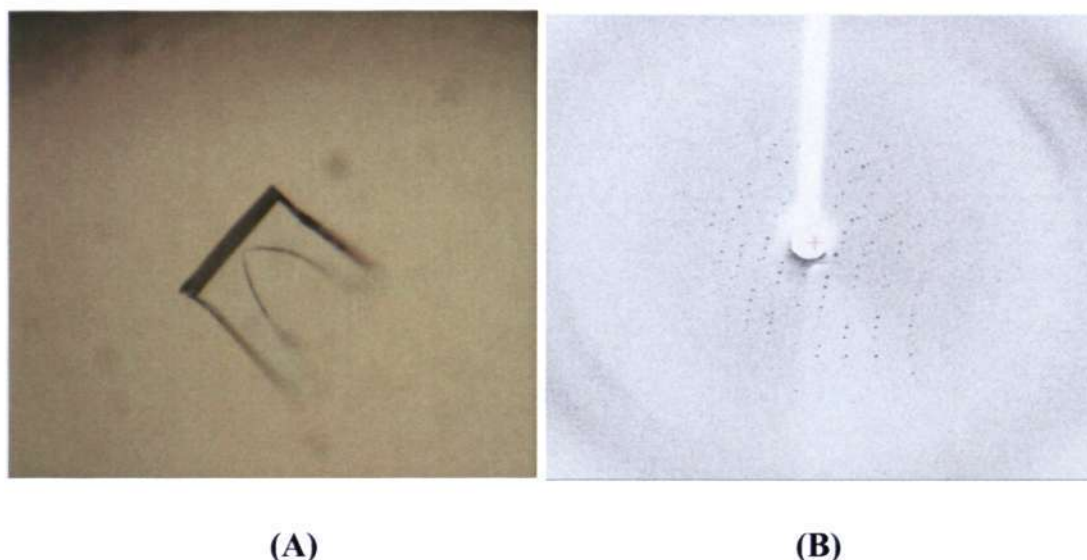


Figure 59. *Crystal of des 2 NCP grown in $MnCl_2$, MPD and $HgCl_2$.* (A) Des 2 NCP was crystallized in a buffer containing Manganese chloride, MPD and Mercuric chloride. (B) The corresponding crystal diffraction pattern.

In order to get crystals without twinning and with better resolution, we performed an additive fine screen of MPD and mercuric chloride conditions. Inclusion of additives such as spermine tetrachloride and β -octyl glucoside gave moderate sized crystals without twinning. Maintaining the same concentration of MPD (*i.e.* 12%) in the drop as well as in the reservoir proved helpful in the improvement of the crystal size (Fig. 60), although it required longer periods of time (two and a half months).



Results

Figure 60. Final des 2 NCP crystals: Des 2 NCP147 was crystallized in a buffer containing 85 mM MnCl_2 , 60 mM KCl, 20 mM K-Cacodylate (pH 6.0) 12% MPD (same concentration in both drop and reservoir), 2 mM Mercuric chloride, 2 mM Spermine tetrachloride and 0.5% β -octyl glucoside. The reservoir contained 0.5X of the above components with the exception of MPD.

5.2. Designer 2 NCP crystal harvesting and data collection

Desinger 2 crystals were harvested in a buffer containing 37 mM MnCl_2 , 40 mM KCl, 20 mM potassium cacodylate (pH 6.0), 12% MPD, 2 mM HgCl_2 , 2 mM Spermine tetrachloride and 0.5% β -octyl glucoside, which was followed by gradually increasing MPD concentration from 12% to 24% in steps of 4%. In the final step, 2% trehalose was also introduced. Harvested NCP crystals were maintained in this final buffer for 3 hours to overnight for stabilization and to avoid loss of quality that might affect diffraction limits.

These crystals still diffracted anisotropically, but the resolution limit was improved up to ~ 3.5 Å on in-house equipment. Afterwards, Des 2 crystal data were collected from the synchrotron (SLS) at an X-ray wavelength of 1.0 Å. The diffraction limit was further increased to 3.05 Å (Fig. 61). The unit cell parameters and the space group were quite similar compared to the palindromic NCP147.

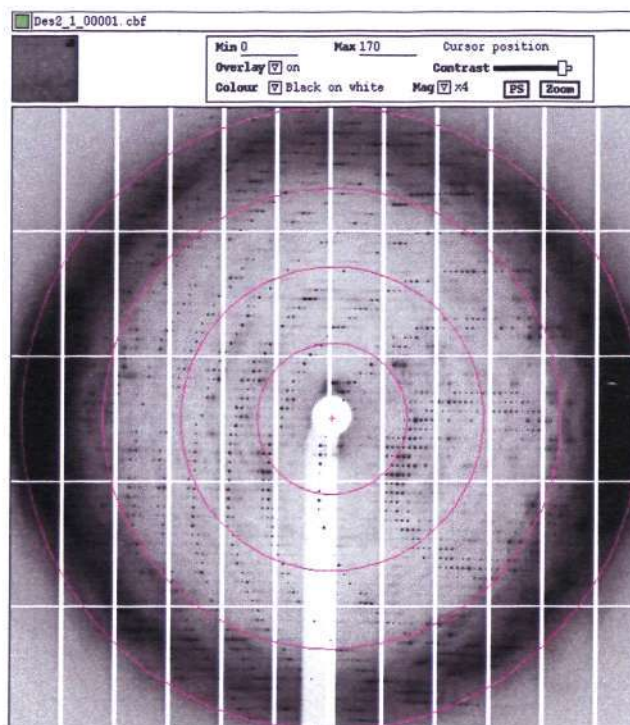


Figure 61. Diffraction pattern of des 2 NCP crystal. Des 2 crystals were grown in manganese chloride buffer along with other additives. The Des 2 crystals diffracted up to ~ 3.05 Å at the synchrotron.

Table 13.Crystallographic statistics for des 2 NCP

Space group	<i>P</i> 2 ₁ 2 ₁ 2 ₁
Unit cell dimensions (Å)	
<i>a</i>	106.38
<i>b</i>	109.59
<i>c</i>	179.90
Resolution range (Å)	3.05–60
Unique reflections	38701
Redundancy (last shell)	5.7 (5.6)
Completeness (%) (last shell)	95.2 (76.6)
<i>I</i> /σ	24.5 (3.0)
<i>R</i> _{merge} (last shell)	0.056 (0.483)
<i>R</i> _{factor}	0.257
<i>R</i> _{free}	0.330
Number of aminoacids	761
Number of Bases	294
Rmsd	
Bond (Å)	0.008
Angles (°)	1.353
Average B-factor (Å ²)	
Protein	103
DNA	181

**Numerical values in parentheses are for the highest resolution shell*

5.3. Structure of des 2 NCP

The overall structure of designer NCP was similar to that of NCP147 with palindromic DNA. The relatively low resolution and high B-factors that characterized the DNA in this particular structure posed limits to the extent of analysis that can be

Results

conducted for the DNA. In the difference map, a Hg^{2+} peak was observed at two sites; one near the cysteine residues of H3 and H3' and the other at 46/histidine of H2B'. Manganese ions were observed at eight locations; one at the predominant protein inter-particle contact site and the rest associated with the DNA and its backbone. The overall packing of the DNA was similar to that of palindromic NCP147. Designer NCP crystals had higher thermal factors for both DNA and histone proteins. This was probably the reason for relatively moderate diffraction quality of these crystals. Such high thermal factors were previously reported for the Poly(dA.dT) NCP structure at 3.2 Å resolution (Bao *et al.* 2006).

5.3.1. Orientation of DNA in des 2 NCP

Due to moderate resolution, it was difficult to see the orientation of DNA in the structure. This was a potential problem due to the asymmetric DNA in NCP, because the two halves of the DNA could lead to a mixture of orientations in the lattice. Ideally, all NCP molecules should crystallize in the same orientation throughout the crystal lattice, but that did not happen. In order to find out the preferred orientation, we tried orienting the DNA in both directions, followed by refinement using Refmac. The overall maps were similar in both the orientations and so we chose the free *R*-values as our guidance, which were 0.330 and 0.344. Also, we refined both the DNA orientation with partial occupancy and this model gave higher free *R* value. Therefore, we picked the model with the lower free *R*-value as our most accurate model.

5.3.2. DNA end stacking in des 2 NCP

Based on the structure, we presumed that one major reason for poor resolution was improper DNA end stacking, based on the fact that the ends of des 2 DNA were highly distorted on both the sides of NCP and they were not forming a proper Watson-Crick base pair (Fig. 62). In addition, there was a large gap between the ends of neighboring NCP particles. This result in inadequate end stacking that affects the overall stability of the DNA in the NCP and also diminishes the lattice stabilization, which is indispensable for proper crystal packing. The observed gap appeared to be able to accommodate one more base pair at both ends. We inferred that the addition of such a

Results

base pair to the NCP would potentially improve stacking of the DNA, which in turn could assist the lattice stabilization of overall DNA structure in the NCP and yield a better diffraction quality for the crystals.

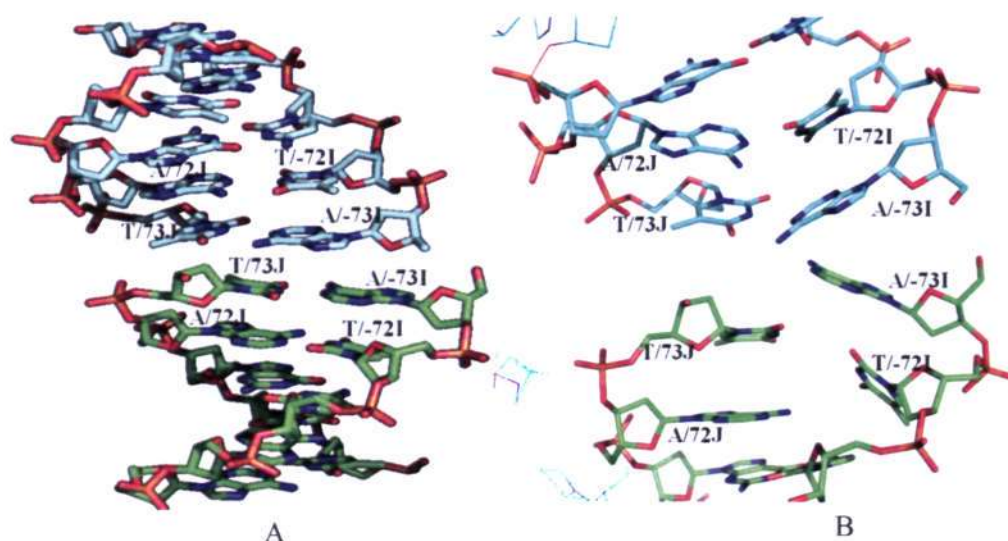


Figure 62. NCP DNA termini: (A) NCP147 palindromic DNA termini were stacked tightly, which helped in the overall stabilization of the DNA (for clarity only the ends are shown). (B) Des 2 DNA termini ends were disoriented. There was a gap for an additional base pair, which if added could potentially aid the stabilization of DNA.

5.3.3. Minor groove narrowing at TA region of des 2 NCP

In spite of the limiting resolution, important conclusions could be drawn from a superposition of the des 2 NCP147 with palindromic NCP147. The two refined structures were found to superimpose with an average root mean square deviation (rmsd) of 0.67 Å for proteins and 1.68 Å for DNA. Overall, there was no significant difference between the two models. In particular, the des 2 DNA conforms moderately to the DNA topology typical for nucleosomal DNA. In the DNA of des 2 NCP, there were four TA elements which face the minor groove of the NCP. These TA elements were present near the dyad ± 0.5 and ± 1.5 SHL regions. The electron density maps in this region revealed that DNA is highly twisted. Moreover, the TA elements in the ± 1.5 SHL region had a very narrow minor groove when compared with NCP147 (Fig. 63). When we inspected the structure carefully we observed that the minor groove of des 2 is narrowed in several TA rich

Results

regions. In another oligonucleotide structure (Alexeev *et al.* 1987) and the structure of poly(dA·dT) NCP (Bao *et al.* 2006), a similar feature was observed. We calculated the minor groove widths using 3DNA software (Lu and Olson 2003) and the quantitative analysis (Fig. 63) revealed that the overall widths of the des 2 DNA were similar to those of the palindromic 147 bp DNA, except for significant shifts at ± 1.5 , +5 and +6.

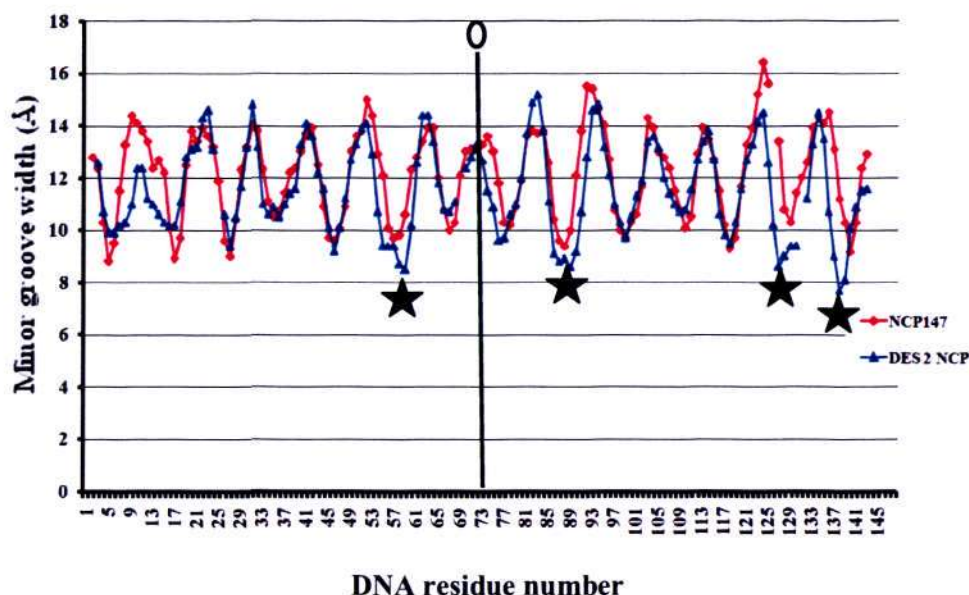


Figure 63. Minor groove width data: Minor groove widths of des 2 NCP147 were calculated by using 3DNA software. Minor grooves were much narrower at the TA elements. “0” indicate the central dyad base pair. Asterisks indicate the narrower minor grooves. For a few bp steps, groove parameters could not be calculated by the program and can be seen as a gap.

5.3.4. High thermal factors for des 2 NCP

One of the significant features of this structure was the relatively high temperature factors over the entire length of the DNA, which can absorb significant amount of noise and systematic error, while indicating a higher degree of static or dynamic disorder than previously observed for the canonical α -satellite NCP147 structure. This phenomenon was observed in another slightly non-palindromic DNA sequence, the Poly(dA·dT) NCP (Bao *et al.* 2006) as well, which might be the expected state for asymmetric nucleosomal DNA, as opposed to what has been observed for the palindromic NCP147 structure. Furthermore, to a certain degree, a combination of mixed DNA orientations in the NCP

Results

could also be a contributing factor to high *B*-factor values in these structures. Since a modified DNA sequence was used in the present study, in which the TA sequence elements were grafted on to a strong positioning sequence, one must be cautious while speculating about the effect of these sequence elements on *in vivo* chromatin structure.

5.3.5. Cation binding to the DNA of des 2 NCP

For the des 2 NCP, Mn^{2+} were found to bind to the DNA at seven sites, out of which 4 sites were the same as in the NCP147 and the other 3 sites were new and involved in inter-particle interactions (Table-14). Sites which were similar as in the palindromic 147 DNA formed the same interactions with Mn^{2+} and were found in the major grooves of the NCP having a direct bond with the N7 atom of a guanine base. A continuous section of 56 base pairs (5'-73 to -18 3') of one half of the des 2 NCP was sequence-identical to that of NCP147 (Fig. 25). In this section, there were 4 possible sites where Mn^{2+} could bind [61, 48, 27 (opposite strand) and -35 bp], but the ions were observed only at 2 sites (48 and 27 bp). We presume that this was mainly due to local conformation changes of the DNA that did not favor Mn^{2+} binding, which resulted from the distinct DNA sequence.

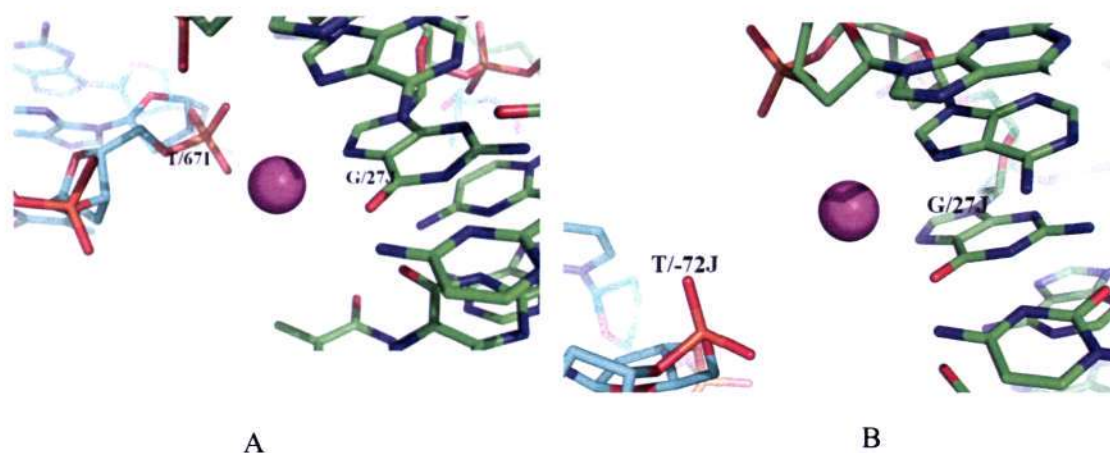


Figure 64. DNA inter-particle site: (A) NCP147 DNA inter-particle site, where Mn^{2+} forms a bond with N7 atom of guanine base of 27 bp from the dyad region and also with the DNA backbone (seventh base pair from the termini) of neighboring NCP (B) In Des 2 NCP, a similar inter-particle interaction was observed except that Mn^{2+} interacted with the second base

Results

pair from the termini of the adjacent NCP, which aided in denser packing of NCP in the crystal.

In NCP147 and in the related constructs, such as NCP146 and NCP145, Mn^{2+} forms an important inter-particle interaction via its coordinated water molecules with the DNA (67T/I) backbone of adjacent NCP, the seventh base pair from the termini (Fig. 64A), whereas for NCP146b the inter particle DNA-DNA contact occurs at the third base pair from the termini of adjacent NCP particle. A four base pair alteration in particle-particle register between NCP147 and NCP146b resulted in significantly closer packing of the two particles paired by terminal stackers, which gave rise to a more dense packing configuration in the NCP146b crystal. In the des 2 structure we observed a similar kind of inter-particle interaction at the same site. The major difference we observed was that the metal ion interacted with the DNA backbone of the second base pair from the terminus of a neighboring NCP (Fig. 64B). A shift in one base pair near the termini as compared to NCP146b appears to cause the disordered DNA termini of des 2 NCP. Besides, the distance between guanine to the phosphate backbone of the adjacent NCP is more than 9 Å, which is too long for a strong metal-mediated interaction. Thus, differences in conformation and metal-binding configuration between the two asymmetric halves reduce lattice ordering.

Among the other three new sites where Mn^{2+} were observed to form the inter-particle interactions, two sites involved DNA-metal-protein interactions and one DNA-metal-DNA interaction (Table-11). Altogether, there were five metal mediated inter-particle interactions in des 2 NCP147, while only three in the case of NCP147. These metal mediated inter-particle interactions might have favored proper crystal packing via compaction of NCP.

Table 14. Metal binding sites in des 2 NCP

Site (A)	Location bp (B) I/J chain	Sequence 5'-3'(C)	Occupancy I/J chain	B-factor (Å ²) I/J chain	Location in Protein	Adjacent NCP interactions
1-GG	61/61	AGGT/AGAT	-	-	-	-
2-GG	48/48	TGGT/AGGT	1/1	167/164	-	-
3-GG	-35/-35	TGGA/AGCG	-	-	-	-
4-GC/GA	27/27	AGCA/AGAA	1/1	199/210	-	Phos-72Td/J
5.DNA backbone	Phos-61Cd/J	-	1.00	197	-	GLU73A/H3
6. DNA backbone	Phos-69TdI	-	1.00	185	-	Phos 25Gd/J
7. DNA backbone	Phos-67TdI	-	1.00	180	-	ASP82A/H3
8. Protein	-	-	1.00	85	ASP77E/H3'	Val45D/H2B
9.Protein (Hg)	-	-	1.00	152	CYT110A E H3 H3'	-
10.Protein (Hg)	-	-	0.5	192	46HISH H2B	-

Results

(A) Metal binding sites. Site 2 and 4 are in the DNA major groove, which are similar sites as those in NCP147. Site 5, 6 and 7 forms the inter-particle interactions with the DNA backbone and with the adjacent NCP. “**Gray Background**” denotes the Mn^{2+} binding sites of NCP147, which are occupied by Mn^{2+} of Des 2 NCP and “**Red numbers**” denotes a Mn^{2+} binding sites of NCP147 which are not occupied in Des 2 NCP. Site 9 and 10 are Hg^{2+} binding sites of protein.

(B) Distance in base pairs from the site of the central base pair (bp 0) on the molecular dyad axis. Chain “I” runs from base pair -73 at the 5' terminus to +73 at the 3' terminus, whereas Chain “J” runs from base pair +73 at the 5' terminus to -73 at the 3' terminus. Des 2 DNA is not a 2-fold sequence symmetric about bp 0.

(C) Dinucleotide step defining Mn^{2+} binding sites in the major groove are underlined. A base which is directly binding Mn^{2+} is shown in blue.

DISCUSSION and OUTLOOK

6. DISCUSSION and OUTLOOK

6.1. Importance of manganese in NCP crystallization

In the crystallization buffer of NCP (Page.55) where Mn was replaced by Co, Ca or Mg yielded crystals. However, NCP crystals grown in Ca and Mg salts looked significantly different from those in Mn, and they were small in size giving poor diffraction of only up to ~ 7 Å. We presumed that the presence of metal similar to Mn (based on HSAB scale and co-ordination geometry, except mercury) would help in getting better NCP crystals; therefore we tried introducing the heavy metals such as Co, Ni, Cu, Cd, and Hg to the calcium and magnesium NCP crystals. All these crystals were still small and had a different shape. Even though these crystals diffracted poorly, we observed one interesting feature for the mercuric chloride co-crystallized NCP crystals; they were extremely long in the case of calcium as well as in magnesium conditions. We know that mercury ion has a very strong affinity for cysteine residues of the H3 protein. Moreover, mercury ion does not bind to DNA unless it has a T-T mismatch (Tanaka *et al.* 2006; Miyake *et al.* 2006). Based on this observation we used Hg^{2+} in the crystallization of the designer DNA of NCP, because designer DNA NCP crystals were very thin and had rough edges (Fig. 57B) when grown in native conditions. Indeed, the usage of mercury ions changed the designer NCP crystal shape drastically and also the diffraction quality improved from 25 Å to 6 Å.

In the case of Co, NCP crystals were very similar in shape and size when compared to NCP crystals grown in Mn, but they started to degrade almost two weeks after formation. This showed the deleterious effect of Co^{2+} on the DNA in NCP even when the concentration of cobalt chloride (85 mM) in the crystallization buffer was same as it would be in Mn^{2+} condition. The Co^{2+} NCP crystals were harvested before degradation, but even at the synchrotron, these crystals diffracted only to 5.5 Å and the diffraction pattern was highly anisotropic, suggesting the importance of Mn^{2+} in obtaining well diffracting crystals of NCP. Indeed, the optimal crystallization range for NCP is very narrow and limited. As a consequence, we had to resort to co-crystallization or soaking.

Discussion and Outlook

Initially, we tried soaking the crystals with the respective heavy metal of interest after harvesting the crystal, where the harvesting buffer was exchanged gradually with respective heavy metal of interest, simultaneously removing Mn^{2+} . This strategy worked more favorably for Co^{2+} and Ni^{2+} , apparently because both metals share the same coordination geometry (octahedral) with Mn^{2+} , and they have borderline softness on the Pearson hardness-softness scale, somewhat similar to manganese. Metals such as Cu, Zn and Cd introduced by soaking, as well as through co-crystallization, resulted in cracking of crystals. Their detrimental effect on the NCP crystals was most probably due to their high softness and also potentially ROS-generating potential.

6.2. Heavy metal ions and DNA binding

Previous metal binding studies with Mn, Ni, Co, and Zn ions and oligonucleotide DNA using NMR and crystallographic techniques showed that these metals have a strong preference for binding at the N7 atom of the 5' guanine, especially in the major groove of GG steps (Froystein *et al.* 1993; Moldrheim *et al.* 1998; Soler-Lopez *et al.* 2002; Valls *et al.* 2004; Millonig *et al.* 2009). Our study on Ni^{2+} and Co^{2+} confirmed this tendency. The binding of these metals to the GG base step is promoted by the electrostatic nature of these divalent nucleotides (Pullman and Pullman 1981; Travers 2004). On the other hand, the precise mode of metal coordination is largely determined by where the metal ion lies on the bonding Pearson hardness and softness scale. Mn^{2+} falls on the 'softer' hard edge of the Pearson scale, whereas Ni^{2+} and Co^{2+} fall on the border between hard and soft, thus their relative degree of softness/hardness varies significantly (Pearson 1990). These differences explain why Mn^{2+} has an affinity for the relatively soft N7 atom of guanine. On the other hand, since Ni^{2+} and Co^{2+} are much softer than Mn^{2+} , they have a very high affinity for purine N7 atoms in general, including the less electrostatically favorable adenine. The observed mode of Mn^{2+} binding to the major groove side of GG steps (Davey and Richmond 2002) in NCP structure is similar to that observed for Ni^{2+} and Co^{2+} site in the NCP. Besides, there are other GG sites which were predicted to be Mn^{2+} binding site, but Mn^{2+} were not observed at those sites, whereas Ni^{2+} and Co^{2+} were (Tables- 3 and 7), as well as a few additional sites. This clearly shows that the degree of metal softness plays a significant role in the binding to the DNA.

Discussion and Outlook

6.3. Biological significance of Ni^{2+} in carcinogenesis

Insoluble nickel compounds like nickel sulfide are very much deleterious and these compounds phagocytized into cells were shown to selectively target heterochromatin (Sen and Costa 1985). They were capable of silencing genes by inducing DNA hypermethylation. Ni^{2+} -induced DNA methylation changes were initially discovered in the Chinese hamster G12 cell line, which possess a copy of the bacterial *gpt* transgene near the telomere of chromosome 1, leading to the inactivation of gene expression (Lee *et al.* 1995). Another *in vivo* study, where nickel sulfide was injected into wild type C57BL/6 mice and mice heterozygous for the tumor suppressor p53 gene, showed remarkable changes in the DNA methylation leading to nickel-induced tumors. The promoter of the tumor suppressor gene p16 was found to be hypermethylated in all instances (Govindarajan *et al.* 2002), even though the mechanisms by which Ni^{2+} induces DNA hypermethylation are unclear. There is a proposed model which suggests that Ni^{2+} substitutes Mg^{2+} in its interactions with the phosphate backbone of DNA, and Ni^{2+} may be more effective in condensing heterochromatin than Mg^{2+} . Another model proposes increased chromatin condensation and triggering of *de novo* DNA methylation of certain critical tumor suppressor or senescence genes that can become incorporated into heterochromatin as a result of Ni^{2+} presence (Lee *et al.* 1995). Ni^{2+} binding to heterochromatin is not confirmed, but it is hypothesized that it may be due to the high concentration of Mg^{2+} present at the phosphate backbone of DNA in heterochromatin, as compared euchromatin, which may encourage the substitution with Ni^{2+} . Another possibility is that heterochromatin forms the inside lining of the interphase of the nucleus, and with this location it encounters toxins entering the nucleus before they reach euchromatin (Borochoy *et al.* 1984; Conway *et al.* 1987; Costa 1991).

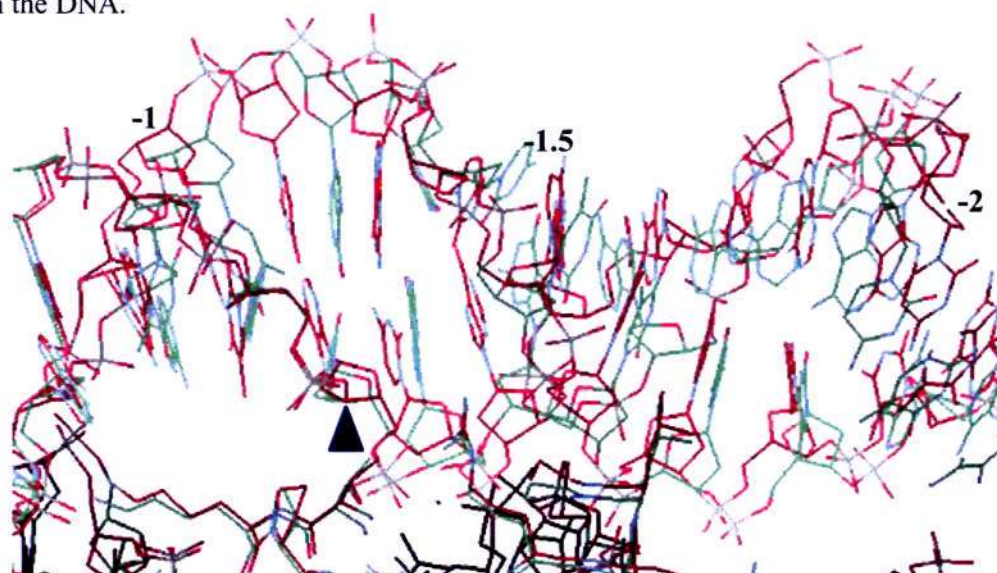
Besides silencing genes by DNA methylation, other Ni^{2+} -induced epigenetic changes include the loss of histone acetylation in H2A, H2B, H3, and H4, increase in H3K9 dimethylation, and increase in ubiquitylation of H2A and H2B at a global level (Lee *et al.* 1995; Broday *et al.* 2000; Karaczyn *et al.* 2005). G12 cells treated with nickel showed a decrease in histone acetylation, H3K4 methylation and H3K9 dimethylation, as well as an increased DNA methylation was observed at the promoter of the *gpt* transgene (Lee *et al.* 1995; Yan *et al.* 2003; Chen *et al.* 2006). In nickel-induced carcinogenesis

Discussion and Outlook

damage to chromatin might directly contribute to this process (Kasprzak *et al.* 2003). This hypothesis is supported by the fact that Ni^{2+} is able to bind to specific motifs of histone H3 and H2A, which could potentially disrupt the structure and function of the nucleosome (Bal *et al.* 1995; Kasprzak *et al.* 2003). Ni^{2+} binding to these histone elements may cause several lesions including oxidative DNA damage through Fenton-like mechanisms and disrupt gene expression resulting in carcinogenicity (Kasprzak *et al.* 2003). Altogether, various data suggest that nickel-induced epigenetic changes contribute more to carcinogenesis than its direct mutagenic effects.

We have observed in our structure the binding of Ni^{2+} to five histidine residues and in particular to one key histidine residue (18His/chain F or H4), which is believed to affect the acetylation of lysine residues. Acetylation of lysine 12 and 16 in yeast is more strongly affected than lysine 5 and 8, hence Costa and co-workers proposed that Ni^{2+} binding to histidine 18 in histone H4 may be responsible for this effect (Lee *et al.* 1995). The suppressive effects of Ni^{2+} on histone H4 acetylation *in vitro* in both yeast and mammalian cells have been reported (Kasprzak *et al.* 2003).

Sequence-specific binding of divalent cations to nucleosomal DNA influences nucleosome positioning and mobility (Davey and Richmond 2002). Binding of Ni^{2+} and Co^{2+} to the NCP in the crystalline state revealed notable 'stretching and shifting' of DNA (Fig. 65) with respect to its position on the HO, as compared to the Mn^{2+} structure, suggesting an influence on the mobility and potentially positioning of the nucleosomes on the DNA.



Discussion and Outlook

Figure 65. DNA stretching in -1.5 SHL of the Ni^{2+} -NCP structure. A region of Ni^{2+} -NCP DNA (green) showing the -1.5 SHL is superposed with the corresponding region of NCP147 (Red; PDB id: IKX5) DNA. This kind of a stretching can potentially influence nucleosome positioning and mobility, as it has been proposed for Mn^{2+} .

Previous studies indicated that nickel ions have higher affinity for amino acids as compared to DNA (Kasprzak *et al.* 2003). However, in our structure of Ni^{2+} -NCP, Ni^{2+} binding was observed predominantly at the DNA. In addition, nickel ion has higher affinity than Mn^{2+} for DNA. The increased nickel ion binding to the DNA in the NCP arises from the softer nature of this metal.

6.4. Metallodrugs in cancer

Medicinal inorganic chemistry is an expanding field of increasing importance as metal-based compounds offer possibilities for the design of therapeutic agents. One such agent is cisplatin and related platinum-based agents which have anti-cancer activity. The therapeutic effect of these drugs appears to be due to preferential coordination of the platinum to the N7 positions of guanine, which results in distortion of the helical structure of DNA, hindering replication and subsequently promoting apoptosis. More recently, much attention has been focused on other transition metals such as ruthenium, osmium and cobalt, as well as their derivatives.

A derivative of cobalt called hexacarbonyl dicobalt 5-alkynyl-2-deoxyuridines shows significant potential as a metallo-drug, which primarily targets DNA (Sergeant *et al.* 2008). The drug was tested for two different breast cancer cell lines MCF-7 and MDA-MB-231 and showed a higher level of cytotoxic effect. In general, most of the DNA in human cells is present in a nucleosomal form. Our NCP structure with cobalt ions could be of potential use to the pharmaceutical chemists in developing better derivatives of anti-cancer metallo-drugs, where they could consider the various parameters of the DNA, especially the base steps of DNA to which cobalt binds with higher affinity and also the conformation of the DNA in nucleosomes.

6.5. Monovalent ions in the DNA of NCP

Monovalent ions are ubiquitous in the nucleus of eukaryotic cells and are known to play a major role in the charge neutralization of the DNA, which is a driving force for DNA compaction. *In vivo* DNA compaction is achieved by histone proteins, which neutralize 57% of the DNA negative charge (Morgan *et al.*, 1987) while the remaining charges are neutralized by other positively charged entities in cell fluid, wherein mono- and divalent cations comprise up to 1% of the cell weight. The most abundant monovalent cations in cells are K^+ and Na^+ , which are not only involved in DNA compaction but also responsible for the regulation of other important biological processes.

Major differences in the interaction of K^+ and Na^+ with the DNA (Strick *et al.*, 2001) are subjects of *in vitro* investigations, as well as those of other monovalent alkali cations such as Li^+ , Rb^+ , and Cs^+ (Bleam *et al.*, 1980; Tereshko *et al.* 1999). However, most of these reports described monocation interactions with naked DNA, and not the nucleosomal form, which contains essential structural details useful in understanding their role in chromatin compaction. Our structural analysis on the interaction of monovalent heavy cations (Rb^+ and Cs^+) with the NCP reveals that these ions have a strong preference for A/T tracts in the NCP, especially when an AT dinucleotide resides in the center of the minor groove. This is in agreement with what has been observed for naked DNA (McFail-Isom *et al.*, 1999). Moreover, as found from these oligonucleotide DNA studies, monovalent ions may generally narrow the minor groove of the DNA by close coordination to the O_2 atom of thymine and N_3 atom of adenine, thus forming an inter-strand bridge. In addition, we observed an intra-strand bridge in the case of Cs ion, where it binds the oxygen atoms of consecutive thymine and cytosine bases in the minor groove.

6.6. Designer DNA and its NCP

Over the last two decades, many different DNA oligonucleotides have been crystallized and studied at atomic resolution. The overall geometry of oligonucleotide DNA has been characterized based on sequence. Initially, Drew and colleagues showed that the conformation of the DNA is dependent upon the nature of the DNA base sequence by studying the crystal structure of B-DNA decamer (Dickerson and Drew 1981). Later on

Discussion and Outlook

using the digestion of the nucleosome DNA in EMSA gel electrophoresis, he showed that the bending of the DNA in nucleosome is strongly dependent upon the sequences, which determine positioning of the DNA in nucleosomes, (Drew and Travers 1985). Earlier, it was believed that the bending of the DNA is influenced by the crystal packing, but Zhurkin and colleagues showed that the intrinsic bending of the DNA is determined by DNA base sequence and the protein's to which it is bound (Olson *et al* 1998). The DNA in chromatin is tightly wrapped around a HO. Therefore, it was critical to investigate the structure of nucleosomal DNA. The first structure of the NCP was solved at 2.8 Å (Luger *et al.* 1997a), which contained a palindromic 146DNA, and few years later a high resolution structure of NCP with an additional base (147DNA) was solved, giving detailed information about the structure of DNA in chromatin (Davey and Richmond 2002).

To date, for the most part, only palindromic DNA was utilized to study the structure of DNA in the NCP. But most of the DNA in our nucleus is non-palindromic. Therefore, we designed non-palindromic DNA sequences containing strong positioning sequences TTAAA, flanking the nucleosome center, which bind to the HO with high affinity. A process including sequence analysis, dinucleotide steps analysis and DNA conformational studies were used to arrive at this particular sequence, which was modified from the usual human α -satellite DNA sequence. As changes in dynamics occur upon DNA binding to HO, DNA loses entropy while forming contacts with the histones. Energy is expended to distort the unbent DNA into 1.67 turns. Nonetheless, Widom and colleagues deduced that many interactions are formed to compensate for the energy cost of bending and loss of entropy. In summary, there are 5 different ways in which a particular DNA sequence can affect the free energy in its interaction with HO: (i) particular DNA sequences can make better bonding with histones through interactions such as salt-bridges, hydrogen bonds, *etc.* (ii) permanent bendedness of DNA (iii) bendability of particular sequences (Cloutier and Widom 2004). (iv) permanent twist of DNA and (v) twistability of DNA (Widom 2002).

DNA conformation gets altered drastically upon binding to the HO. Its twist value changes from 10.5 bp/turn to 10.2 bp/turn. The two important parameters twist and bend of dinucleotide steps are the major players that aid in wrapping. Although this depends on

Discussion and Outlook

sequence and location, other dinucleotide step parameters may also contribute to some extent (slide and tilt in certain minor groove sites) (Richmond and Davey 2003). Particular sequences have a permanent bent, which can make the sequence very difficult to bend in the opposite direction. In general, some sequence types may have a bendability preference, which can be differentiated as two classes; isotropic and anisotropic (Widom 2001; Richmond and Davey 2003). Isotropic bendability is the ability to bend to any direction; thus measurement over time will give a zero bending vector. Anisotropic bendability is similar to permanent bendedness and majoritively indistinguishable from it experimentally. Here the bending is in one direction only, and thus time-averaged measurements will give a non-zero bending vector.

Examples of permanent bendedness, which could also be anisotropic bendedness, are AAAAA that tends to bend into minor groove (negative roll angles) (Fitzgerald and Anderson 1999) and GGGCCC that tends to bend into the major groove (positive roll angles) (Widom 2002). From our experiments, it has been shown that the various designer DNA sequences indeed bind with higher affinity to HO compared to the palindromic DNA147. When we heat the NCP, the electrostatic interaction between DNA and HO decreases and that makes the terminal DNA, which is loosely bound to HO as compared to the DNA at dyad, to slide and reposition itself properly to the center of the HO. In the case of designer DNA, even after heating at 50 °C for 1 hr, only a minute fraction repositioned (Fig. 56). However, these designer DNA NCP samples, when kept at room temperature for 2 days, showed further repositioning, especially in the case of des 2, which we selected for crystallization.

The overall structure of the non-palindromic designer NCP (des 2) DNA was similar to that of palindromic NCP147 DNA. Due to the moderate resolution, only subtle differences were observed. The diffraction quality of the NCP crystals is highly dependant on the length and nature of the DNA sequences. Due to the non-palindromic nature of the DNA in des 2, we obtained a mixed population of two different orientations of DNA in the crystal lattice. As a consequence, there is an overall increase in the B-factors. In addition to this, an improper inter-particle terminal stacking of the DNA was observed. Terminal stacking is highly imperative for proper stabilization of the DNA in NCP. In both DNA termini of des 2 NCP, there is a gap for one additional base pair.

Discussion and Outlook

Even though the length of the DNA of des 2 is 147 bp, the available length is insufficient, as it appears short by one base pair. Thus, it is evident that the length is essential for proper crystal packing, which suggests that the addition of one base pair in the DNA of des 2 would help in getting better diffracting crystals.

Arrangements of the neighboring NCPs in the crystal are important for proper lattice ordering, which is accomplished by two particles engaged in termini stacking and each in turn paired with two other particles on the opposite ends. One side of the inter-particle interface is involved in the strong histone-histone and histone-DNA interactions and the other side is involved in a GC metal-mediated inter-particle DNA-DNA contact. In des 2 NCP, the metal-mediated DNA-DNA inter-particle contact distance was increased, which might have contributed to a weak metal-mediated interaction. Hence, the identity of the DNA sequence, length and also DNA having palindromic nature or potentially non-symmetric orientations in the crystal lattice determines diffraction quality of NCP crystals.

6.7. Outlook

Given the ever-increasing industrial usage of toxic metals, especially in developing nations, the quest for a detailed understanding of carcinogenic metals is on the rise (Galanis *et al* 2009). Furthermore, improved knowledge of metal-mediated cancer pathways would help us to develop more safe metal-based therapeutic agents. It is important to elucidate the contribution from the interactions of the heavy metals with chromatin in the process of carcinogenesis.

REFERENCES

References

References

7. REFERENCES

- Abresica L, Malinina LG, Fernandez T, Huynh-Dinh S, Neidle JA, Subirana NGA (1999) Structure of the oligonucleotide d(CGTATATACG) as a site-specific complex with nickel ions. *Nucl Acids Res* **27**: 1593
- Arita A., and Costa,M (2009) Epigenetics in metal carcinogenesis: nickel, arsenic, chromium and cadmium. *Metallomics*. **1**:222.
- Alexeev DG, Lipanov AA, Skurativskii IY (1987) Poly(dA).poly(dT) is a B-type double helix with a distinctively narrow minor groove. *Nature* **325**: 831
- Allfrey VG, Mirsky AE (1964) Structural modifications of histones and their possible role in the regulation of RNA synthesis. *Science* **144**(3618): 559
- Arents G, Burlingame RW, Wang BC, Love WE, Moudrianakis EN (1991) The nucleosomal core histone octamer at 3.1 Å resolution: A tripartite protein assembly and a left-handed superhelix. *Proceedings of the National Academy of Sciences of the United States of America* **88**(22): 10148-10152
- Auffinger P, Westhof E (2000) Water and ion binding around RNA and DNA (C,G) oligomers. *Journal of Molecular Biology* **300**(5): 1113-1131
- Aust AE, Eveleigh JF (1999) Mechanisms of DNA oxidation. *Proceedings of the Society for Experimental Biology and Medicine* **222**(3): 246-252
- Bal W, Kasprzak KS (2002) Induction of oxidative DNA damage by carcinogenic metals. *Toxicology Letters* **127**(1-3): 55-62
- Bal W, Lukszo J, Jezowska-Bojczuk M, Kasprzak KS (1995) Interactions of nickel(II) with histones. Stability and solution structure of complexes with CH₃CO-CyS-Ala-Ile-His-NH₂, a putative metal binding sequence of histone H3. *Chemical Research in Toxicology* **8**(5): 683-692
- Bao Y, White CL, Luger K (2006) Nucleosome Core Particles Containing a Poly (dA·dT) Sequence Element Exhibit a Locally Distorted DNA Structure. *Journal of Molecular Biology* **361**(4): 617-624
- Becker PB (2002) Nucleosome sliding: Facts and fiction. *EMBO Journal* **21**(18): 4749-4753
- Bentley GA, Lewit-Bentley A, Finch JT (1984) Crystal structure of the nucleosome core particle at 16 Å resolution. *Journal of Molecular Biology* **176**(1): 55-75
- Bin W, Davey CA (2010) Using Soft X-Rays for a Detailed Picture of Divalent Metal Binding in the Nucleosome. *Journal of Molecular Biology* **398**(5): 633-640

References

- Blank TA, Becker PB (1995) Electrostatic mechanism of nucleosome spacing. *Journal of Molecular Biology* **252**(3): 305-313
- Bleam ML, Anderson CF, and Record MT. (1980) Relative binding affinities of monovalent cations for double-stranded DNA. *Proc Natl Acad Sci USA*(77): 3085-3089
- Bloomfield VA, Crothers DM, Tinoco I Jr (2000) *Nucleic Acids, Structures, Properties, and Functions*; University Science Books: Sausalito, CA. pp-508 and 512.
- Borochoy N, Ausio J, Eisenberg H (1984) Interaction and conformational changes of chromatin with divalent ions. *Nucleic Acids Research* **12**(7): 3089-3096
- Broday L, Peng W, Kuo MH, Salnikow K, Zoroddu M, Costa M (2000) Nickel compounds are novel inhibitors of histone H4 acetylation. *Cancer Research* **60**(2): 238-241
- Chantalat L, Nicholson JM, Lambert SJ, Reid AJ, Donovan MJ, Reynolds CD, Wood CM, Baldwin JP (2003) Structure of the histone-core octamer in KCl/phosphate crystals at 2.15 Å resolution. *Acta Crystallographica - Section D Biological Crystallography* **59**(8): 1395-1407
- Chen H, Ke Q, Kluz T, Yan Y, Costa M (2006) Nickel ions increase histone H3 lysine 9 dimethylation and induce transgene silencing. *Molecular and Cellular Biology* **26**(10): 3728-3737
- Clark DJ, Kimura T (1990) Electrostatic mechanism of chromatin folding. *Journal of Molecular Biology* **211**(4): 883-896
- Cloutier TE, Widom J (2004) Spontaneous sharp bending of double-stranded DNA. *Molecular Cell* **14**(3): 355-362
- Conway K, Wang XW, Xu LS, Costa M (1987) Effect of magnesium on nickel-induced genotoxicity and cell transformation. *Carcinogenesis* **8**(8): 1115-1121
- Cooke MS, Evans MD, Dizdaroglu M, Lunec J (2003) Oxidative DNA damage: mechanisms, mutation, and disease. *FASEB Journal* **17** (10): 1195-1214
- Cosgrove MS, Boeke JD, Wolberger C (2004) Regulated nucleosome mobility and the histone code. *Nature Structural and Molecular Biology* **11**(11): 1037-1043
- Cosgrove MS, Wolberger C (2005) How does the histone code work? *Biochemistry and Cell Biology* **83**(4): 468-476
- Costa M (1991) Molecular mechanisms of nickel carcinogenesis. *Annual Review of Pharmacology and Toxicology* **31**: 321-337

References

- Davey CA, Richmond TJ (2002) DNA-dependent divalent cation binding in the nucleosome core particle. *Proceedings of the National Academy of Sciences of the United States of America* **99**(17): 11169-11174
- Davey CA, Sargent DF, Luger K, Maeder AW, Richmond TJ (2002) Solvent mediated interactions in the structure of the nucleosome core particle at 1.9 Å resolution. *Journal of Molecular Biology* **319**(5): 1097-1113
- Denisov VP, Halle B (2000) Sequence-specific binding of counterions to B-DNA. *Proceedings of the National Academy of Sciences of the United States of America* **97**(2): 629-633
- Dickerson RE, Bansal, M., Calladine, C.R., Diekmann, S., Hunter, W.N., and Kennard, O. (1989) Definitions and nomenclature of nucleic acid structure parameters. *EMBO Journal* **8**(1): 1-4
- Drew HR, Travers AA (1981) Structure of a B-DNA Dodecamer II. Influence of Base Sequence on Helix Structure. *J. Mol. Biol.* **149**: 761-786
- Drew HR, Travers AA (1985) DNA Bending and its Relation to Nucleosome Positioning. *J. Mol. Biol.* **186**: 773-790
- Dyer PN, Edayathumangalam RS, White CL, Bao Y, Chakravarthy S, Muthurajan UM, Luger K. (2004) Reconstitution of Nucleosome Core Particles from Recombinant Histones and DNA. *Methods in Enzymology*, Vol. 375, pp. 23-44.
- Elgin S C R., Workman J L. (2000). Chromatin Structure and Gene Expression, pp. 328. Oxford, UK: *Oxford University Press*
- Emsley P, Cowtan K (2004) Coot: Model-building tools for molecular graphics. *Acta Crystallographica Section D: Biological Crystallography* **60**(12 I): 2126-2132
- Felsenfeld G, Groudine M (2003) Controlling the double helix. *Nature* **421**(6921): 448-453
- Ferner DJ (2001) Toxicity, heavy metals. *Med J* **2**: 1
- Finch JT, Brown RS, Rhodes D, Richmond T, Rushton B, Lutter LC, Klug A (1981) X-ray diffraction study of a new crystal form of the nucleosome core showing higher resolution. *Journal of Molecular Biology* **145**(4): 757-769
- Fitzgerald DJ, Anderson JN (1999) DNA distortion as a factor in nucleosome positioning. *Journal of Molecular Biology* **293**(3): 477-491
- Fletcher TM, Hansen JC (1995) Core histone tail domains mediate oligonucleosome

References

- folding and nucleosomal DNA organization through distinct molecular mechanisms. *Journal of Biological Chemistry* **270**(43): 25359-25362
- Froystein NA, Davis JT, Reid BR, Sletten E (1993) Sequence-selective metal ion binding to DNA oligonucleotides. *Acta chemica Scandinavica (Copenhagen, Denmark : 1989)* **47**(7): 649-657
- Galanis A, Karapetsas A, Sandaltzopoulos R (2009) Metal-induced carcinogenesis, oxidative stress and hypoxia signalling. *Mutation Research - Genetic Toxicology and Environmental Mutagenesis* **674**(1-2): 31-35
- Govindarajan B, Klafter R, Steven Miller M, Mansur C, Mizesko M, Bai X, LaMontagne Jr K, Arbiser JL (2002) Reactive oxygen-induced carcinogenesis causes hypermethylation of p16ink4a and activation of MAP kinase. *Molecular Medicine* **8**(1): 1-8
- Halliwell B, Aruoma OI (1991) DNA damage by oxygen-derived species. Its mechanism and measurement in mammalian systems. *FEBS Letters* **281**(1-2): 9-19
- Hoekstra, MF. and Jac A. Nickoloff, DNA Damage and Repair Vol II, *DNA Repair in Higher eucaryotes* pp No – 201-203
- Hsu YY, Wang YH (2002) Human fragile site FRA16B DNA excludes nucleosomes in the presence of distamycin. *Journal of Biological Chemistry* **277**(19): 17315-17319
- Hunter CA (1993) Sequence-dependent DNA structure. The role of base stacking interactions. *Journal of Molecular Biology* **230**(3): 1025-1054
- Inoue M, Sato EF, Nishikawa M, Park AM, Kira Y, Imada I, Utsumi K (2003) Mitochondrial generation of reactive oxygen species and its role in aerobic life. *Current Medicinal Chemistry* **10**(23): 2495-2505
- Izatt RM, Christensen JJ, Rytting JH. (1971) Sites and thermodynamic quantities associated with proton and metal ion interaction with ribonucleic acid, deoxyribonucleic acid, and their constituent bases, nucleosides and nucleotides. *Chem.Rev* **71**, 439-481.
- Kabsch W (1993) Automatic processing of rotation diffraction data from crystals of initially unknown symmetry and cell constants. *Journal of Applied Crystallography* **26**(6): 795-800
- Karaczyn AA, Golebiowski F, Kasprzak KS (2005) Truncation, deamidation, and oxidation of histone H2B in cells cultured with nickel(II). *Chemical Research in Toxicology* **18**(12): 1934-1942
- Karoui H, Hogg N, Frejaville C, Tordo P, Kalyanaraman B (1996) Characterization of

References

- sulfur-centered radical intermediates formed during the oxidation of thiols and sulfite by peroxynitrite: ESR-spin trapping and oxygen uptake studies. *Journal of Biological Chemistry* **271**(11): 6000-6009
- Kasprzak KS, Bal W, Karaczyn AA (2003) The role of chromatin damage in nickel-induced carcinogenesis. A review of recent developments. *Journal of Environmental Monitoring* **5**(2): 183-187
- Kelbauskas L, Chan N, Bash R, Yodh J, Woodbury N, Lohr D (2007) Sequence-dependent nucleosome structure and stability variations detected by Forster resonance energy transfer. *Biochemistry* **46**(8): 2239-2248
- Kobayashi S, Ueda K, Komano T (1990) The effects of metal ions on the DNA damage induced by hydrogen peroxide. *Agricultural and biological chemistry* **54**(1): 69-76
- Kornberg R (1981) The location of nucleosomes in chromatin: Specific or statistical? *Nature* **292**(5824): 579-580
- Kumar SV, Wigge PA. (2010) H2A.Z-containing nucleosomes mediate the thermosensory response in Arabidopsis. *Cell* **140**(1):136-47
- Lavelle C, Benecke A (2006) Comment: Chromatin physics: Replacing multiple, representation-centered descriptions at discrete scales by a continuous, function-dependent self-scaled model. *European Physical Journal E* **19**(3): 379-384
- Lavery R, Sklenar H (1988) The definition of generalized helicoidal parameters and of axis curvature for irregular nucleic acids. *Journal of biomolecular structure & dynamics* **6**(1): 63-91
- Lee YW, Klein CB, Kargacin B, Salnikow K, Kitahara J, Dowjat K, Zhitkovich A, Christie NT, Costa M (1995) Carcinogenic nickel silences gene expression by chromatin condensation and DNA methylation: A new model for epigenetic carcinogens. *Molecular and Cellular Biology* **15**(5): 2547-2557
- Leslie A.G.W. (1992). *Joint CCP4 + ESF-EAMCB Newsletter on Protein crystallography*. No. **26**.
- Leonard SS, Bower JJ, Shi X (2004) Metal-induced toxicity, carcinogenesis, mechanisms and cellular responses. *Molecular and Cellular Biochemistry* **255**(1-2): 3-10
- Li G, Widom J (2004) Nucleosomes facilitate their own invasion. *Nature Structural and Molecular Biology* **11**(8): 763-769
- Liang Q, Dedon PC (2001) Cu(II)/H₂O₂-induced DNA damage is enhanced by packaging of DNA as a nucleosome. *Chemical Research in Toxicology* **14**(4):

References

- 416-422
- Lu XJ, Olson WK (2003) 3DNA: A software package for the analysis, rebuilding and visualization of three-dimensional nucleic acid structures. *Nucleic Acids Research* **31**(17): 5108-5121
- Luger K (2003) Structure and dynamic behavior of nucleosomes. *Current Opinion in Genetics and Development* **13**(2): 127-135
- Luger K (2006) Dynamic nucleosomes. *Chromosome Research* **14**(1): 5-16
- Luger K, Mader AW, Richmond RK, Sargent DF, Richmond TJ (1997a) Crystal structure of the nucleosome core particle at 2.8 Å resolution. *Nature* **389**(6648): 251-260
- Luger K, Rechsteiner TJ, Flaus AJ, Waye MMY, Richmond TJ (1997b) Characterization of nucleosome core particles containing histone proteins made in bacteria. *Journal of Molecular Biology* **272**(3): 301-311
- Luger K, Rechsteiner TJ, Richmond TJ. (1999) Preparation of nucleosome core particle from recombinant histones. *Methods in Enzymology*, Vol. 304, pp. 3-19.
- Luger K, Richmond TJ (1998) DNA binding within the nucleosome core. *Current Opinion in Structural Biology* **8**(1): 33-40
- Marnett LJ (2000) Oxyradicals and DNA damage. *Carcinogenesis* **21**(3): 361-370
- McFail-Isom L, Sines CC, Williams LD (1999) DNA structure: cations in charge? *Current Opinion in Structural Biology* **9**: 298-304
- Millonig H, Pous J, Gouyette C, Subirana JA, Campos JL (2009) The interaction of manganese ions with DNA. *Journal of Inorganic Biochemistry* **103**(6): 876-880
- Mirzabekov AD, Rich A (1979) Asymmetric lateral distribution of unshielded phosphate groups in nucleosomal DNA and its role in DNA bending. *Proceedings of the National Academy of Sciences of the United States of America* **76**(3): 1118-1121
- Moldrheim E, Andersen B, Froystein NA, Sletten E (1998) Interaction of manganese(II), cobalt(II) and nickel(II) with DNA oligomers studied by ¹H NMR spectroscopy. *Inorganica Chimica Acta* **273**(1-2): 41-46
- Morgan JE, Blankenship JW, Matthews HR (1987) Polyamines and acetylpolyamines increase the stability and alter the conformation of nucleosome core particles. *Biochemistry* **26**(12): 3643-3649
- Olson WK, Gorin AA, Lu XJ, Hock Lm, Zhurkin VB (1998). DNA sequence-dependent deformability deduced from protein-DNA crystal complexes. *Proc. Natl. Acad. Sci. USA* **95**: 11163-11168.

References

- Ong MS, Richmond TJ, Davey CA (2007) DNA Stretching and Extreme Kinking in the Nucleosome Core. *Journal of Molecular Biology* **368**(4): 1067-1074
- Packer MJ, Dauncey MP, Hunter CA (2000) Sequence-dependent DNA structure: Dinucleotide conformational maps. *Journal of Molecular Biology* **295**(1): 71-83
- Pearson RG (1990) Hard and soft acids and bases - The evolution of a chemical concept. *Coordination Chemistry Reviews* **100**: 403-425
- Pennings S, Meersseman G, Bradbury EM (1991) Mobility of positioned nucleosomes on 5 S rDNA. *Journal of Molecular Biology* **220**(1): 101-110
- Pflugrath JW (1999) The finer things in X-ray diffraction data collection. *Acta Crystallographica Section D: Biological Crystallography* **55**(10): 1718-1725
- Prunell A, Kornberg RD (1982) Variable center to center distance of nucleosomes in chromatin. *Journal of Molecular Biology* **154**(3): 515-523
- Pullman A, Pullman B (1981) Molecular electrostatic potential of the nucleic acids. *Quarterly Reviews of Biophysics* **14**(3): 289-380
- Ramakrishnan V. (1997) Histone structure and the organization of the nucleosome. *Annual Review of Biophysics and Biomolecular Structure* **26**: 83-112
- Richmond TJ, Davey CA (2003) The structure of DNA in the nucleosome core. *Nature* **423**(6936): 145-150
- Richmond TJ, Finch JT, Rushton B, Rhodes D, Klug A (1984) Structure of the nucleosome core particle at 7 Å resolution. *Nature* **311**(5986): 532-537
- Richmond TJ, Searles MA, Simpson RT (1988) Crystals of a nucleosome core particle containing defined sequence DNA. *Journal of Molecular Biology* **199**(1): 161-170
- Robert E (1999) Intrauterine effects of electromagnetic fields - (Low frequency, mid-frequency RF, and microwave): Review of epidemiologic studies. *Teratology* **59**(4): 292-298
- Rouzina L, Bloomfield VA (1998) DNA bending by small, mobile multivalent cations. *Biophysical Journal* **74**(6): 3152-3164
- Salnikow K, Zhitkovich A (2008) Genetic and Epigenetic Mechanisms in Metal Carcinogenesis and Cocarcinogenesis: Nickel, Arsenic, and Chromium. *Chem. Res. Toxicol.* **(21)**: 28-44.

References

- Sambrook J., Russell D. Molecular Cloning (2001): *A Laboratory manual*. Cold Spring Harbour Laboratory Press, Cold Spring Harbor, NY.
- Santisteban MS, Arents G, Moudrianakis EN, Smith MM (1997) Histone octamer function in vivo: Mutations in the dimer-tetramer interfaces disrupt both gene activation and repression. *EMBO Journal* **16**(9): 2493-2506
- Satchwell SC, Drew HR, Travers AA (1986) Sequence periodicities in chicken nucleosome core DNA. *Journal of Molecular Biology* **191**(4): 659-675
- Schwarz PM, Felthausen A, Fletcher TM, Hansen JC (1996) Reversible oligonucleosome self-association: Dependence on divalent cations and core histone tail domains. *Biochemistry* **35**(13): 4009-4015
- Segal, E., Y. Fondufe-Mittendorf, L. Chen, A. C. Thastrom, Y. Field, I. K. Moore, J. P. Z. Wang and J. Widom (2006). A genomic code for nucleosome positioning. *Nature* **442**: 772-778.
- Sen P, Costa M (1985) Induction of chromosomal damage in Chinese hamster ovary cells by soluble and particulate nickel compounds: Preferential fragmentation of the heterochromatic long arm of the X-chromosome by carcinogenic crystalline NiS particles. *Cancer Research* **45**(5): 2320-2325
- Sergeant CD, Ott I, Sniady A, Meneni S, Gust R, Rheingold AL, Dembinski R (2008) Metallo-nucleosides: Synthesis and biological evaluation of hexacarbonyl dicobalt 5-alkynyl-2'-deoxyuridines. *Organic and Biomolecular Chemistry* **6**(1): 73-80
- Shrader TE, Crothers DM (1989) Artificial nucleosome positioning sequences. *Proceedings of the National Academy of Sciences of the United States of America* **86**(19): 7418-7422
- Smith SR, Jaffe DM, Skinner MA (1997) Case report of metallic mercury injury. *Pediatric Emergency Care* **13**(2): 114-116
- Soler-Lolpez M, Malinina L, Tereshko V, Zarytova V, Subirana JA (2002) Interaction of zinc ions with d(CGCAATTGCG) in a 2.9 Å resolution X-ray structure. *Journal of Biological Inorganic Chemistry* **7**(4-5): 533-538
- Stohs SJ, Bagchi D (1995) Oxidative mechanisms in the toxicity of metal ions. *Free Radical Biology and Medicine* **18**(2): 321-336
- Strahl BD, Allis CD (2000) The language of covalent histone modifications. *Nature* **403**(6765): 41-45
- Strick R, Strissel PL, Gavrilov K, Levi-Setti R, Daban JR (2001) Cation-chromatin

References

- binding as shown by ion microscopy is essential for the structural integrity of chromosomes. *Journal of Cell Biology* **155**(6): 899-910
- Tereshko V, Minasov G, Egli M (1999) A 'hydrat-ion' spine in a B-DNA minor groove. *Journal of the American Chemical Society* **121**(15): 3590-3595
- Thastrom A, Lowary PT, Widom J (2004) Measurement of histone–DNA interaction free energy in nucleosomes. *Methods* **33**: 33–44
- Thoma F (1992) Nucleosome positioning. *Biochimica et Biophysica Acta - Gene Structure and Expression* **1130**(1): 1-19
- Thoma F, Koller T, Klug A (1979) Involvement of histone H1 in the organization of the nucleosome and of the salt-dependent superstructures of chromatin. *Journal of Cell Biology* **83**(2): 403-427
- Thomas JO, Butler PJG (1977) Characterization of the octamer of histones free in solution. *Journal of Molecular Biology* **116**(4): 769-781
- Travers AA (2004) The structural basis of DNA flexibility. *Philosophical Transactions of the Royal Society A: Mathematical, Physical and Engineering Sciences* **362**(1820): 1423-1438
- Travers AA, Klug A (1987) The bending of DNA in nucleosomes and its wider implications. *Philosophical transactions of the Royal Society of London Series B: Biological sciences* **317**(1187): 537-561
- Valko M, Morris H, Cronin MTD (2005) Metals, toxicity and oxidative stress. *Current Medicinal Chemistry* **12**(10): 1161-1208
- Valko M, Rhodes CJ, Moncol J, Izakovic M, Mazur M (2006) Free radicals, metals and antioxidants in oxidative stress-induced cancer. *Chemico-Biological Interactions* **160**(1): 1-40
- Valls N, Wright G, Steiner RA, Murshudov GN, Subirana JA (2004) DNA variability in five crystal structures of d(CGCAATTGCG). *Acta Crystallographica Section D: Biological Crystallography* **60**(4): 680-685
- Widom J (1986) Physicochemical studies of the folding of the 100 Å nucleosome filament into the 300 Å filament. Cation dependence. *Journal of Molecular Biology* **190**(3): 411-424
- Widom J. (1998) Structure, dynamics, and function of chromatin in vitro. *Annual Review of Biophysics and Biomolecular Structure*, Vol. 27, pp. 285-327.
- Widom J (2001) Role of DNA sequence in nucleosome stability and dynamics. *Quarterly*

References

Reviews of Biophysics **34**(3): 269-324

- Wood CM, Nicholson JM, Lambert SJ, Chantalat L, Reynolds CD, Baldwin JP (2005) High-resolution structure of the native histone octamer. *Acta Crystallographica Section F: Structural Biology and Crystallization Communications* **61**(6): 541-545
- Yan Y, Kluz T, Zhang P, Chen HB, Costa M (2003) Analysis of specific lysine histone H3 and H4 acetylation and methylation status in clones of cells with a gene silenced by nickel exposure. *Toxicology and Applied Pharmacology* **190**(3): 272-277
- Ye J, Ai X, Eugeni EE, Zhang L, Carpenter LR, Jelinek MA, Freitas MA, Parthun MR (2005) Histone H4 lysine 91 acetylation: A core domain modification associated with chromatin assembly. *Molecular Cell* **18**(1): 123-130
- Zheng C, Hayes JJ (2003) Structures and interactions of the core histone tail domains. *Biopolymers* **68**(4): 539-546